Computational Investigation of Structure, Dynamics and Proton Transport in Polymer Electrolyte Membrane Fuel Cells

A

thesis submitted

in partial fulfillment of the requirements for the degree of

DOCTOR OF PHILOSOPHY

by

Rakesh Pant

Roll No.:20133265

Indian Institute of Science Education and Research, Pune

2019

Certificate

Certified that the work incorporated in the thesis entitled *"Computational Investigation of Structure, Dynamics and Proton Transport in Polymer Electrolyte Membrane Fuel Cells"* submitted by **Rakesh Pant** was carried out by the candidate, under my supervision. The work presented here or any part of it has not been included in any other thesis submitted previously for the award of any degree or diploma from any other University or institution.

Date:

Dr. Arun Venkatnathan

(Supervisor)

Declaration

I declare that this written submission represents my ideas in my own words and where others ideas have been included, I have adequately cited and referenced the original sources. I also declare that I have adhered to all principles of academic honesty and integrity and have not misrepresented or fabricated or falsified any idea/data/fact/source in my submission. I understand that violation of the above will be cause for disciplinary action by the Institute and can also evoke penal action from the sources which have thus not been properly cited or from whom proper permission has not been taken when needed.

Date:

Rakesh Pant

(Roll No.:20133265)

I dedicate this thesis to my family...

Acknowledgement

I express my sincere gratitude to my Ph.D. supervisor Dr. Arun Venkatnathan for his support, patience, motivation, and help during my Ph.D. program. His critical comments, suggestions, and approach have helped me improve my understanding of the subject. It would have been impossible to complete this journey without his support.

I am grateful to Dr. Milan Kumar for his collaborative work in one of my projects. I am thankful to my collaborators Dr. Alexey, V. Lyulin, Soumyadipta Sengupta, Dr. Kostas Karatasos, and Dr. Georgios Kritikos for their help in collaborative work. I thank Group Theory of Polymers and Soft Matter at the Technische Universiteit Eindhoven for the hospitality during my stay there. I acknowledge my research advisory committee members: Dr. Arun Venkatnathan, Dr. Anirban Hazra, and Dr. Kumar Vanka for their valuable comments and suggestions which has significantly improved my research understanding.

I thank my labmates Minal, Praveen, Prabhat, and Anna for their inputs in my research work and maintaining a friendly environment in the lab. Also, all my friends who supported me in this journey. I express my sincere thanks to Subrahmanyam Sappati and Reman Kumar, for their suggestions during various stages of my Ph.D. I want to thank Yogeshwar More for his help in designing figures for my thesis. I thank Suresh, Sachin, and Nisha from IT department for providing technical support. I thank Indian Institute of Science Education and Research, Pune for graduate fellowship for my research work. I would like to thank American Chemical Society, Royal Society of Chemistry, Elsevier, IOP Publishing and Wiley for permission to include figures from copyrighted articles.

Last, but not least, I would like to thank my parents and family members for their love and support in all endeavors of life.

IISER Pune **Rakesh Pant**

List of Publications

- **Pant, R.**; Sengupta, S.; Lyulin, A. V. and Venkatnathan, A.; *Computational Investigation of a Protic Ionic Liquid doped Poly-benzimidazole: Fuel Cell Electrolyte*, (Under Review).

- **Pant, R.**; Sengupta, S.; Lyulin, A. V. and Venkatnathan, A.; *Charge Delocalization Effects on Nafion Structure and Water/Proton Dynamics in Hydrated Environments*, Fluid Phase Equilibria. *2020*, 504, 112340

- Kritikos, G.; **Pant, R.**; Sengupta, S.; Karatasos, K; Venkatnathan, A. and Lyulin, A. V.; *Nanostructure and Dynamics of Humidified Nafion-Graphene Oxide Composites via Molecular Dynamics Simulations*, J. Phys. Chem. C, *2018*, 122, 22864-22875

- Sengupta, S.; **Pant, R.**; Komarov, R.; Venkatnathan, A. and Lyulin, A. V.; *Atomistic Simulation Study of the Hydrated Structure and Dynamics of a Novel Multi Acid Side Chain Polyelectrolyte Membrane*, Int J. Hydrogen Energy, *2017*, 42, 27254-27268

- **Pant, R.**[†]; Kumar, M.[†] and Venkatnathan, A.; *Quantum Mechanical Investigation of Proton Transport in Imidazolium Methanesulfonic Acid Ionic Liquid*, J. Phys. Chem. C, *2017*, 121, 7069-7080

[†]Equal Contribution

Contents

List of Figures

List of Tables

Abbreviations

PEM	:	Polymer Electrolyte Membrane
MD	:	Molecular Dynamics
OPLS-AA	:	Optimized Potentials for Liquid Simulations-All Atom
PME	:	Particle-Mesh Ewald
NPT	:	Isobaric Isothermal
NVT	:	Isochoric Isothermal
RDF	:	Radial Distribution Function
MSD	:	Mean Square Displacement
DFT	:	Density Functional Theory
MS-EVB	:	Multistate Empirical Valence Bond
IL	:	Ionic Liquid
PIL	:	Protic Ionic Liquid
TS	:	Transition State
MSA	:	Methanesulfonic Acid
IMMSA	:	Imidazolium-methanesulfonate
PES	:	Potential Energy Surface
ZPE	:	Zero Point Energy
AIMD	:	*Ab initio* Molecular Dynamics

Abstract

Polymer electrolyte membrane fuel cells are environmentally friendly energy conversion devices where electrical energy is derived from chemical energy. The key role of the membrane is to prevent the mixing of the reactant gases, to conduct protons from anode to cathode and to provide insulation to the transfer of electrons. Experimental techniques and computer simulations have been employed extensively to study structure, surface morphology, membrane deformation, dynamics, hydrophilicity, etc. of various polymer electrolyte membranes. In this thesis, molecular dynamics (MD) simulations (using all-atom force field) is employed to examine structure/dynamics of molecular transport in hydrated perfluorosulfonic acid and N,N-diethyl-N-methylammonium triflate([dema][TfO]) ionic liquid (IL) doped poly-benzimidazole (PBI) fuel cell environments.

In the first part, MD simulations are employed to examine the effect of atomic charge delocalization on the pendant side chain of hydrated Nafion on the structural and dynamical properties. The sulfur-sulfur radial distribution functions suggest that the sulfonate groups of the pendant side chain have closer geometric proximity with an increase in charge delocalization. A complex interplay between sulfur-sulfur, sulfur-water/hydronium interactions, and water cluster distribution plays a key role in the magnitude of the diffusion coefficient of water molecules and hydronium ions. In the second study, the simulations predict ionic conductivity increases with wt% of [dema][TfO] IL (in IL-doped PBI) and temperature and is found to be in qualitative agreement with experimental measurements. Also, the simulations predict that anions of IL preferably interact with the interaction site on the PBI. In the final investigation, quantum chemistry calculations are employed to examine proton transport pathways in base rich imidazolium methanesulfonate (IMMSA) IL. When IMMSA interacts with two imidazole molecules, one of the pathways shows barrierless rotation of imidazole molecules. This could be the reason for high proton conductivity in base rich imidazolium ILs.

Chapter 1

Introduction

The excessive use of fossil fuels has led to global warming which necessitates the development of alternatives for energy technology. Polymer electrolyte membrane (PEM) fuel cells are environmentally friendly energy conversion devices where electrical energy is derived from chemical energy stored in simple fuels, such as hydrogen. PEMFCs have been used for various stationary, portable and transportation applications.[1,2] Hydrogen gas is introduced at the anode, where it dissociates into protons and electrons with the help of a platinum catalyst. The electrons flow through the external circuit, and the protons are

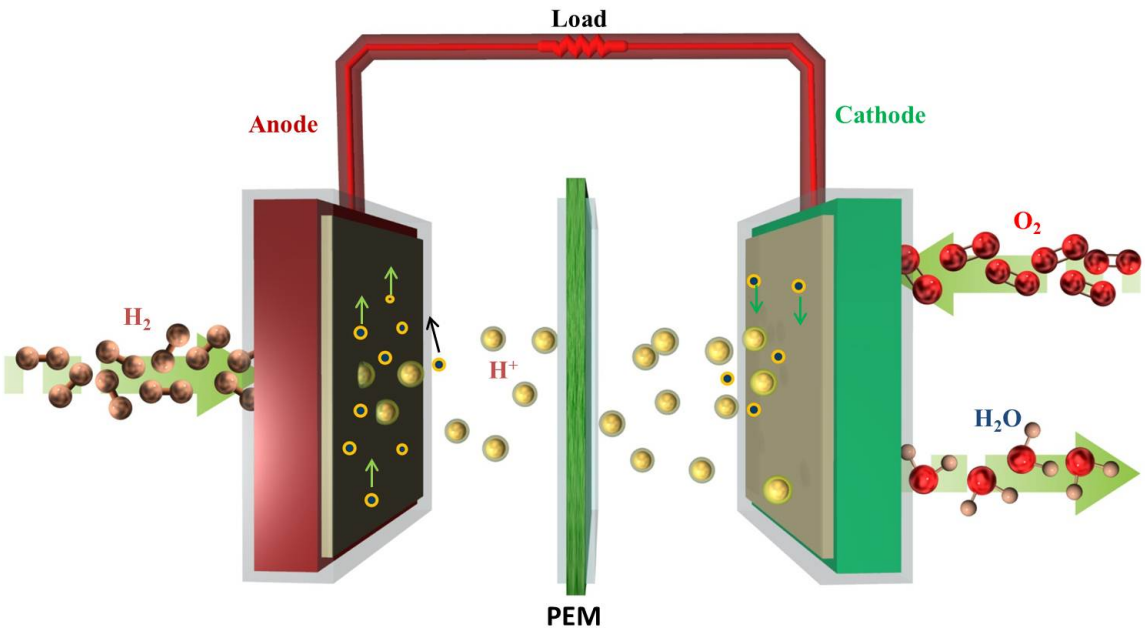

Figure 1.1: Schematic of PEMFC.

transported to the cathode with the help of electrolytic membrane. Oxygen gas is introduced at the cathode, which interacts with protons and electrons to produce liquid water.

The chemical reactions are as follows:

Anode:

$$H_2 \rightarrow 2H^+ + 2e^- \tag{1.1}$$

Cathode:

$$\frac{1}{2}O_2 + 2H^+ + 2e^- \rightarrow H_2O \tag{1.2}$$

Overall Reaction:

$$H_2 + \frac{1}{2}O_2 \rightarrow H_2O \tag{1.3}$$

The polymer membrane is a vital component of the PEMFC (see Figure 1.1). The membrane prevents mixing of reactant gases and assists in proton conduction across the electrode. The polymer membrane should have high mechanical, thermal stability, chemical resistivity, and provide insulation to the transfer of electrons and have high proton conductivity in fuel cell environments.[3,4] Several PEMs, such as Nafion (Perfluorosulfonic acid

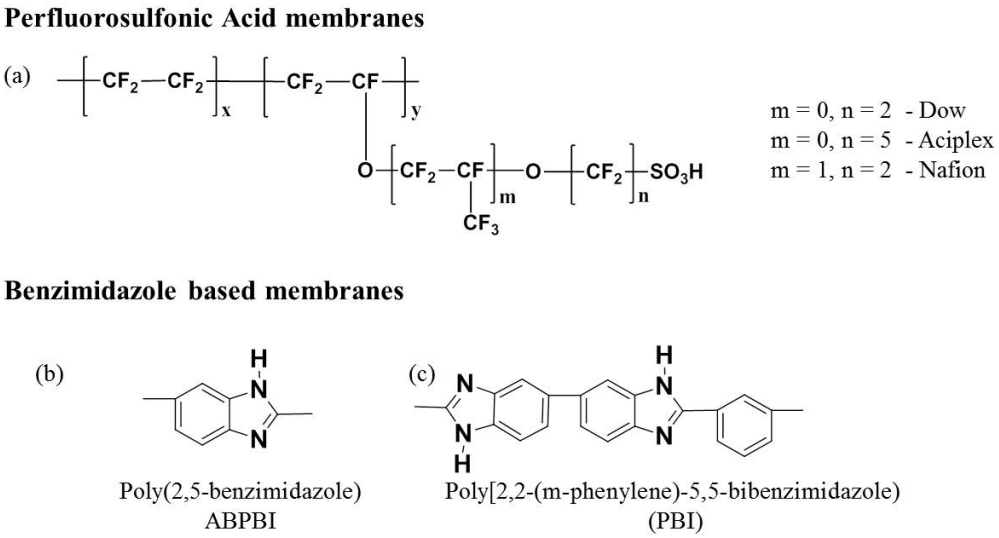

Figure 1.2: Chemical structure of (a) PFSA (b) ABPBI and (c) PBI

(PFSA)) (see Figure 1.2),[3–5] and aromatic membranes such as poly(2,5-benzimidazole)

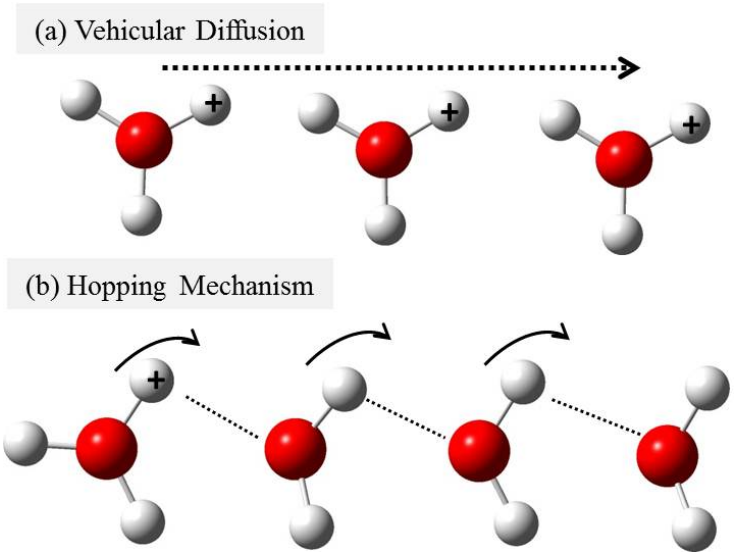

Figure 1.3: Proton transport mechanisms (a) Vehicular diffusion of hydronium ions (b) Hopping mechanism of proton transport.

(ABPBI), poly[2,2-(m-phenylene)-5,5-bibenzimidazole) (PBI), etc. have been explored for fuel cell applications. The membranes require charge carriers to conduct protons (via vehicular diffusion[6] or Grotthuss (hopping/structural) mechanism[7] (see Figure 1.3)) to achieve high conductivity desired for commercial applications of PEMFCs. A wide range of charge carriers such as water,[4] phosphoric acid,[8] imidazole,[5] ionic liquids (ILs),[9] etc. have been explored. A description of literature on humidified and non-humidified membranes is presented in the subsequent sections.

1.1 Humidified membranes

PFSA membranes have a hydrophobic backbone, and the pendant side chain is hydrophilic. Such structure results in a enhanced phase-separated morphology in hydrated conditions. The hydrophobic backbone provides mechanical strength and hydrophilic phase assists in proton transport. PFSA membranes (e.g. Nafion) have been extensively studied[4,10–12] using a wide range of experimental techniques and theoretical methods. Experimental meth-

ods such as X-ray,[13] atomic force microscopy (AFM),[14–17] electrochemical mass transport measurements,[18] and contact angle measurements,[19–21] etc. have been employed to examine water uptake, scattering intensity, surface morphology, hydrophilicity, membrane deformation, and micelle orientation. A schematic (see Figure 1.4) of Nafion polymer backbone, hydrophilic groups, and the water phase illustrates phase separation which occurs due to hydrated conditions (backbone is not cylindrical rather just a schematic to show phase separated morphology). The AFM studies confirm stronger phase-separation in hy-

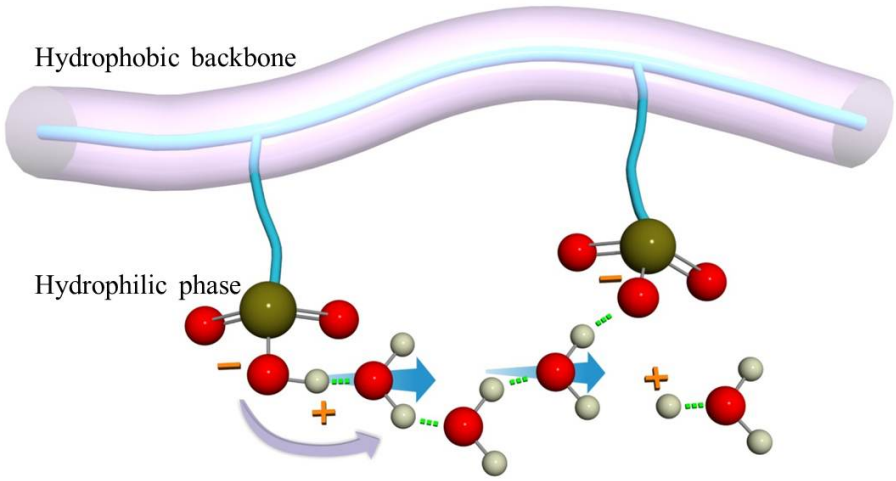

Figure 1.4: Schematic of hydrated PFSA Membrane.

drated conditions as compared to hydrophobic surface depleted of hydrophilic groups in dry conditions. McLean et al.[15] employed AFM and phase imaging methods and showed a cluster-like structure of the hydrophilic domains. The authors concluded that swelling and redistribution of hydrophilic clusters is a dynamic process. The current sensing AFM results from the work of Kostecki and coworkers,[22] on Nafion at low relative humidity (RH) (see Figure 1.5) shows predominantly non-conductive domains responsible for the limited connectivity in the hydrophilic network. The authors observed a more pronounced current pattern of more conducting and larger active regions with the increase in RH. The clustering of hydrophilic domains (conducting areas) increases at high RH. The red color

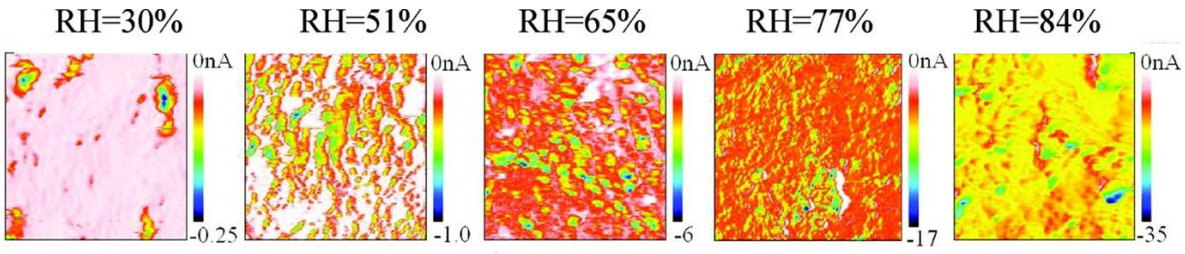

Figure 1.5: Synchronized AFM current-sensing image of Nafion. Reprinted with permission from the work of Kostecki and coworkers.[22] Copyright American Chemical Society.

indicates more conductive regions. The current shown in the color scale bar shows that flow of current increases with increase in hydration (the difference in the magnitude of values is more at higher hydration levels). A few non-conducting patches appear on the membrane surface due to hydrophobic backbone. Zawodzinski et al.[23] using contact angle measurements observed that the surface of PFSA membrane is relatively hydrophobic at low RH. Perrin et al.[24] employed Small angle neutron scattering (SANS) study on hydrated Nafion, and observed (see Figure 1.6) a shift and increment in the ionomer peak in the SANS structure factors with hydration which demonstrates nanoscale swelling of the hydrophilic domains. In a review article, Kusoglu and Weber[12] compared (see Figure 1.7) the diffusion coefficient of water molecules in several PFSA (Dow, Aquivion, Flemion, 3M, and Gore-Select) membranes.

In addition to experimental studies, computational methods have been used to examine structure and dynamics in hydrated PFSA membranes. Classical molecular dynamics (MD) simulations have been widely employed to investigate membrane morphology and vehicular diffusion of water molecules/hydronium ions.[4,34–41] For example, Vishnyakov and Neimark[34] explored phase segregation at microscopic level in the hydrated Nafion, and showed that the proton conductivity depends on extent of hydration. Jang et al.[35] explored monomeric sequence effects on phase separation and transport properties in hydrated Nafion. The authors showed that water diffusion is faster in the dispersed sequence

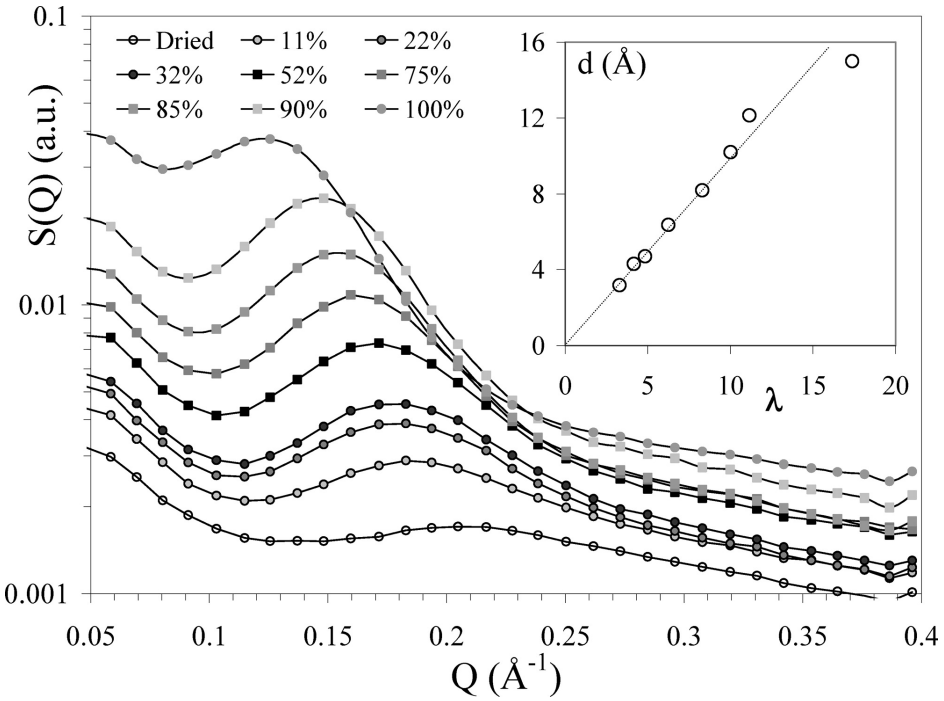

Figure 1.6: SANS structure factors of hydrated Nafion (from dry to saturated). The variation of the mean distance between hydrophobic aggregates d = 2π ($1/Q_0(\lambda)$ - $1/Q_0$ (λ = 0)), where Q_0 is the position of the ionomer peak, as a function of the number of water molecules per ionic group λ, is shown in the inset. Reprinted with the permission from work of Perrin et al.[24] Copyright American Chemical Society.

compared to the blocky sequence. Cui et al.[36] observed the formation of hydrophobic domains and heterogeneous hydrophilic domains in hydrated Nafion. The authors concluded that clustering of water molecules is minimal at low hydration, and large clusters are observed only at higher hydration. Venkatnathan et al.[37] investigated structure and transport in hydrated Nafion. The authors reported that diffusion coefficients of hydronium ions is lower than water. Devanathan et al.[38] characterized nanostructure of hydrated Nafion and observed that sulfonate groups move apart with increasing hydration. The authors observed strong sulfonate-water/hydronium interaction leads to a lower probability of vehicular diffusion of protons at lower hydration. In another study, these authors[39] observed that the mean residence time of water molecules/hydronium ions decreases with

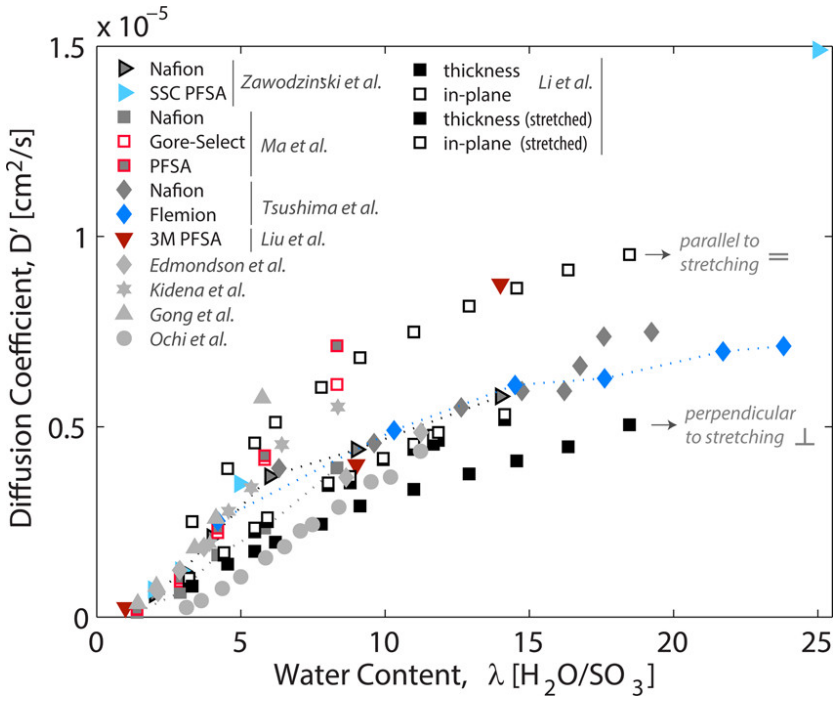

Figure 1.7: Water tracer-diffusion coefficient of PFSA membranes as a function of water content (25–30 °C), compiled from the pulsed field gradient stimulated spin echo (PFGSE)- nuclear magnetic resonance (NMR) data in the literature: Nafion (1100 EW),[25–30] Dow,[25] (Flemion,[28] Gore-Select,[30] 3M,[31] as well as anisotropy of D' and stretching effect for Nafion membrane (from Li et al.[32,33]). Reprinted with the permission from work of Kusoglu and Weber.[12] Copyright American Chemical Society.

hydration. However, the mean residence time for hydronium ions was found to be higher than water molecules. The diffusion coefficients of hydronium ions using MD simulations were found to be in good agreement with quasielastic neutron scattering (QENS) experiments. Sunda and Venkatnathan[40] examined the structure and dynamics of a different PFSA (Aciplex) membrane. The authors observed, that sulfonate-water interactions decrease with increasing hydration similar to the trends seen in hydrated Nafion. The diffusion of hydronium ions in hydrated Aciplex was found to be higher as compared to hydrated Nafion, though the diffusion coefficients of water molecules showed a reverse trend. In a subsequent study, Sunda and Venkatnathan[41] examined structure and dynamics in pendant side chains of Nafion, Dow, and Aciplex (PFSA) in hydrated environments. A

schematic (see Figure 1.8) of variation in chain length from simulations and the change in the nanostructure with an increase in hydration with snapshots is illustrated. The authors concluded that the extra ether oxygen (of pendant side chain of Nafion) leads to enhanced interaction between the sulfonate group and hydrophilic phase.

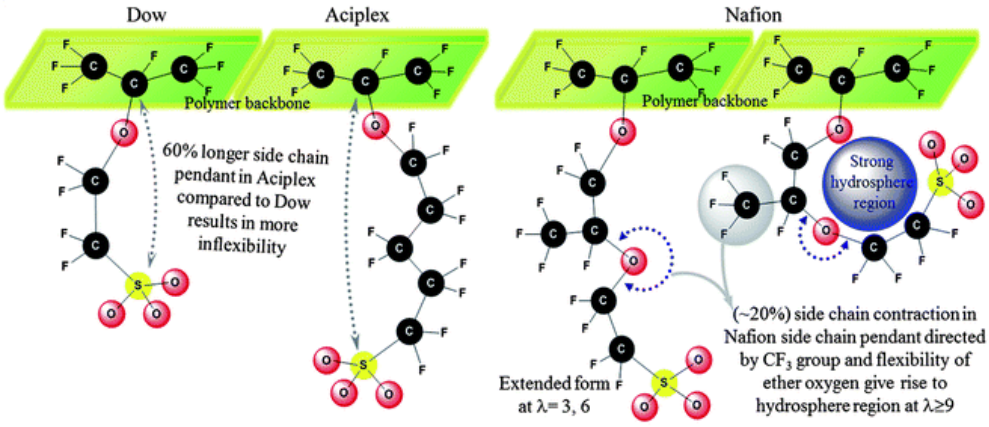

Figure 1.8: Schematic of variation in pendant side chain length. Reprinted with the permission from work of Sunda and Venkatnathan.[41] Copyright Royal Society of Chemistry.

Quantum chemistry calculations have also been used to examine the proton transfer mechanism in membrane fragments and dopants.[42–45] For example, a density functional theory (DFT) study by Paddison[42] showed that the ether oxygen atoms (in pendant side chains of Nafion) are not hydrophilic and attributed it to the strong electron withdrawing effect of the neighboring -CF_2- groups. In a different study, Paddison[43] observed that proton dissociates from the -SO_3H group in the presence of minimum three water molecules. Paddison and Elliott[44] showed that the number of water molecules required to connect these sulfonic acid groups decreases with a reduction in the length of the backbone (-CF_2- groups) (see Figure 1.9). Further these authors[45] examined short-side-chain PFSA membrane and investigated the effects of conformational changes in the backbone with varying water molecules. The authors observed that the membrane backbone could either adopt an elongated form with all C atoms in a trans-state or a folded conformation due to hydrogen

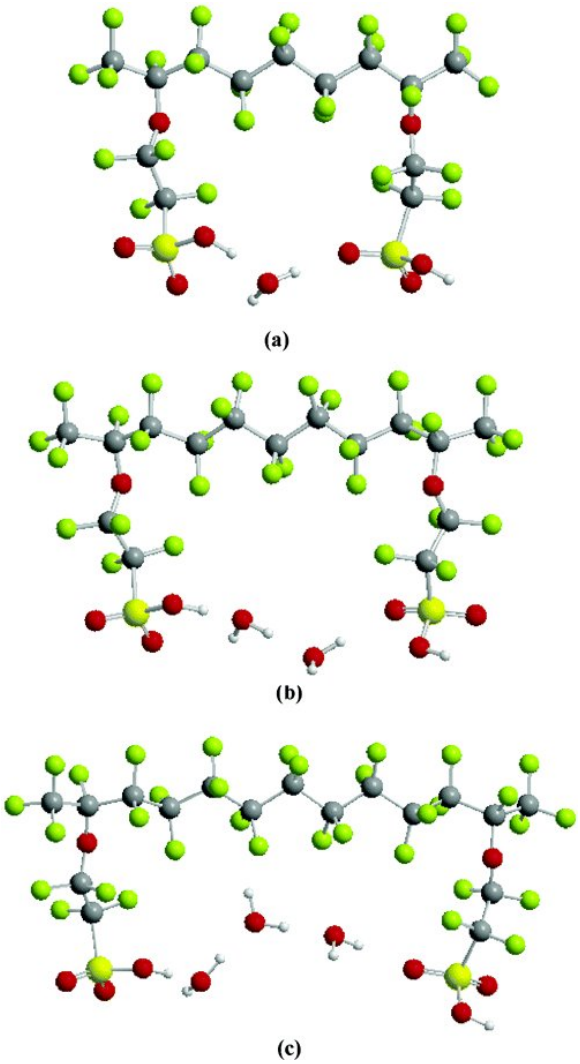

Figure 1.9: Fully optimized (B3LYP/6-311G**) global minimum energy structures of two side chain fragments of the short-side chain perfluorosulfonic acid polymer showing the connectivity of the hydrophilic groups with explicit water molecules: (a) one H_2O connects the sulfonic acid groups in the C_6 fragment; (b) two H_2Os connect the sulfonic acid groups in the C_8 fragment; (c) three H_2Os connect the sulfonic acid groups in the C_{10} fragment. Reprinted with permission from work of Paddison and Elliot.[44] Copyright American Chemical Society.

bonding of the pendant sulfonic acids groups with the water. The authors concluded that a 'kinked' backbone leads to stronger interaction of water with the pendant sulfonic acid groups and also results in proton transfer from the -SO_3H acid group to water with a fewer water molecules (see Figure 1.10).

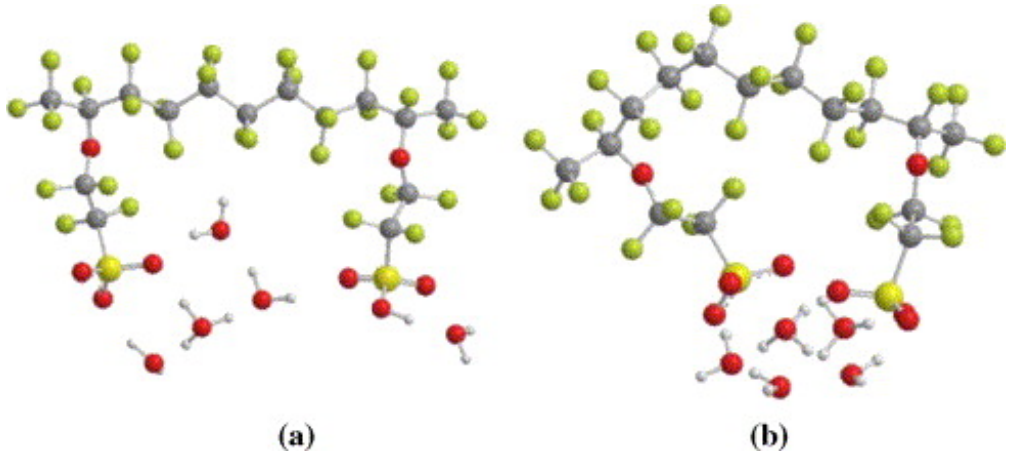

Figure 1.10: Fully optimized (B3LYP/6-311G**) global minimum energy structures of the two side chain fragment with 5 explicit water molecules: (a) dissociation has occurred with only one of the sulfonic acid groups with hydrated proton exhibiting a Zundel-like structure and the PTFE backbone is elongated with the carbons in a trans conformation through out; (b) both protons are dissociated with one as a hydronium ion hydrogen bonded to both sulfonates; the backbone is folded with both the sixth and seventh carbon atoms from the left in nearly cis arrangements. Reprinted with the permission from work of Paddison and Elliott.[45] Copyright Elsevier.

Proton hopping mechanism is also crucial for full understanding of proton conduction. Since this cannot be modeled using classical MD simulations, this has been explored using reactive MD simulations,[47] Self consistent iterative multistate empirical valence bond (SCI-MS-EVB),[46,48–50] and ab initio MD (AIMD) simulations.[51–53] Petersen and Voth[46] employed SCI-MS-EVB to characterize hydrated Nafion. The authors concluded that hopping (discrete component) and diffusion mechanism (continous component) are of similar magnitude and anti-correlated, (see Figure 1.11) which results in an overall lower proton diffusion. Feng and Voth[49] showed occurence of Zundel and Eigen ions depends on the distance from the sulfonate group. Voth and coworkers[50] examined several morphological models (see Figure 1.12) of hydrated Nafion and showed that different models show distinct proton transport patterns and hence different rates of proton diffusion.

Choe and coworkers[51] employed first-principles MD simulations to model proton dynamics in hydrated Nafion. The authors obtained proton diffusion coefficients to be 0.3

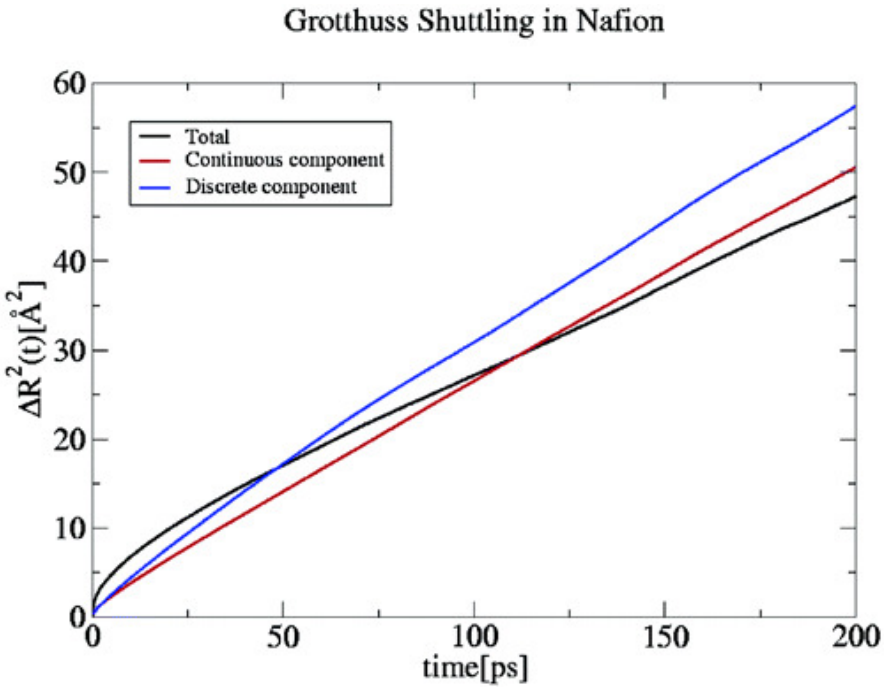

Figure 1.11: Total mean-squared displacement (black) and the continuous (red) and discrete (blue) components of the mean-squared displacement of proton in Nafion. Reprinted with permission from work of Voth and coworkers.[46] Copyright American Chemical Society.

$\times$ 10^{-5} cm^2/s and 7.1 $\times$ 10^{-5} cm^2/s for λ = 4.25 and 12.75, respectively (λ is number of water molecules per sulfonate group). Ilhan and Spohr[52] employed Car–Parrinello MD simulations to examine the nature of water/protons in cylindrical pore consisting of CF_3SO_3H and CF_3–CF_3 molecules (see Figure 1.13). The authors observed that in the first step, protons dissociate and then is transferred from the polymer to water molecules to form an ion pair (sulfonate-hydronium) at λ = 3. The authors concluded that proton transport depends on the continuity of hydrogen bonding network. Devanathan et al.[53] performed AIMD simulations on hydrated Nafion and reported proton diffusion coefficient at λ = 15 to be 0.9 $\times$ 10^{-5} cm^2/s, which is close to the experimental measurements. To summarize, proton conduction in hydrated PFSA membranes varies with hydration, interaction of water with sulfonate groups, length of side-chain, and polymer segmental

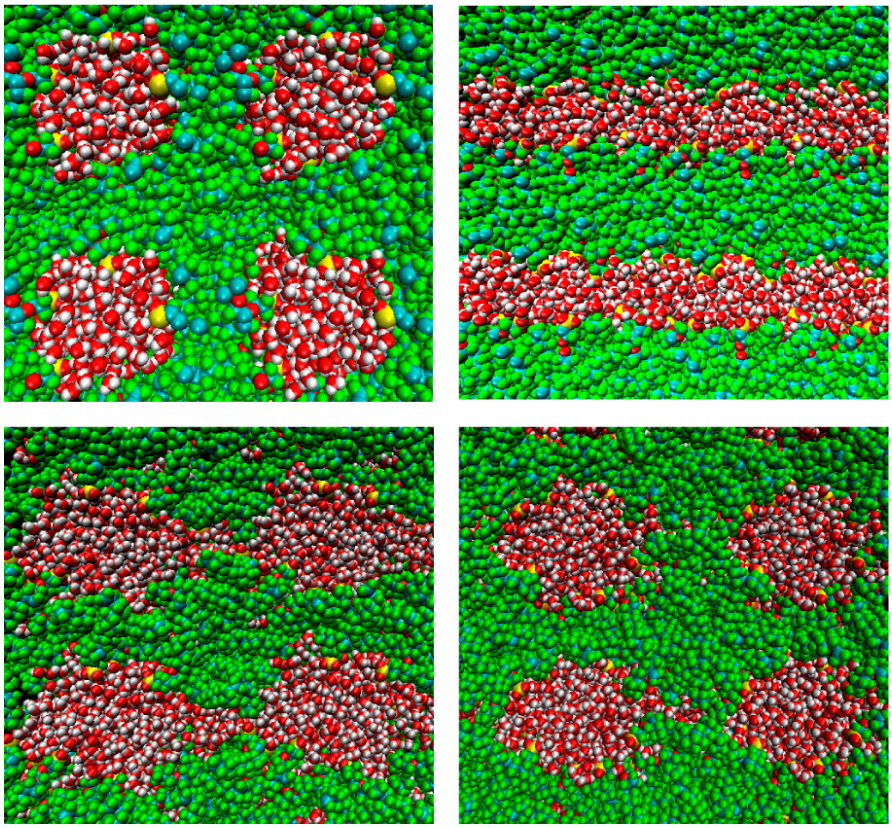

Figure 1.12: Upper left: snapshot of the cylinder-type model at hydration level 15; the axis of the cylinder is on the Z direction. Upper right: snapshot of the lamellar model at hydration level 15. Lower left and right: snapshots of the cluster model from two different perspectives; the clusters are connected on the Z axis. Red spheres represent the oxygen atoms, white spheres represent the hydrogen atoms, yellow spheres represent the sulfur atoms, and the rest represent the Nafion backbone atoms. Reprinted with permission from work of Voth and coworkers.[50] Copyright American Chemical Society.

motions. The challenge in the design of such electrolytic membranes is to enhance the transport properties without undermining the mechanical stability.[12]

1.2 Non-humidified membranes

PEMs which require humidification for proton conduction limit the deployment of these fuel cells with operating temperatures restricted to the boiling point of water. The operation of these fuel cells at higher temperature is also favored to reduce catalyst poison-

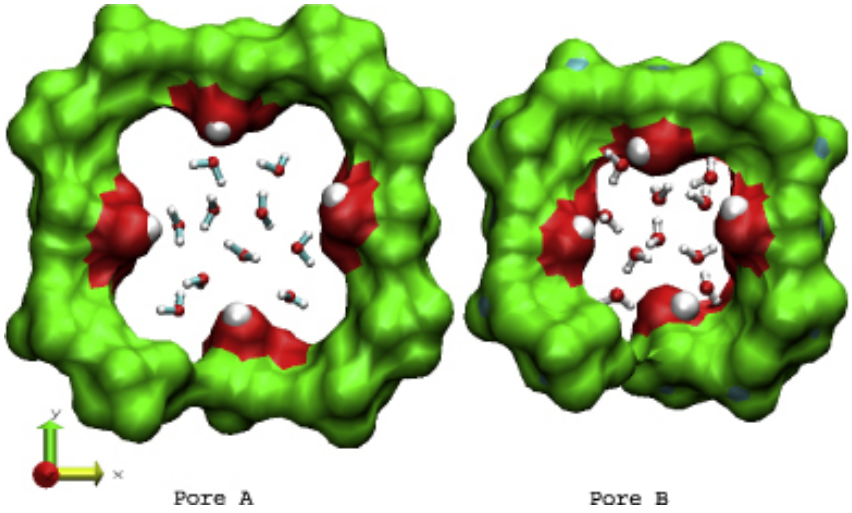

Figure 1.13: Sketch of the model pores for λ = 2.5. The eight CF_3-CF_3 and the four CF_3SO_3H entities are arranged in a helical pattern. Pore atoms are shown as a density map and water molecules as stick models. Printed with permission from work of Ilhan and Spohr.[52] Copyright IOP Publishing.

ing, and hence, suitable alternatives as proton carriers have been explored.[54,55] Aromatic membranes such as ABPBI, PBI doped with phosphoric acid have been explored for high-temperature fuel cells. These membranes possess excellent properties such as high thermal, chemical and mechanical stability, high conductivity at elevated temperatures and are available at low cost.[8,56–61] PBI membrane has a high glass transition temperature (430 °C), excellent chemical resistance, and mechanical strength which stems from the aromatic backbone. These membranes are promising alternatives for the operation of high temperature fuel cells. ABPBI membrane has N atom on imidazole ring which serves as a proton acceptor[56] and can interact with dopants like phosphoric acid. ABPBI, has higher affinity towards phosphoric acid as compared to PBI due to absence of phenyl ring in the former (see Figure 1.2).

Phosphoric acid is amphoteric and has a high boiling point, which makes it a suitable proton conductor for fuel cell applications.[58] The phosphoric acid doped PBI has high proton conductivity (0.07 Scm^{-1}) in fully doped conditions and is comparable to the state-

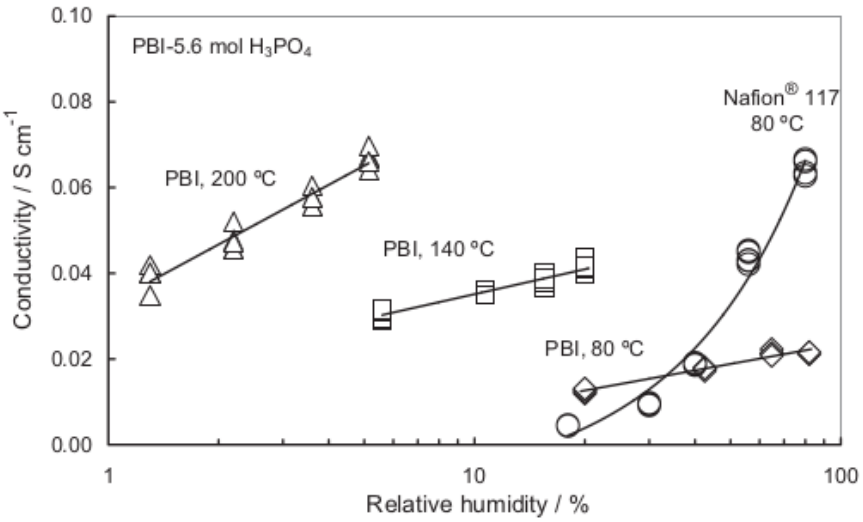

Figure 1.14: Conductivity of Nafion and acid doped PBI membranes as a function of Relative Humidity at different temperatures.[60] Temperatures are indicated in the figure printed from work of Li et al.[61] Copyright John Wiley & Sons.

of-the-art Nafion membrane (see Figure 1.14) at higher temperatures.[61] A few computational studies have been performed on benzimidazole (BIM) based membranes. Pahari et al.[62] investigated structure and dynamics of phosphoric acid doped PBI membranes at a varying concentration of phosphoric acid using MD simulations. The authors observed no phase separation (see Figure 1.15) and phosphoric acid molecules form inter and intramolecular hydrogen bonds at all concentration of phosphoric acid. Venkatnathan and coworkers[63] performed MD simulations to examine structure and dynamics in neat BIM, phosphoric acid, and phosphoric acid-BIM mixtures. The authors observed that diffusion coefficients of BIM decrease with increasing phosphoric acid concentration, whereas the diffusion of phosphoric acid increases. The RDFs showed a strong hydrogen bonding interaction between the imine N of BIM and hydrogen of phosphoric acid. Venkatnathan and coworkers[64] examined structure and dynamics of phosphoric acid doped ABPBI and characterized the effect of polymer chain length (dimer to decamer). The authors observed

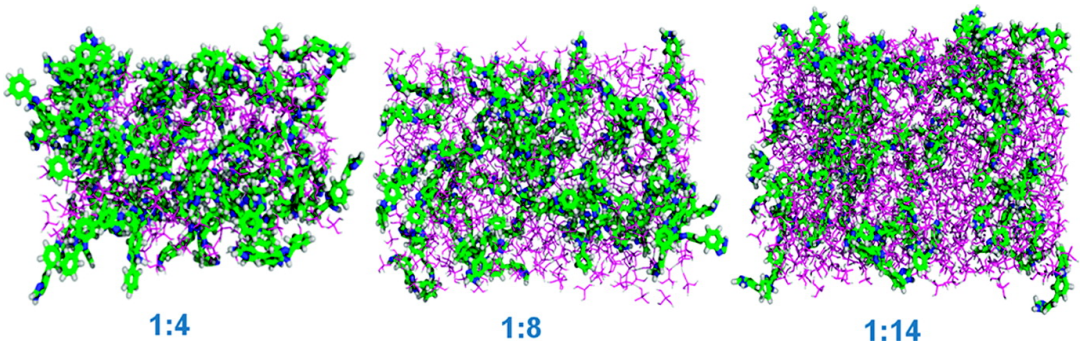

Figure 1.15: Snapshots of PBI–phoshporic acid mixed systems (1:4, 1:8, and 1:14) Reprinted with permission from work of Pahari et al.[62] Copyright American Chemical Society.

that the inter and intra-chain interactions change insignificantly with chain length. The authors proposed decamer to be optimum for computation of structure and dynamics. Pahari and Roy[65] employed MD simulations on phosphoric acid doped PBI and ABPBI. The au-

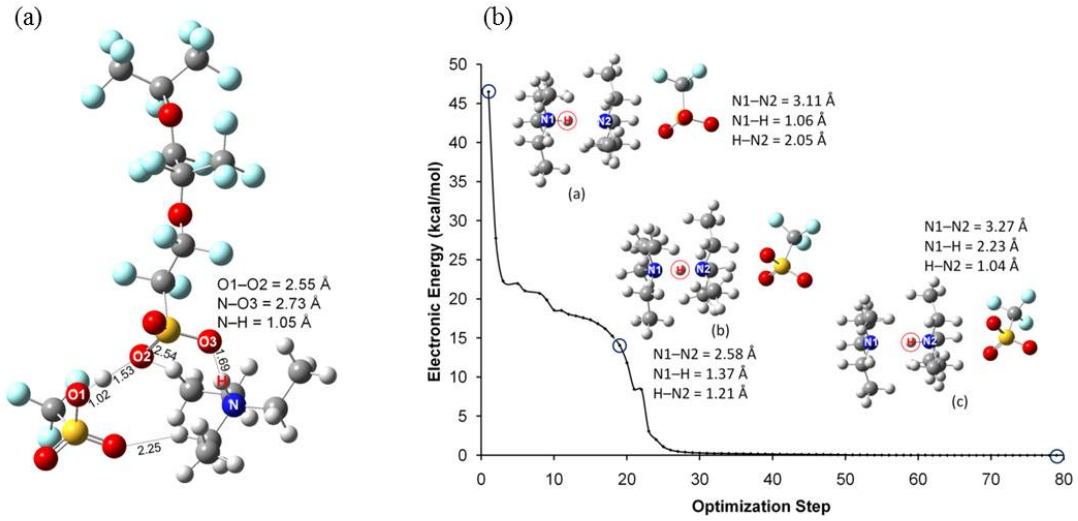

Figure 1.16: (a) Interaction of a Nafion-side-chain fragment with a TEATF IL unit. TFA approaches towards hydrogen atom and $TEAH^+$ towards the oxygen atom of the sulfonic acid end-group of the membrane fragment. (b) Mechanism of proton transfer in a $TEAH^+$...TEA...TFA- complex. Reprinted with permission from work of Kumar and Venkatnathan.[66] Copyright American Chemical Society.

thors showed that ABPBI has more affinity towards phosphoric acid as compared to PBI

due to more number of hydrogen-bonds in ABPBI than in PBI. Iojoiu and co-workers[67] examined triethylamine (TEA)-saturated and triethlyammonium-triflate (TEATF)-doped Nafion and suggested proton transport occurs via cationic clusters. Kumar and Venkatnathan[66] employed quantum chemistry calculations on TEATF-doped Nafion membrane and examined proton transport pathways (see Figure 1.16). The authors proposed that hydrogen bonding interaction of anions, present in the medium, with the free base increases its basicity and thus facilitates faster proton conduction. Shirata and Kawauchi[68]

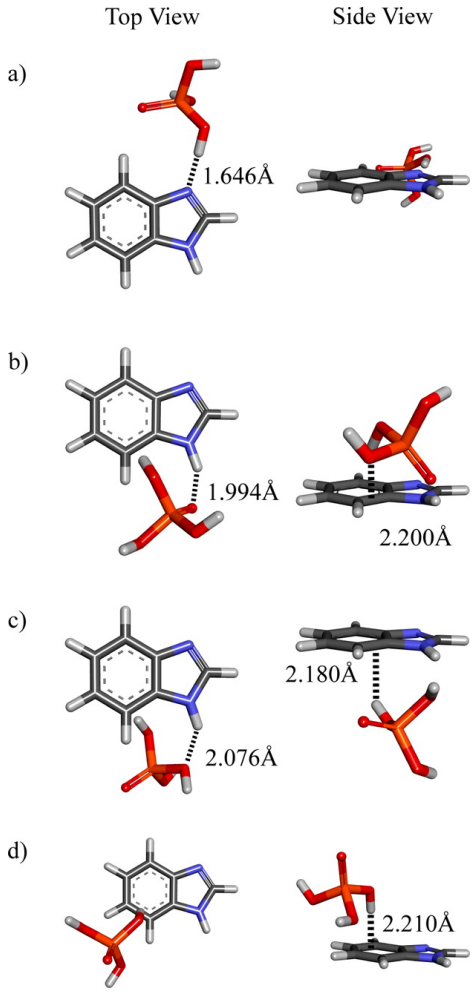

Figure 1.17: Optimized structures of (a) N-type, (b) O-type, (c) OH-type, and (d) π-type interactions at the B97X-D/6-311G(d,p) level of theory. Reprinted with permission from work of Shirata and Kawauchi.[68] Copyright American Chemical Society.

employed DFT calculations to examine the interaction of phosphoric acid with BIM with different configurations. The authors explored several interactions (see Figure 1.17) and observed that N-type to be strongest (followed by O-, OH-, and π-type). Vilčiauskas et al.[69] investigated proton transport mechanism in neat phosphoric acid using AIMD simulations. The authors showed that interplay of polarizable hydrogen-bonds and frustrated hydrogen-bonding is responsible for high proton conductivity. Further, the authors examined proton transfer mechanism, structure, and dynamics in phosphoric acid-imidazole mixtures.[70] However, PBI is preferred due to loss of mechanical strength of ABPBI with increasing concentration of phosphoric acid. Another drawback of ABPBI membrane is its poor solubility in common solvents employed for membrane casting methods.[71] Also, phosphoric acid doped PBI membranes have disadvantages like leaching and condensation of phosphate groups at high temperatures.[72] Hence, alternatives to phosphoric acid such as ILs are explored.

ILs are considered as a promising alternative due to their excellent properties such as high thermal stability, low vapor pressure, wide electrochemical window, and high anhydrous ionic conductivity. These properties make ILs a promising dopant in electrolytic membranes and thus enabling operation of PEM fuel cells at higher operating temperatures (>100 °C). A protic ionic liquid (PIL) is defined as a combination of a Brønsted base and Brønsted acid, where the base accepts a proton from the acid (see Figure 1.18).[73] The use of PILs as proton carriers has been explored for high-temperature

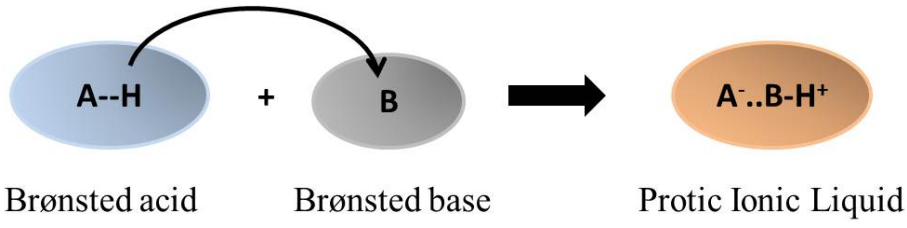

Figure 1.18: Formation of Protic Ionic Liquid.

fuel cells.[73–87] A wide range of PILs as a prospective proton conducting material and underlying proton conduction mechanism in PIL, in PIL with excess of one constituent, or in PIL doped membranes have been investigated for fuel cell applications.[9,73,88–91] Sood et al.[90] demonstrated IL (triethylammmonium trifluoromethanesulfonate, TEAMS) doping in Nafion (neutralized with triethylamine, TEA) enhances the ionic conductivity in anhydrous conditions. The conductivity of IL doped membrane increases with wt% of IL (see Figure 1.19).

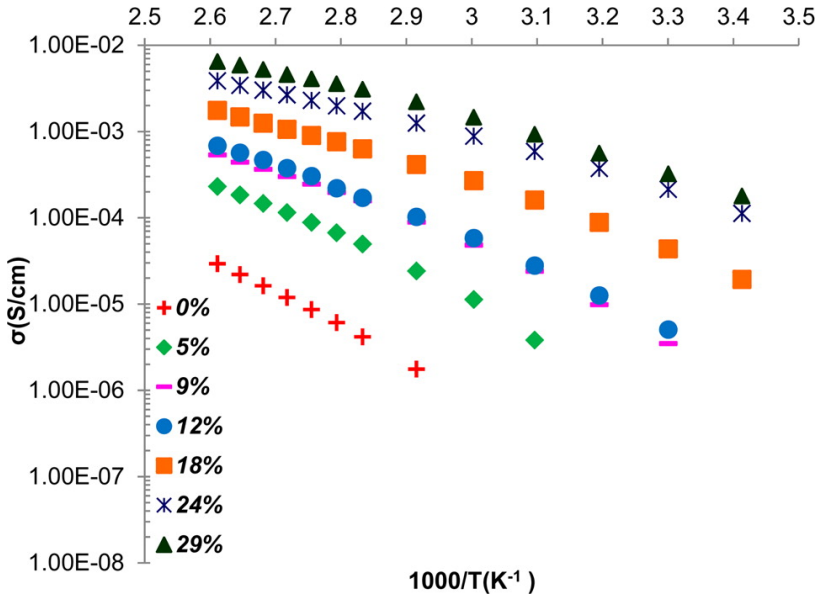

Figure 1.19: Conductivity vs temperature of Nafion–TEA+x%TEAMS (4–29 wt %) under anhydrous conditions. Reprinted with permission from work of Sood et al.[90] Copyright American Chemical Society.

1.3 Molecular dynamics simulations

A chemical system such as an atom, molecule or a macromolecule (polymer, biomolecule) can be represented by a model. The molecular models are constructed using standard softwares (e.g. MOLDEN,[92] Gaussview[93] etc.) and represented as coordinates. The co-

ordinate representation of a chemical system provides information on bonds, angles and dihedrals. The coordinates can be described in cartesian coordinates (xyz) or internal coordinates (Z-matrix). An example of Z-matrix for water molecule is shown in Figure 1.20.

```
O
H          1          B1
H          1          B2          2          A1
B1          0.96
B2          0.96
A1          109.50
1 2 1.0 3 1.0
```

Figure 1.20: Z-matrix of water molecule.

The matrix shows the atoms (O and 2 H atoms) of water molecule, distance between H and oxygen atom is denoted by B1 and B2 respectively and the angle H-O-H is denoted by A1. The coordinates can be extracted from experiments such as XRD or NMR. The visualization of these models play an important role in understanding various physical and chemical processes. Some of the most commonly used molecular visualization softwares are VMD[94] and Chimera.[95] For example, a visual representation of a polymer in CPK representation is shown in Figure 1.21.

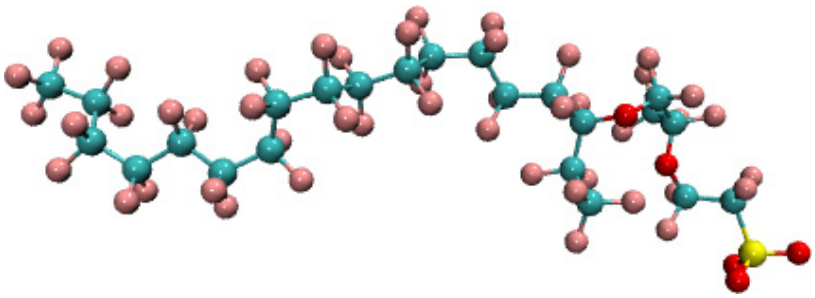

Figure 1.21: Visual CPK representation of a polymer.

MD simulations are based on Newton's equations of motion where the forces between atoms are derived from an empirical potential. The force field (which depends on coordinates) or total potential energy (V_{total}) can be written as:

$$V_{total} = \underbrace{V_{bonds} + V_{angles} + V_{torsion}}_{V_{bonded}} + \underbrace{V_{electrostatic} + V_{vdw}}_{V_{non-bonded}} \tag{1.4}$$

$$V_{bonded} = \sum_{bonds} \frac{k_b}{2}(r - r_0)^2 + \sum_{angle} \frac{k_\theta}{2}(\theta - \theta_0)^2 + \sum_{torsion}^{n=0-5} C_n(\cos(\psi))^n \tag{1.5}$$

k_b and k_θ are force constants for bonds and angles respectively, r_0 is the equilibrium bond length and θ_0 is the equilibrium bond angle. C_n is called the torsional coefficient, ψ = ϕ-180°, where ψ is a torsion angle. The non-bonded potential ($V_{non-bonded}$) energy is defined as:

$$V_{non-bonded} = \sum_{ij} 4\epsilon_{ij} \left[\left(\frac{\sigma_{ij}}{r_{ij}} \right)^{12} - \left(\frac{\sigma_{ij}}{r_{ij}} \right)^{6} \right] + \frac{1}{4\pi\epsilon_0} \frac{q_i q_j}{\epsilon_r r_{ij}} \tag{1.6}$$

where, ϵ_{ij} is the depth of potential well, r_{ij} is the distance between atoms, σ_{ij} is the distance at which potential energy is zero, q_i and q_j are the charges on atom i and j. ϵ_r is the dielectric constant and ϵ_0 is permittivity of vacuum. The force-field parameters can be obtained from experiments or quantum chemistry calculations. The accuracy of simulations and calculation of macroscopic properties depends on the choice of force-field parameters. Broadly, force fields are classified as all-atom force fields, united atom force fields, coarse-grained force fields and reactive force fields. The commonly used classical force fields are CHARMM,[96] AMBER,[97] OPLS-AA,[98] COMPASS,[99] GROMOS,[100] etc. Among these, the OPLS-AA force field is widely used to study ILs and polymer membranes.[40,101–103]

1.4 Quantum chemistry methods

The objective of quantum chemistry methods is to solve the time independent Schrödinger equation,[104] which is written as:

$$\hat{H}\Psi_i = \mathrm{E_i}\Psi_i \tag{1.7}$$

Ψ_i is the wave function and represents the state of chemical system under investigation i^{th} state. $\mathrm{E_i}$ is the energy of the system in the i^{th} state and $\hat{H}$ is the Hamiltonian operator for any chemical system. Since nuclei are heavier than electrons, the nuclei are assumed to be static, where electrons can move in the field generated by the nuclei. Thus, using Born-Oppenheimer approximation[104] the nuclear kinetic energy term is neglected and the nuclei-nuclei repulsion term is kept as constant and the and the corresponding Schrödinger equation can be written as:[104]

$$\begin{aligned} \hat{H}_{elec}\Psi_{elec} &= E_{elec}\Psi_{elec} \\ E_{total} &= E_{elec} + E_{nucl} \end{aligned} \tag{1.8}$$

where $\hat{H}_{elec}$ is called as electronic Hamiltonian operator; Ψ_{elec} represents electroninc wavefunction and the corresponding energy is denoted by E_{elec}; E_{nucl} represents nuclear energy and E_{total} is total energy. Some of the most popular quantum chemistry methods are DFT, Møller–Plesset perturbation theory, configuration interaction, coupled cluster, multi-configurational self-consistent field etc. Among these methods, DFT is used due to relatively lower computational cost to investigate large molecular systems. A brief description of DFT is presented in the next section.

1.4.1 Density functional theory

DFT[105,106] uses the electron density, *n(r)*, as a central quantity. The ground state energy (E_0) is written as:

$$E_0 = \int n(r)\nu(r)dr - \frac{1}{2}\sum_{i=1}^{N} < \psi_i|\nabla_i^2|\psi_i > + \frac{1}{2}\int\int \frac{n(r)n(r')}{|r-r'|}drdr' + E_{xc}[n(r)] \quad (1.9)$$

where $\nu(r)$ is the external potential. The second term denotes the kinetic energy of a non-interacting system. The third term is the classical expression for the interaction energy. The fourth term (E_{xc}) is the exchange correlation energy. The Kohn-Sham equations are (in principle) exact, if an appropriate E_{xc} can be determined. In the next section, exchange correlational functionals are briefly discussed.

1.4.2 Exchange correlation functionals

The exchange-correlation functionals are classified as follows:

1.4.2.1 Local-density approximation (LDA)

The local density approximation (LDA) for the exchange and correlation energy is as follows:

$$E_{xc}^{LDA}[n(r)] = \int n(r)\ \epsilon_{xc}^{LDA}(n(r)\ \ dr \quad (1.10)$$

where $E_{xc}^{LDA}[n(r)]$ is the exchange-correlation energy per particle of the homogeneous electron gas of density $[n(r)]$. The common LDA functionals are Perdew-Zunger (PZ)[107] Perdew-Wang (PW),[108] and Vosko-Wilk-Nusair (VWN).[109]

1.4.2.2 Generalized-gradient approximation (GGA)

Since the electron density is typically not spatially uniform which implies LDA approach has limitations. The correlation functional can be improved by invoking its dependence

on local value of density as well as the extent to which the density changes locally. The exchange correlation functional with the GGA depends on the density and its gradient and is written as:

$$E_{xc}^{GGA}[n(r)] = \int n(r)\ \epsilon_{xc}^{GGA}(n(r),\ |\Delta n(r)|)\ dr \tag{1.11}$$

Some examples of GGA functionals are: Perdew, Burke and Ernzerhof (PBE)[110] and BLYP (Becke correlation functional; Lee, Yang, Parr).[111]

1.4.2.3 meta-GGA and hybrid functionals

The functionals which involve the second derivative of the electron density are termed as meta-GGA functionals.[112,113] Additionally, these functionals implement higher derivatives of electron density/kinetic energy density and its gradient. A few examples of meta-GGA functionals are B95, B98, TPSS etc. The hybrid functionals are combination of the Hartree-Fock exchange and DFT exchange-correlation. Some examples of exchange correlation functionals used in computational chemistry are: B3LYP,[109,114–116] M05,[117] M05-2X,[117] M06-2X,[118] B97-D (Becke's 97 Dispersion).[119]

1.5 Scope of the thesis

The objective of the thesis is to examine structure, dynamics and proton transport in polymer electrolyte membranes using MD simulations and quantum chemistry calculations. The detailed theoretical principles of MD simulations are available elsewhere.[120–123] The detailed theoretical principles of quantum chemistry calculations can be seen elsewhere.[104,105] The rest of the thesis is organized as follows: **Chapter 2** describes the effect of atomic charge delocalization on the pendant side chain of hydrated Nafion membrane on the structural (radial distribution functions (RDFs), cluster analysis) and dynamical properties (mean square displacement (MSD), diffusion coefficients and ionic con-

ductivity) using MD simulations. **Chapter 3** describes structure and dynamics of N,N-diethylmethyl ammonium triflate doped PBI membrane using MD simulations. **Chapter 4** describes proton conduction in imidazolium methanesulfonate (IMMSA) IL with varying imidazole (IM) concentration using DFT. **Chapter 5** presents the key findings from previous chapters, followed by a short discussion on possible future directions.

———⊛———⊛———⊛———

Chapter 2

Charge Delocalization Effects on Nafion Structure and Water/Proton Dynamics in Hydrated Environments

2.1 Introduction

In this chapter, the effect of charge delocalization (on the pendant side chain of Nafion) on structure and dynamics is explored. A description of literature from computational investigations on the effect of atomic charges on structure and dynamics in hydrated Nafion is presented. Paddison[43] employed quantum-chemistry calculations on hydrated model polymers and concluded that the excess electron density on the sulfonate group (due to the dissociation of a proton from the sulfonic acid group) is delocalized by the neighboring electron withdrawing CF_2 groups on the Nafion pendant side chain. Eikerling et al.[124] performed DFT calculations on hydrated sulfonyl imide moieties and reported that the microscopic details of charge separation due to dissociation of proton and charge delocalization are essential for the understanding of proton/water mobility. Mikami et al.,[125] using DFT calculations, examined the intermolecular hydrogen bonding interactions between $CF_3O(CF_2)_2SO_3^-$ and water, and showed that the interaction of water molecule is stronger with the oxygen atom of the sulfonate group compared to ether oxygen atoms. In another study, Vila and Mosquera[126] reported a reduction in the proton affinity of the

ether oxygen due to fluorination of ether moieties.

Vishnyakov and Neimark[127] used MD simulations and showed that the CF_2 groups and ether oxygen atoms closest to the sulfonate groups of the pendant side chain of Nafion possess a substantial negative charge. Urata et al.[128,129] showed that the hydrophobic behavior of ether oxygen atoms is due to the electron withdrawing effect of fluorination. Urata et al.,[130] using MD simulations, observed that water molecules have a preferential binding with the sulfonate groups of pendant side chain of Nafion. Wu et al.[131] have shown that simple mixing rules for non-bonded interactions between the oppositely charged ions lead to incorrect results and can lead to the overestimation of the hydronium ions binding to the sulfonate groups.[132] Voth and coworkers[133] reported sulfonate-hydronium ion interaction has minimal influence on the proton diffusion.

Spohr et al.[134] investigated the effects on the proton diffusion of the charge delocalization on the sulfonate groups, the motion of the sulfonate groups and the side chains using the empirical valence bond model. The authors employed side chains attached to the cylindrical walls and excluded the hydrophobic backbone of the membrane in their study. The authors proposed that the charge delocalization on the pendant side chain of the Nafion membrane is one of the critical factors which affect proton conduction. However, there have been no MD simulation study on full PFSA membrane or other functionalized membranes under hydrated conditions to understand the effects of the charge delocalization on structural and dynamical properties. This is important since the hydrophobic parts of PFSA membranes form a continuous phase separate from the water phase and, hence, affect the morphology of water domains. Under varying charge delocalization, this hydrophobic phase could change morphology and in turn, impact the water cluster morphology.

In this chapter, we performed classical MD simulations (T = 353 K) on hydrated Nafion with varying charge delocalization on its pendant side chain. Properties such as

i) intermolecular RDFs ii) the clustering of water molecules and iii) the diffusion coefficients of water molecules and hydronium ions were calculated. Since classical MD simulations cannot account for proton hopping mechanism, only the vehicular diffusion of proton (hydronium ions) is calculated. The remaining part of the chapter is organized as follows: Section 2.2 describes the computational details of the MD simulations of charge delocalization on various hydrated Nafion mixtures, Section 2.3 presents the effects of the charge delocalization on RDFs, water clusters and diffusion coefficients.

2.2 Computational details

The chemical structure of a Nafion monomer is shown in Figure 2.1a. GROMACS 4.6.7 [135] software was used to perform MD simulations. The force-field parameters for the Nafion backbone were taken from the OPLS-AA force-field database. [98] The charge delocalization was modeled by using the unscaled charges on the pendant side chain of Nafion (obtained from the study of Sunda and Venkatnathan [41]). For example, q = 0.70q_0 is obtained using q_0 = 0.75 (q_0 is denotes unscaled charge and is the total charge on the sulfonate group). Similarly, other charge models such as q = 0.63q_0, 0.50$_0$, 0.38$_0$ and 0.25$_0$ were also employed. Depending on the charge model (q), the remaining charge was distributed equally on the remaining pendant side-chain atoms of Nafion. The input configurations are obtained as follows: A single decamer chain of Nafion along with 10 hydronium ions was energy minimized and replicated 48 times. The equivalent weight (EW) of the membrane is 1100 which is defined as the weight of the polymer divided by the number of sulfonate groups. The resultant mixture, containing 48 Nafion chains and 480 hydronium ions, was used as an input for the simulated annealing by warming from (at 50 K/250 ps) 353 K to 1000 K and cooled back (at the same rate) to 353 K, with a total simulation time of 8.25 ns. The final system obtained from the annealing procedure was solvated with

(a) 1440 water molecules corresponding to the hydration value of $\lambda = 3$, where λ denotes the number of water molecules per sulfonate group, (b) 4320 water molecules, which corresponds to $\lambda = 9$ and (c) 7200 water molecules corresponding to $\lambda = 15$. The typical configuration of a hydrated Nafion mixture is shown in Figure 2.1b. The hydrated config-

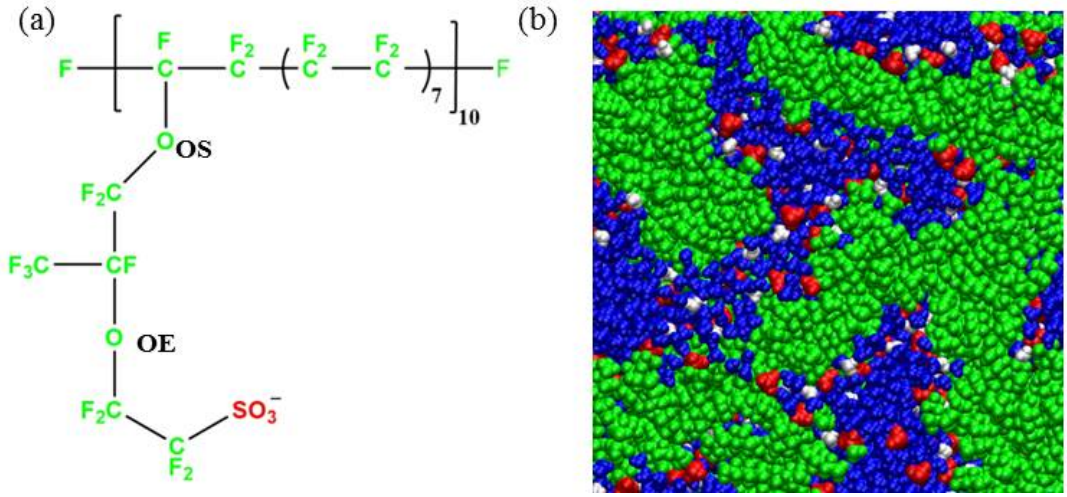

Figure 2.1: (a) The molecular structure of the Nafion decamer (EW = 1100) simulated in the present study. 48 Nafion chains have been placed with 480 hydronium ions and different amounts of water molecules. (b) A snapshot ($\lambda = 15$) illustrating Nafion (green color) with sulfonate groups shown in red color, the blue color represents water, and hydronium ions are shown in white.

urations were energy minimized further using the steepest descent algorithm. The cut-off for the non-bonded interactions was set to 1.2 nm, and the leapfrog algorithm was used to integrate the equations of motion with a time step of 1 fs. The hydrated Nafion mixtures were equilibrated for 20 ns using the NPT ensemble. The Berendsen[136] barostat was used to maintain 1 bar isotropic pressure. The velocity-rescale thermostat, with a coupling time of 0.1 ps, was used to keep a fixed temperature. The particle mesh ewald (PME)[137] method was used for the calculation of the long-range electrostatic interactions. The equilibration was followed by a 35 ns production run using the NVT ensemble controlling the temperature by the Nosé–Hoover[138] thermostat. The trajectories were recorded every 5 ps

to analyze the structural and dynamical properties of all hydrated Nafion configurations.

The simulated densities at λ = 3, 9 and 15 are 1.75, 1.68 and 1.59 g/cm^3 respectively are in good agreement with work of Venkatnathan et al.[37] and Wise et al.[139] The simulated densities (see Figure 2.2) show insignificant change with charge delocalization.

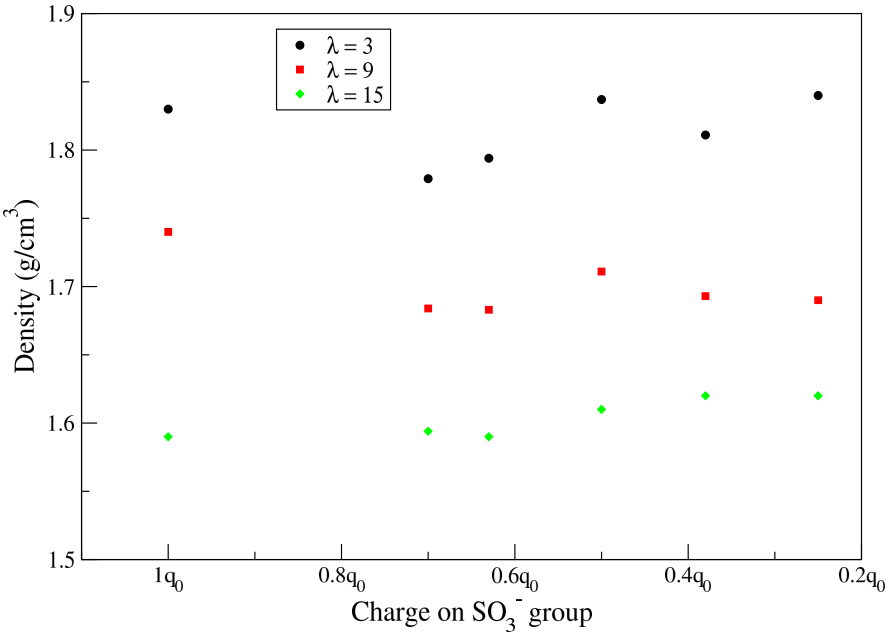

Figure 2.2: The simulated densities for hydrated Nafion mixtures at T = 353 K, for different charge delocalization and hydration levels.

2.3 Results and discussion

2.3.1 Radial distribution functions

The RDF ($g_{AB}(r)$) is calculated as:[123]

$$g_{AB}(r) = \frac{1}{\langle \rho_B \rangle_{local}} \frac{1}{N_A} \sum_{i \in A}^{N_A} \sum_{i \in B}^{N_B} \frac{\delta(r_{ij} - r)}{4\pi r^2} \tag{2.1}$$

where, N_A and N_B is the number of *A* and *B* particles respectively, r_{ij} is the distance between i^{th} and j^{th} particle, $\langle \rho_B \rangle_{local}$ is the particle density of type B at a distance r, averaged over all spheres around particles A.

In a review article by Devanathan,[10] the author has reported that the width of the water channel and the proton conductivity of hydrated Nafion membranes, is closely related to the distribution of the sulfonate groups. This distribution can be characterized by sulfur-sulfur (S-S), RDF.[40] Figure 2.3 shows the S-S RDF at T = 353 K and with charge delocalization (decreasing charge on the sulfonate group). At λ = 3 (q_0) the peak maximum in S-S RDFs appears at 6.0 Å and further decreases to 5.2 Å (0.25q_0). At λ = 9 (q_0) the peak maximum appears at 6.2 Å and shifts to 5.0 Å (0.25q_0). Similarly, at λ = 15 (q_0) the peak maximum at 6.4 Å shifts to 5.0 Å (0.25q_0) with an increase in charge delocalization. The peak maximum at λ = 15 (q_0) is in agreement with previously reported results.[35,37,130,140] The S-S RDFs suggest that increasing charge delocalization (corresponding to decreasing charge on sulfonate groups) leads to a very pronounced shift of the first maximum to the smaller distances. The shift in peak maximum is observed for all simulated water concentrations. Hence, increased charge delocalization leads to the obvious reduced repulsion between the sulfonate groups. Paddison and coworkers[141] have shown that the proton dissociation occurs at lower hydration and with lower energy barriers if the separation between side chains is reduced. Hence, it can be concluded that the charge delocalization could influence proton transfer due to the decreased separation between the sulfonate groups.

To characterize the interactions between the sulfonate groups and water/hydronium molecules, the corresponding RDFs between the sulfur (S) and the water oxygens (OW)/ hydronium oxygens (OH) were calculated (see Figures 2.4 and 2.5). The position of the peak maximum for S-OW RDFs (see Figure 2.4) shifts slightly towards larger distances with increasing charge delocalization which implies a slight decrease in S-OW interac-

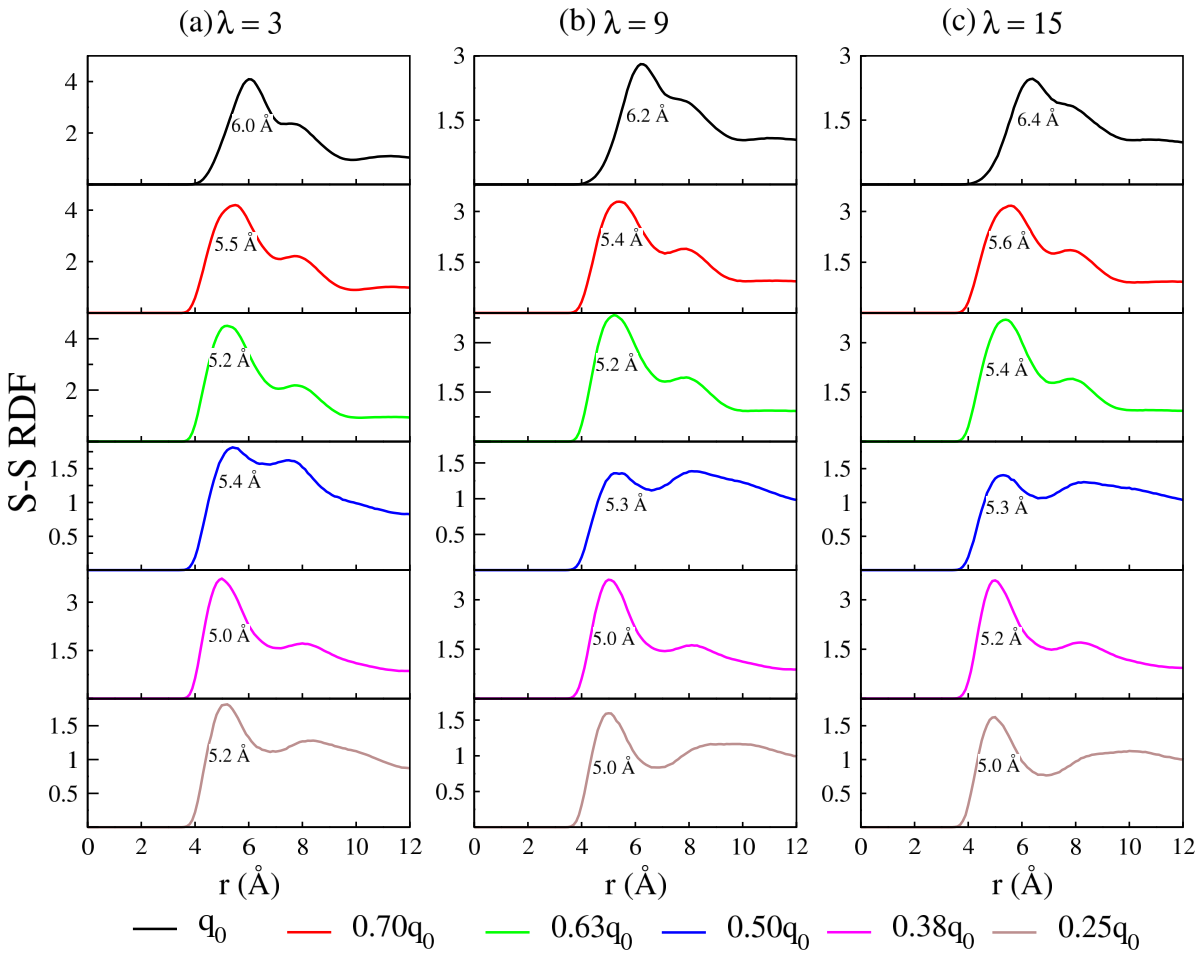

Figure 2.3: S-S RDFs, at (a) λ = 3 (b) λ = 9 and (c) λ = 15, with varying charge (q_0, $0.70q_0$, $0.63q_0$, $0.50q_0$, $0.38q_0$, and $0.25q_0$) on the sulfonate group. The position of the RDF peak maximum is shown within the graphs.

tions leading to the larger separations.

The peak maximum in S-OW RDFs is observed at 3.9 Å (q_0) which is in agreement with the work of Venkatnathan et al.[37] The value of peak maximum shifts to 4.3 Å ($0.25q_0$), with an increase in charge delocalization. Similarly, the peak maximum for S-OH (sulfur and hydronium) RDF (see Figure 2.6). shifts slightly to larger distances with increasing charge delocalization. To understand the interactions of the water molecules with pendant side chain oxygen atom (labeled as OE and OS in Figure 2.1a of Nafion)

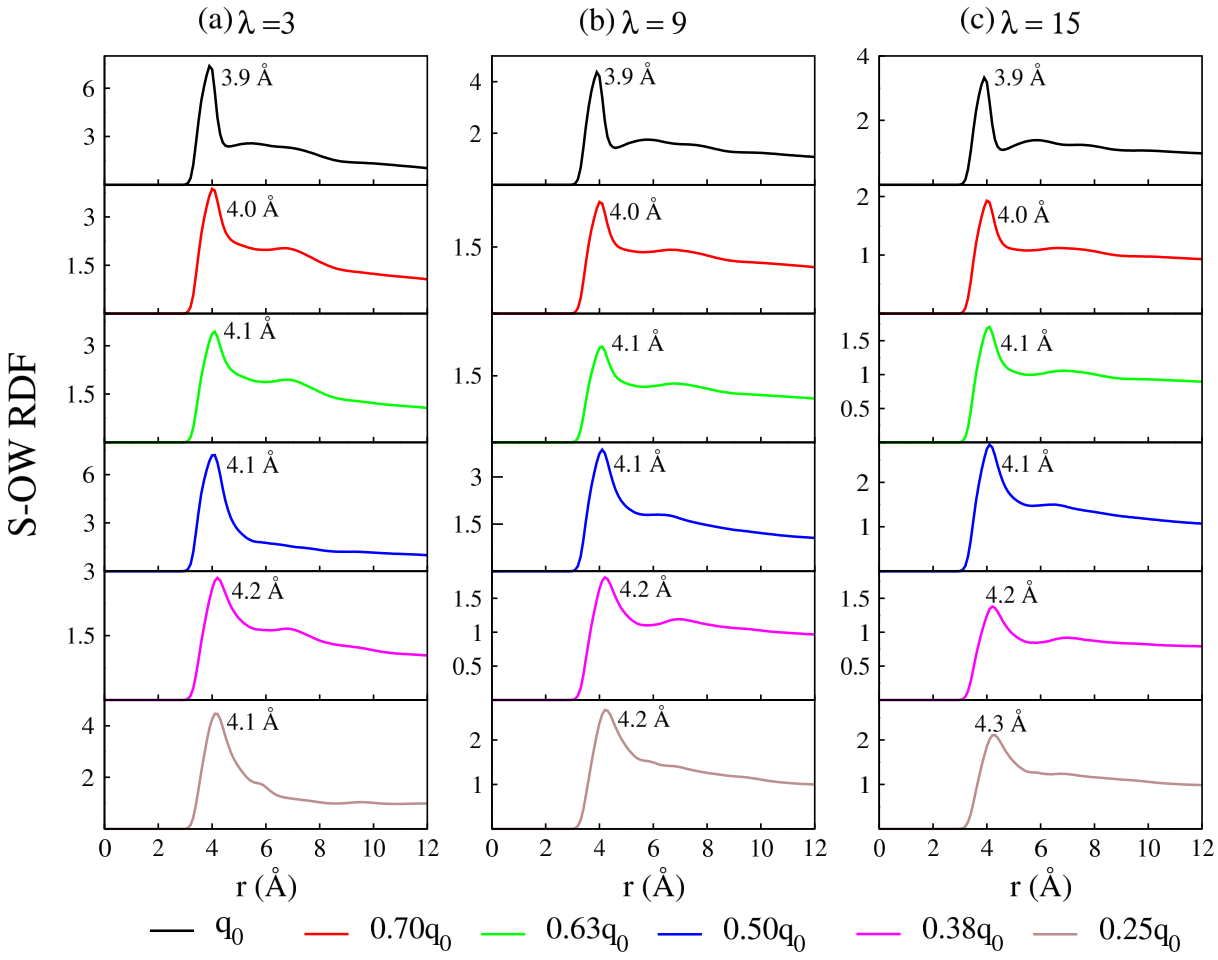

Figure 2.4: S-OW RDFs at (a) $\lambda = 3$ (b) $\lambda = 9$ and (c) $\lambda = 15$, with varying charge (q_0, $0.70q_0$, $0.63q_0$, $0.50q_0$, $0.38q_0$, and $0.25q_0$) on the sulfonate group. The position of the RDF peak maximum is shown within the graphs.

OE-OW and OS-OW RDFs were also calculated (Figure 2.8). These RDFs suggest that at the highest charge delocalization ($0.25q_0$) the interactions of water molecules with the pendant side chain oxygen atoms are significantly increased as compared to the lowest charge delocalization (q_0).

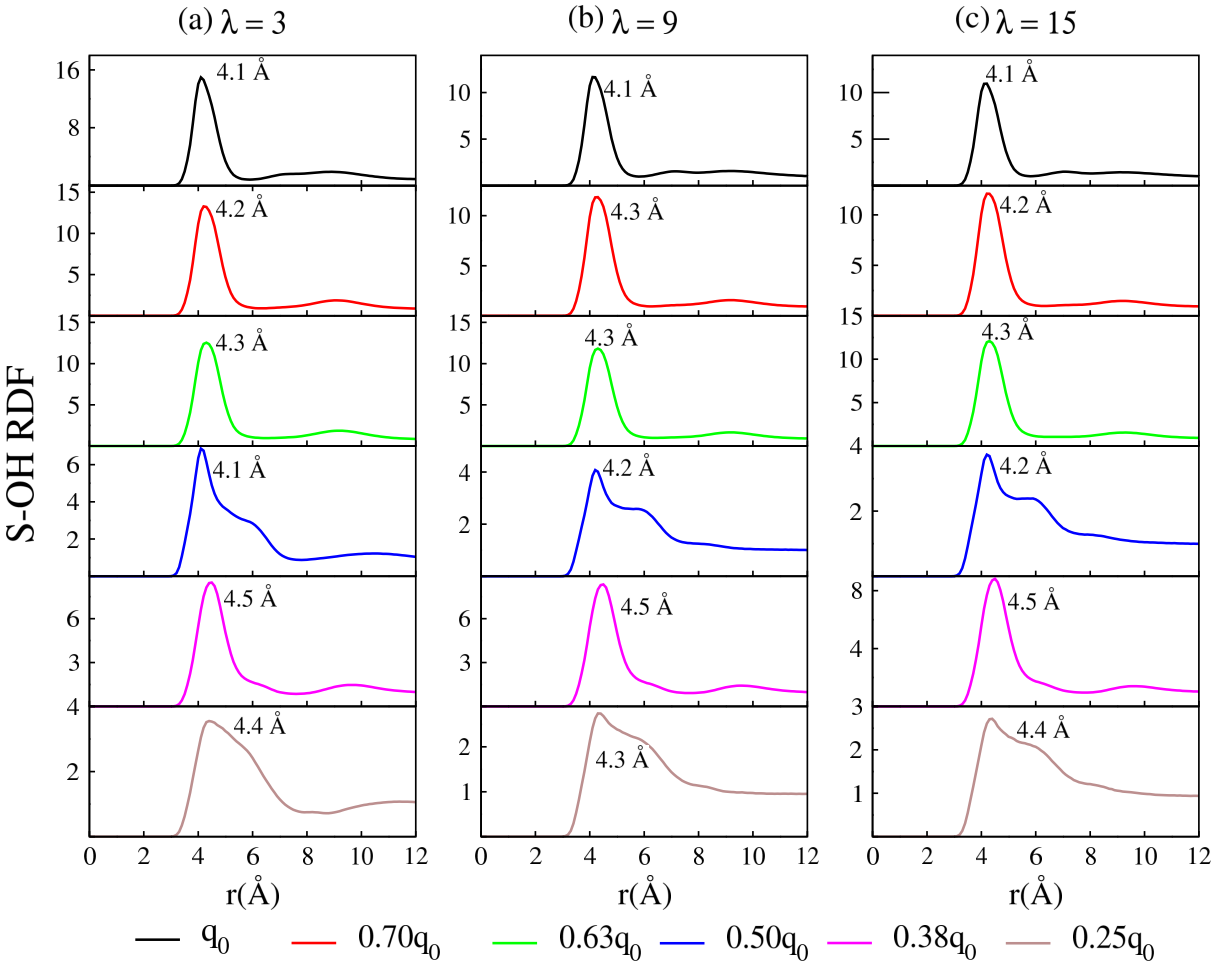

Figure 2.5: S-OH RDFs at (a) $\lambda = 3$ (b) $\lambda = 9$ and (c) $\lambda = 15$, with a varying charge (q_0, $0.70q_0$, $0.63q_0$, $0.50q_0$, $0.38q_0$, and $0.25q_0$) on the sulfonate group. The position of the RDF peak maximum is shown within the graphs.

2.3.2 Water cluster distribution

The Nafion side chains are hydrophilic due to the presence of the sulfonate groups. In hydrated environments, this results in phase separation and leads to the formation of the water clusters which is important for proton conduction.[142] Prior studies[34,36,143,144] have reported a change in the cluster size distribution with varying hydration, from isolated water molecules (at lower water concentration) to larger water domains (for higher wa-

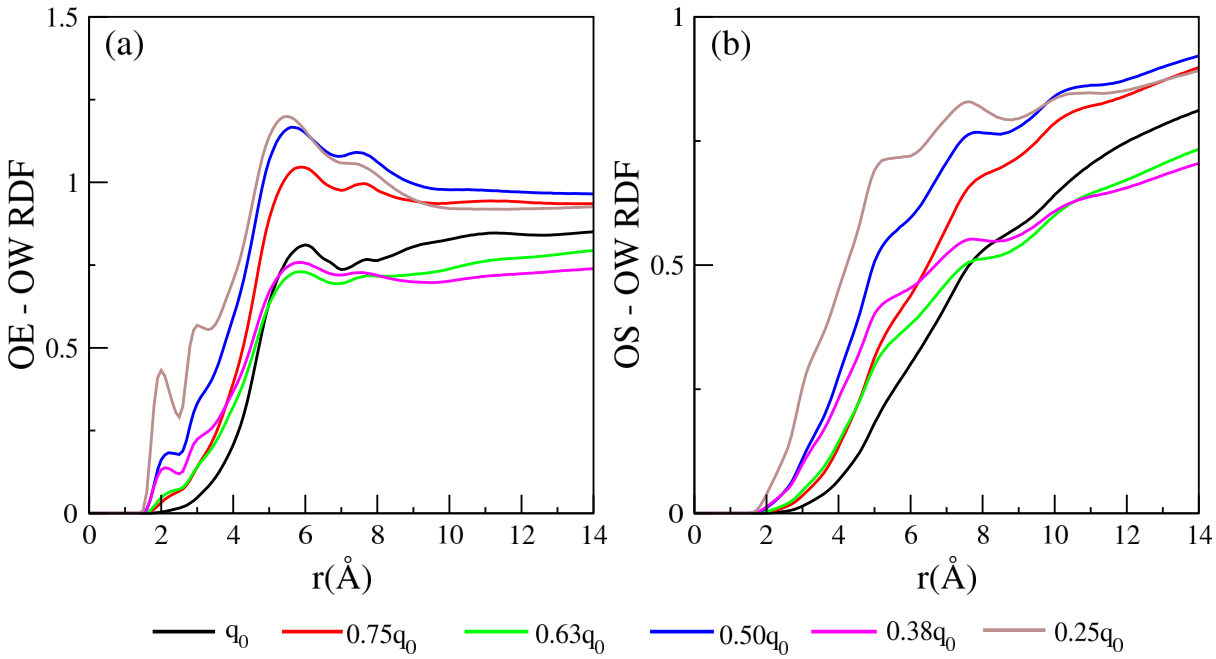

Figure 2.6: RDFs of the pendant side-chain oxygen atoms with water molecules. (a) OE-OW (b) OS-OW at λ = 15 (where OE and OS are oxygen atoms present in the side chain and OW is oxygen atom of water molecule).

ter concentration). The formed water clusters facilitate proton conduction. Hence, it is important to understand the effect of the charge delocalization on the clustering of water molecules. In this work, the water molecules were considered to be clustered if the minimum distance between water molecules (oxygen atoms) was less than 3.6 Å (distance is close to the first solvation shell).[145] The average cluster size was calculated as where N is the number of clusters of a particular size, C_s is the size of a cluster of water molecules and n is the total number of clusters.

$$Avg = \frac{\sum_{s=1}^{n} NC_s}{\sum_{s=1}^{n} C_s} \tag{2.2}$$

Figure 2.7a shows the average water cluster size with charge delocalization at different hydration levels. At lower hydration (λ = 3), water clusters could not be observed in this

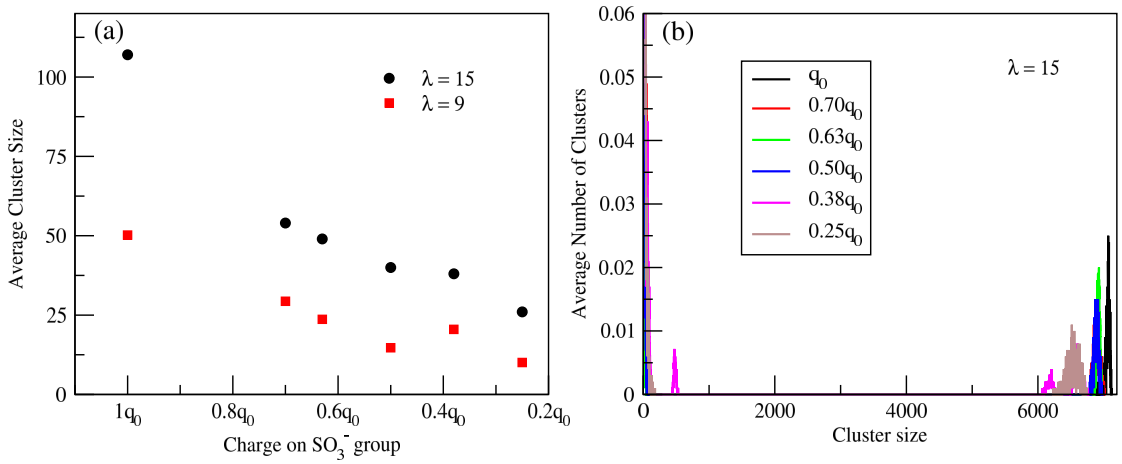

Figure 2.7: (a) The average cluster size of the water molecules at a cut-off of 3.6 Å and T = 353 K, λ = 15 and λ = 9 and (b) the average number of clusters at λ =15 with charge delocalization.

work and is consistent with the findings of Devanathan et al.[146] Further, water cluster sizes decrease monotonically with the increase in charge delocalization, which implies decreasing phase separation. It can be seen from Figure 2.7b that the largest water cluster is observed for the charge q_0; the size of the largest cluster decreases with an increase in the charge delocalization.

2.3.3 Water diffusion and Hydronium transport

The translational diffusion coefficients of water molecules and hydronium ions were calculated by analyzing their MSD using the Einstein relation,[123]

$$\lim_{(t\to\infty)} \langle \|r_i(t) - r_i(0)\|^2 \rangle_{i\in A} = 6D_A t \tag{2.3}$$

where, r_i is the center-of-mass position of molecule, $r_i(0)$ and $r_i(t)$ are positions of atoms at time t = 0 and t respectively. D_A is the self-diffusion coefficient calculated from the linear regime of the corresponding MSD (Figure 2.8).

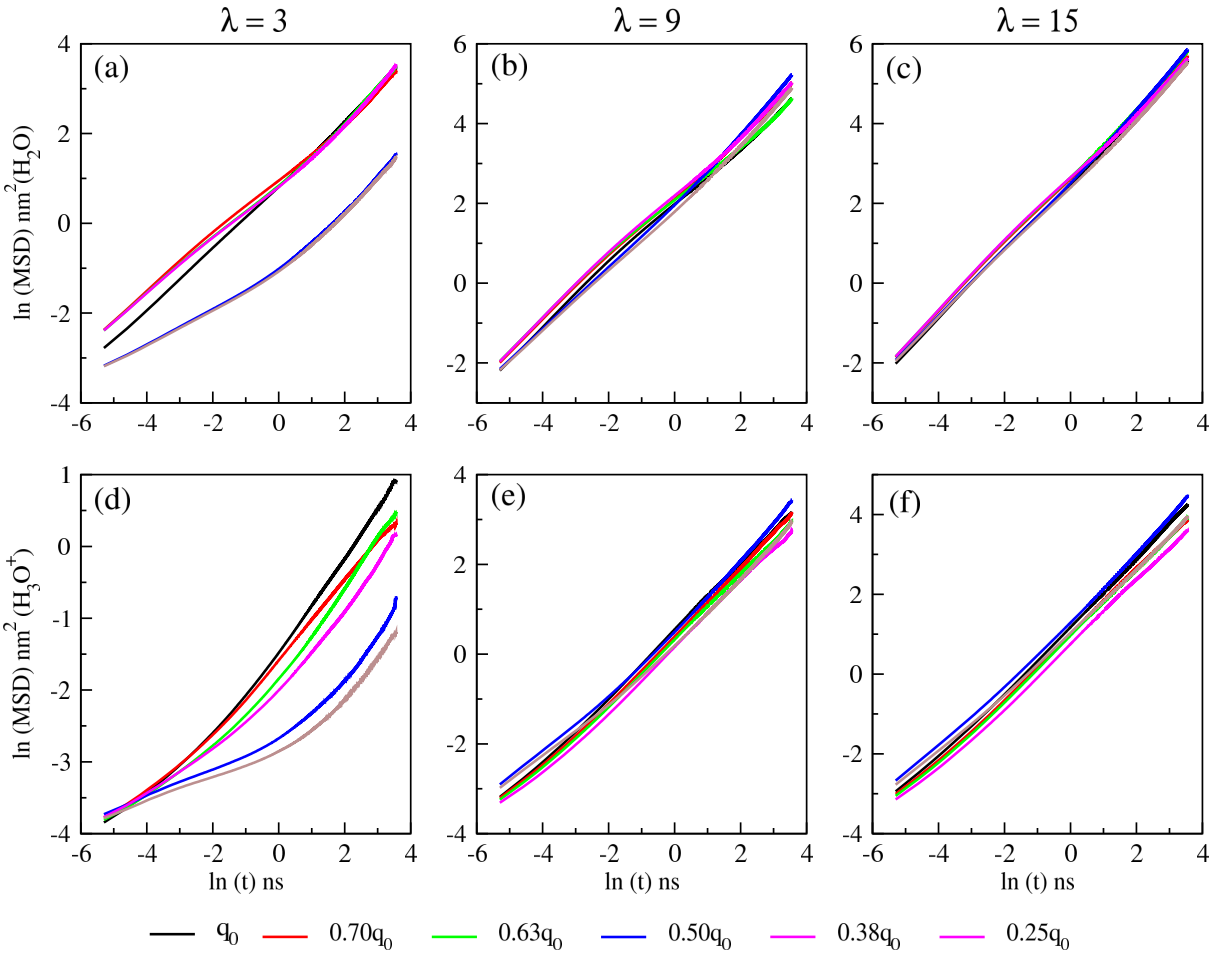

Figure 2.8: Time dependence of the MSDs of water molecules (a, b, c) and hydronium ions (d, e, f).

Figure 2.9 shows the diffusion coefficients of (a) water and (b) hydronium. At λ = 15 (q_0) the calculated self-diffusion coefficient of water molecules and hydronium ions is 1.34 $\times$ 10^{-5} cm^2/s and 0.39 $\times$ 10^{-5} cm^2/s respectively. These values are in good agreement with the work of Devanathan et al.[37] (1.37 $\times$ 10^{-5} cm^2/s (water) and 0.22 $\times$ 10^{-5} cm^2/s (hydronium ions)) and Jang et al.[35] (1.43 $\times$ 10^{-5}cm^2/s (water) and 0.29 x 10^{-5}cm^2/s (hydronium ions)). The increase in charge delocalization leads to reduced electrostatic interactions between the sulfonate group and water molecules and is expected to show increased diffusion coefficient of water molecules. The water diffusion

increases (see Figure 2.9) initially with charge delocalization (on reducing the charge on sulfonate group from q_0 to $0.50q_0$) and decreases further with excessive charge delocalization ($0.63q_0$ to $0.25q_0$). A comparison of diffusion coefficeints of hydronium ions (from

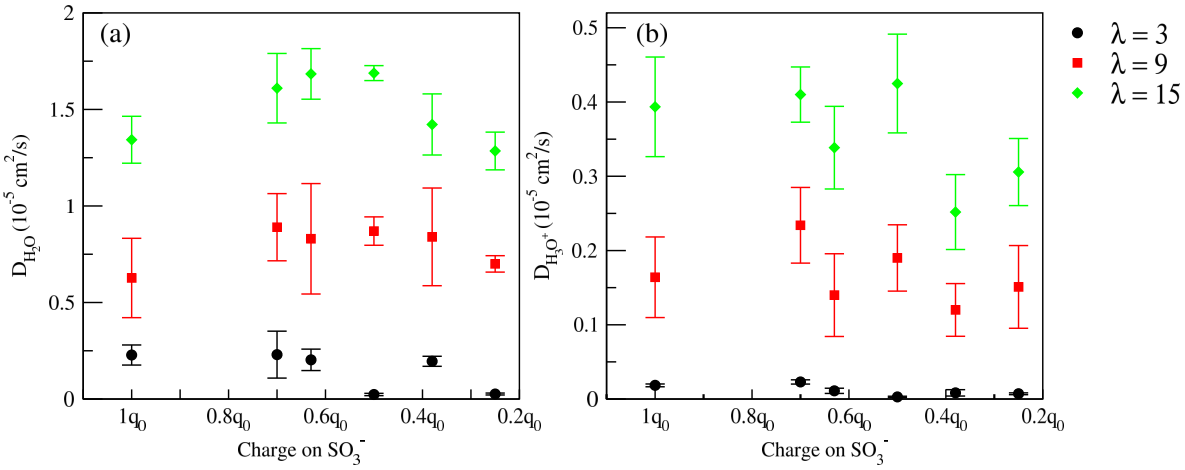

Figure 2.9: The diffusion coefficients of (a) water molecules and (b) hydronium ions vs. charge (q) on the sulfonate group at $\lambda = 3$, $\lambda = 9$ and $\lambda = 15$.

this work) with experiments and previous simulations in shown in Figure 2.10. As observed, the vehicular diffusion coefficients from this work are in qualitative agreement with trends observed from experimental, ab initio MD, MS-EVB studies and are in excellent agreement with previously reported from classical MD simulations. Earlier studies on Nafion,[36] SPEEK,[147] and PFIA[148] membranes have shown that water diffusion increases with increasing water cluster sizes. In contrast, in this work the diffusion coefficients of water molecules increases at $\lambda = 15$ from 1.34×10^{-5}cm^2/s (q_0) to 1.68×10^{-5}cm^2/s ($0.50q_0$), though a four-fold decrease in average water cluster sizes (see Figure 2.7) is observed. Similar trends are observed at $\lambda = 9$, with insignificant changes seen at $\lambda = 3$. This effect could be explained in the following manner. For charge delocalization from q_0 to $0.50q_0$ water molecules experience less electrostatic attraction from the sulfonate groups which results in a higher diffusivity though there is a decrease in water cluster sizes. However, when charge delocalization is relatively higher ($0.38q_0$ and $0.25q_0$), the water cluster

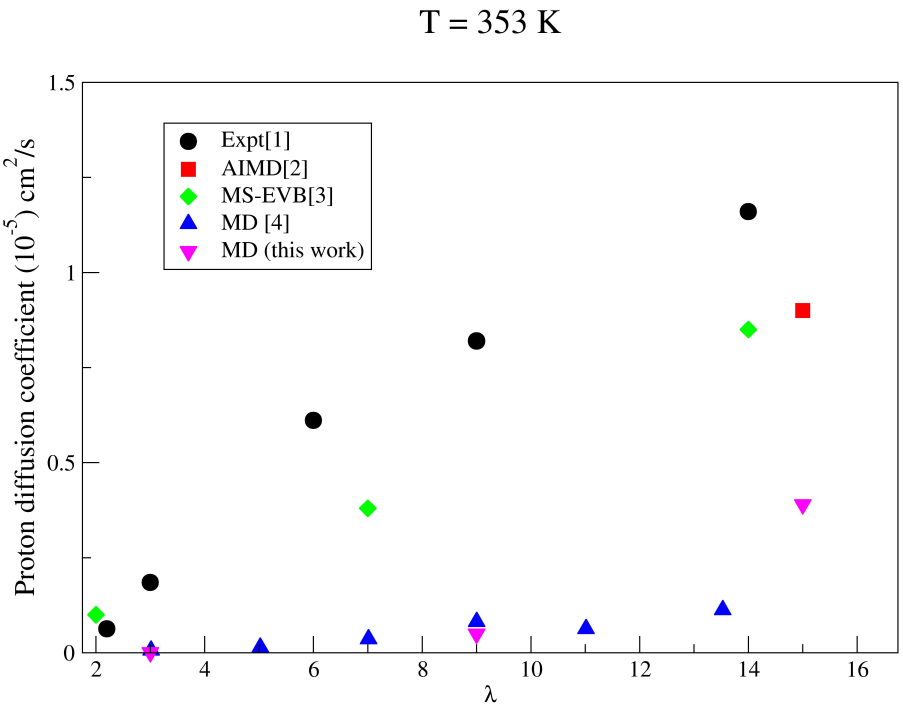

Figure 2.10: The diffusion coefficients of (a) water molecules and (b) hydronium ions vs. charge (q) on the sulfonate group at $\lambda = 3$, $\lambda = 9$ and $\lambda = 15$.

size decreases significantly and negate the effects due to the smaller electrostatic attraction between the sulfonate groups and water molecules thus reducing diffusivity. It is also possible that the water molecules are trapped along the side chains at higher charge delocalization, due to the larger negative charge being distributed on the pendant side chain atoms, which leads to reduced diffusivity of water molecules. This trapping effect can be elucidated by stronger interactions between water molecules and pendant side chain oxygen atoms, at very high charge delocalization as compared to those at lower charge delocalization as suggested by the RDFs (Figure 2.5).

Chapter 3

Computational Investigation of a Protic Ionic Liquid doped Poly-benzimidazole: Fuel Cell Electrolyte

3.1 Introduction

In this chapter, ion transport in N, N- diethyl-N-methylammonium triflate ([dema][TfO]) doped PBI membrane is modeled using MD simulations. Noto et al.[149] proposed proton transport occur via cation clusters in triethylamine saturated and triethylammonium-triflate IL doped Nafion. Liu et al.[150] observed high conductivity in a trimethylammonium phosphate IL doped nano-filtration membrane. Mogurampelly and Ganesan[151] observed using MD simulations increased mobility of ions with increasing [BMIM][PF_6] IL wt% in poly(ethylene oxide) polymer electrolytes containing a $LiPF_6$ salt. Blanchard et al.[152] investigated a family of neat trimethylamine ILs using the PFGSE-NMR spectroscopy and concluded the absence of proton hopping (structural diffusion).

A commonly investigated protic IL is the [dema][TfO]. Nakamoto and Watanabe[153] observed proton activity of [dema][TfO] to be higher than phosphoric acid. The authors investigated around 80 different protic ILs. The authors proposed [dema][TfO] is a promising electrolyte due to following reasons: facile electrode reactions (hydrogen oxidation, oxygen reduction at Pt electrode), open circuit voltage (OCV) of 1.03 V at 150

°C which is close to the theoretical OCV, wide liquid range, and high ionic conductivity. The authors also found that the proton activity of [dema][TfO] to be higher than that of phosphoric acid. Sunda[102]employed MD simulations and concluded that diffusion of ions increases with increasing [dema][TfO] IL wt% when doped with Nafion. Lee et al.[154] observed that conductivity at 80 IL wt% of [dema][TfO] doped sulfonated polyimides to be comparable to hydrated Nafion. Liu et al.[155] observed better stability and high ionic conductivity in [dema][TfO] IL doped PBI. The authors observed that activation energy of ionic conductivity decreased with IL wt% due to free ionic mobility. Using the conditions described in the experimental work of Liu et al.,[155] we employ MD simulations to calculate structure and dynamics in varying [dema][TfO] IL wt% doped with PBI with effect of temperature. The simulations will unravel various interactions in [dema][TfO] IL doped PBI which is not reported from the experimental study. Further, the simulations will provide insights on the diffusion of cations and anions separately and comparison of ionic conductivity with experimental study. The computational details to create configurations which represent the experimental choice of IL wt% are discussed in section 3.2. Section 3.3 discusses the elucidation of ion-ion, ion-PBI interactions, ionic diffusion, and conductivity in varying [dema][TfO] IL doped PBI environments. A summary of key findings concludes this chapter.

3.2 Computational details

The chemical structure of PBI and [dema][TfO] ion pair is shown in Figure 3.1. The force-field parameters for PBI were taken from the OPLS-AA force-field database.[156] Earlier reports on neat ILs have shown that unit charge on the cations and anions leads to underestimated diffusion coefficients.[157–159] To alleviate this, scaled partial charges were proposed/implemented by Maginn and coworkers,[160] Sprenger et al.[97] and Nasrabadi and

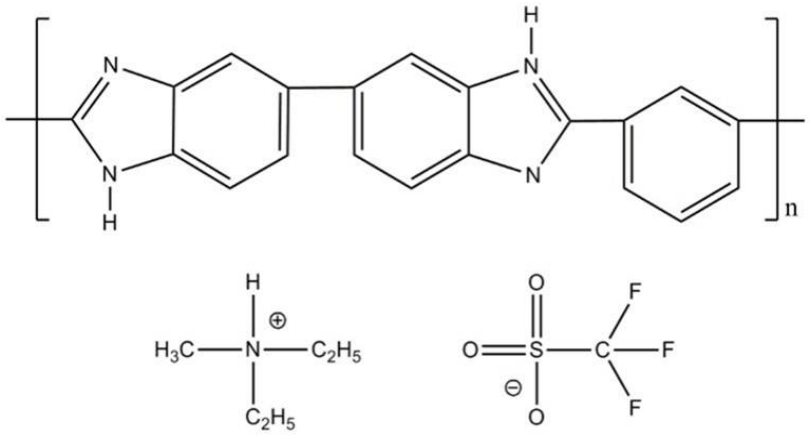

Figure 3.1: The chemical structure of (a) PBI, (b) [dema] cation, and (c) [TfO] anion.

Gelb.[103] In this work, the force field parameters for [dema][TfO] were extracted from the work of Nasrabadi and Gelb,[103] which were originally developed by Lopes et al.[161] The system sizes which represent the compositions of [dema][TfO] doped PBI are shown in Table A3 (Appendix A).

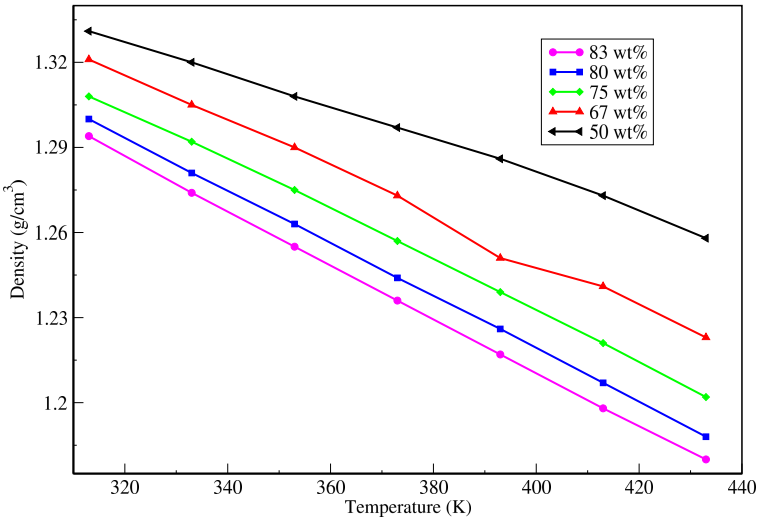

Figure 3.2: Density of [dema][TfO] doped PBI vs. temperature.

The simulation protocol for input generation, equilibration, and production run of varying composition of [dema][TfO] IL doped PBI at different temperatures are shown

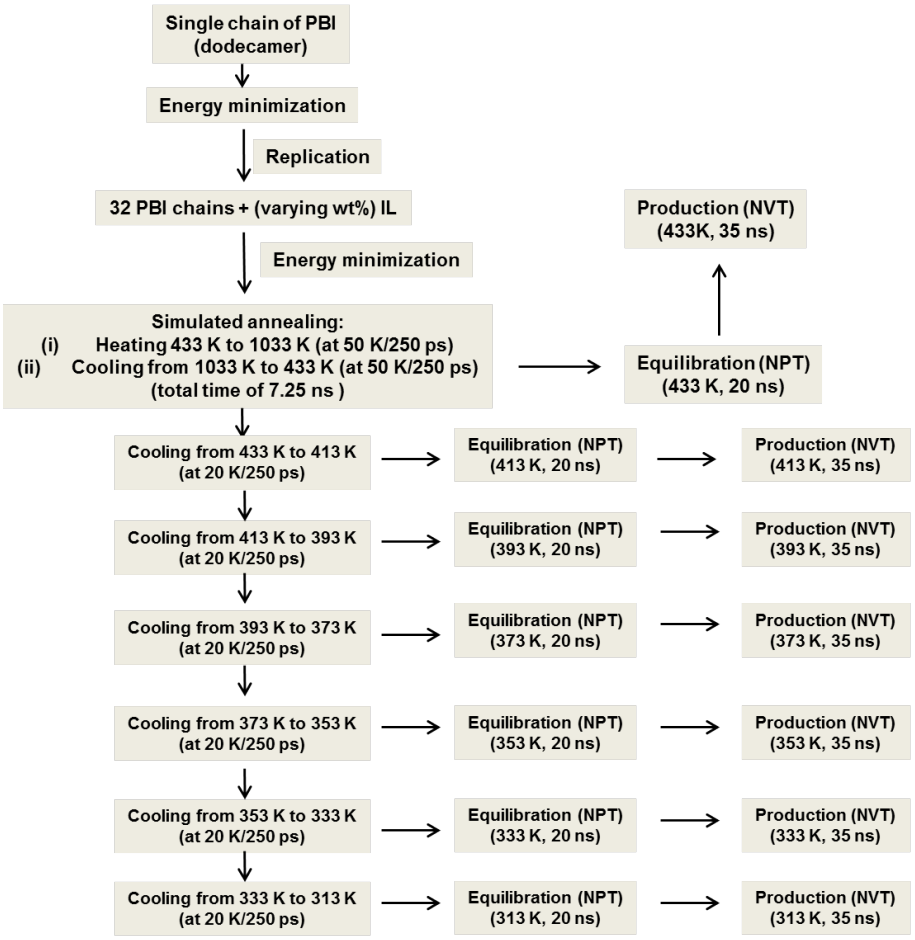

Figure 3.3: Simulation protocol for input generation, equilibration and production run of varying compositions of [dema][TfO] doped PBI at various temperature. The steepest descent algorithm was employed for energy minimization. The timestep to integrate equations of motion was 1 fs, and the leapfrog algorithm[123] was used as an integrator for the equations of motion. The cut-off for the non-bonded interactions was 1.2 nm. The PME[137] method was used to calculate the long-range electrostatic interactions. Each system was equilibrated for 20 ns in the NPT ensemble with an isotropic pressure of 1 bar using Berendsen barostat. The temperature was kept constant using a velocity-rescale thermostat[162] with a coupling time of 0.1 ps. The equilibration for all IL doped systems was followed by a production run in the NVT ensemble using the Nosé–Hoover thermostat.[138]

in Figure 3.3. The densities from equilibration are shown in Figure 3.2. The simulated density for PBI at 300 K (1.29 g/cm^3) is in good agreement with the experimental results (1.2 - 1.34 g/cm^3).[163,164] The simulated density for neat IL (1.27 g/cm^3 at 303 K) agrees

with the value of the experimental report by Yasuda et al.[165]

The snapshots of configurations (extracted from the trajectory of the production run) show (Figure 3.4) ionic clusters at 50 IL wt% and interconnected ionic channels at 83 wt%. The trajectories from the production runs (recorded every 5 ps) are used for calculation of RDF[123] and diffusion coefficients (ionic conductivity), as discussed in the next section. All RDFs discussed here are from MD simulations at T = 433 K.

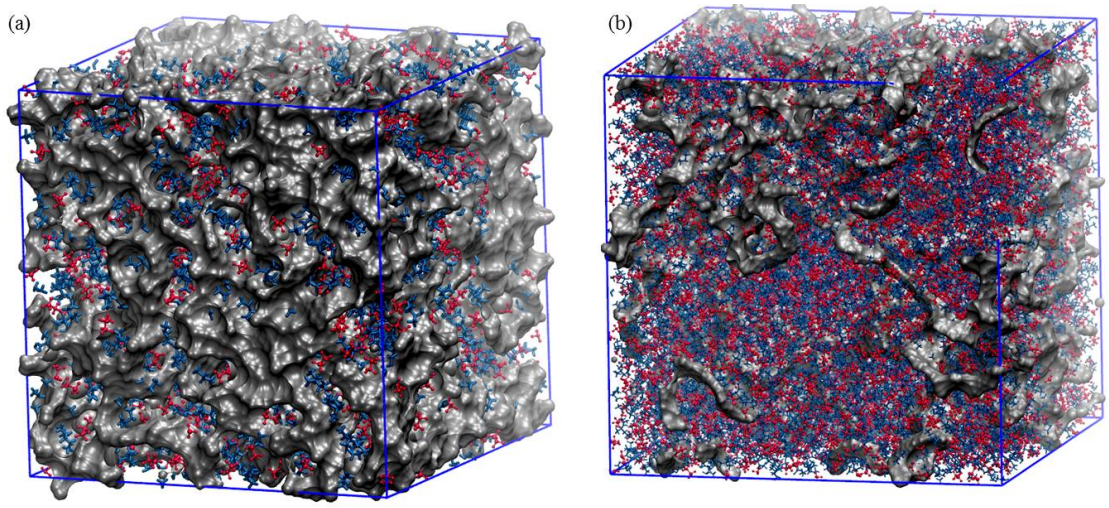

Figure 3.4: The snapshots of configurations obtained from the production run at T = 433 K at (a) 50 wt%, and (b) 83 wt% of [dema][TfO] IL. Grey color (surf representation) represents membrane, blue color (line representation) represents cation, and red color (CPK representation) represents anion using line representation of VMD.

3.3 Results and discussion

3.3.1 Structure

The RDFs can be categorized as ion-ion and ion-PBI interactions. The ion-ion interactions are described by cation-cation and anion-anion RDFs (see Figure 3.5 a,b). Except at 50 wt%, the cation-cation interactions (see Figure 3.5 a) show a primary peak at ∽7 Å and a

minimum at ∽9 Å, a broad and reduced intensity of the secondary solvation shell between 9 Å to 12 Å. In contrast, at 50 IL wt%, the cation-cation interactions appear with a primary peak at 7.2 Å, with a significantly reduced intensity and a minimum at 8.5 Å. However, the secondary solvation shell shows more distinct features with a broad peak at 9.4 Å and a minimum at 12.3 Å. The anion-anion interactions (see Figure 3.5 b) show the following features: Except at 50 IL wt%, a broad primary solvation shell appears with a peak at ∽7.5 Å, with a minimum at ∽10 Å. However, at 50 IL wt% (similar to cation-cation RDFs), the interactions have a reduced intensity compared to other IL wt%. Also, the RDFs shows a sharp primary peak at a relatively shorter distance (6.5 Å) and a first minimum at 8.1 Å. The sharp structural features of cation-cation and anion-anion RDFs at 50 IL wt% support the existence of disconnected ionic clusters (see Figure 3.4).

The ion-PBI interactions are characterized by choice of interaction sites on the cations/ anions and PBI, as seen from the RDFs (see Figure3.5 c,d,e,f). The cation-PBI RDFs calculated between the acidic proton of the cation (HD) and the free nitrogen atoms (N1 and N2) of the imidazole ring of PBI (see Figure 3.5 (c,d)). At all IL wt%, the HD-N1 (see Figure 3.5 c) and HD-N2 RDFs (see Figure 3.5 b) show a primary peak at ∽2.2 Å with a minimum at ∽3.0 Å. A higher intensity secondary peak at ∽5.4 Å and minimum at ∽7 Å is also observed. The smaller intensity of primary peak of cation-PBI RDFs suggests that the cations do not prefer to interact with the PBI at shorter distances. The anion-PBI RDFs were calculated between the oxygen atoms of the anion and the acidic protons (H1, H2) of PBI. A sharp peak at ∽1.9 Å (see Figure 3.5 e), and ∽1.7 Å (see Figure 3.5 f) is observed from the O-H1 and O-H2 RDFs, respectively. Both RDFs show a minimum at ∽2.7 Å and illustrate strong hydrogen bonding interaction between the oxygen atoms of anion and PBI. The RDFs show the interaction of oxygen atoms with the H2 atom is stronger compared to interactions with the H1 atom. Similar trends are seen in RDFs at other temperatures (see Figure B1 - B3 of Appendix B).

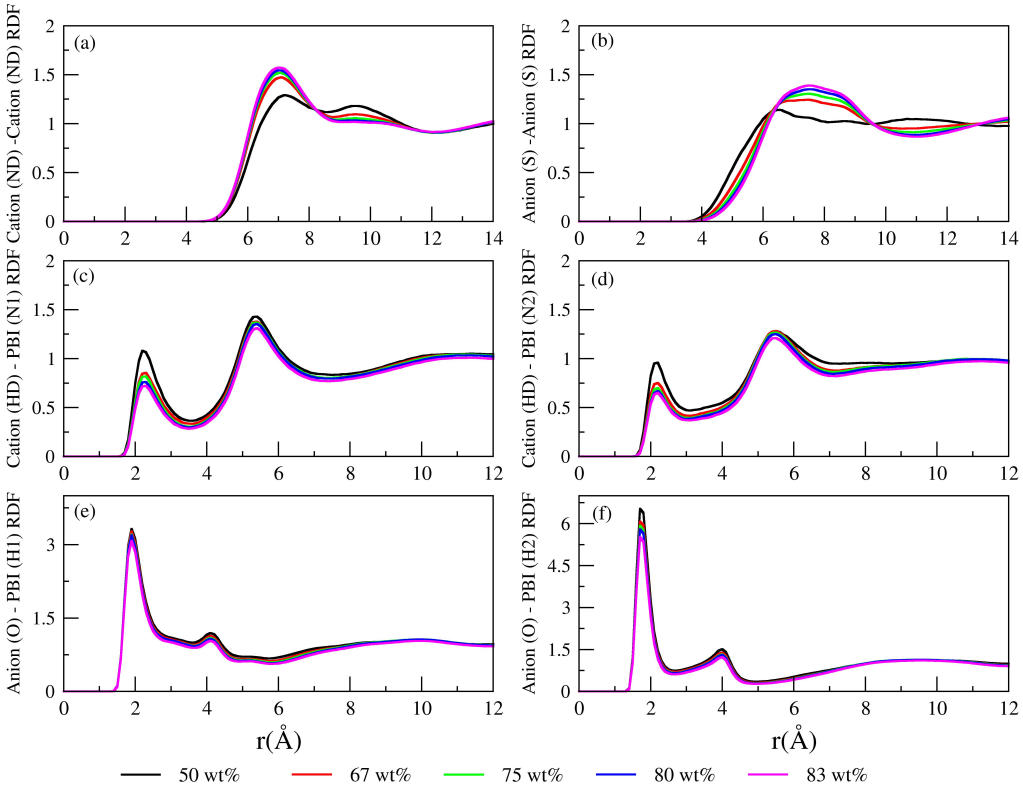

Figure 3.5: PBI has two free N atoms (labelled as N1 and N2) and two acidic protons (protons attached to N, labelled as H1 and H2, see Figure 3.1). N atoms of PBI can interact with an acidic proton of cation, (HD) and the acidic protons of PBI (H1 and H2) can interact with F and O atoms of the anion. The RDF for (a) cation (ND atom)-cation (ND atom) and (b) anion (S atom)- anion (S atom) (c) cation (HD atom) – PBI (N1 atom), (d) cation (HD atom) – PBI (N2 atom) RDF (e) anion (O) – PBI (H1) RDF and (f) anion (O) – PBI (H2) RDF at T = 433 K.

3.3.2 Dynamics

The mobility of cations and anions is characterized by MSD. The MSDs (see Figure 3.6) at lower IL wt% and temperature (e.g. 50 wt% and T = 313 K - 433 K; at 67 wt%, T = 313 K - 353 K, at 75 wt%, T = 313 K - 333 K etc.) show sub-diffusive behavior of cations and anions.

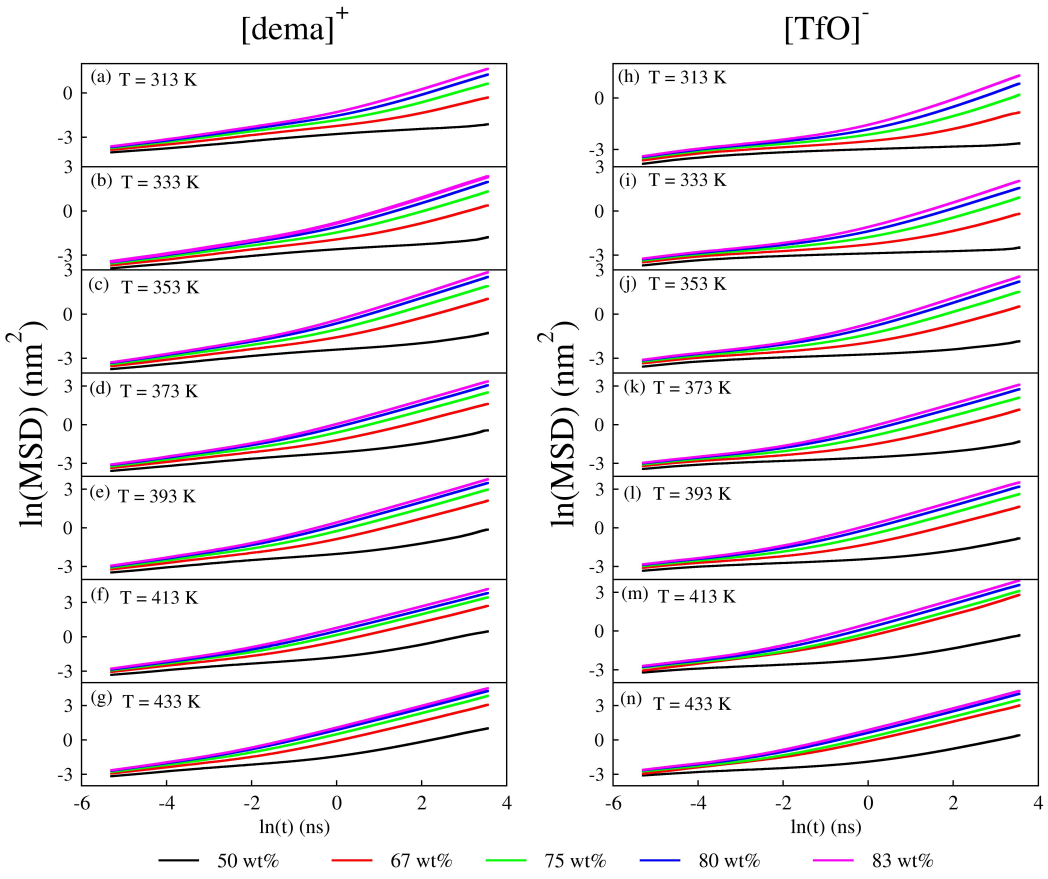

Figure 3.6: MSDs of cations and anions, at different IL wt% and temperature

At other wt% and temperature, linear diffusion of cations and anions are observed. The diffusion coefficients (see Figure 3.7 (a, b)) of cations and anions were calculated from the linear regime (obtained from the production run of simulations) of the MSD (see Figure 3.6) using Einstein equation.[123] The effect of IL wt% on diffusion coefficients shows larger increase (between 67 IL wt% and 83 IL wt%) at lower temperatures. E.g., at T = 433 K, the diffusion coefficeint increases by a factor of ∼3 for cations and anions. However, at T = 373 K, the diffusion coefficient increases by a factor of ∼5 for cations and ∼7 for anions respectively. The effect of temperature (T = 373 K to T = 433 K) on

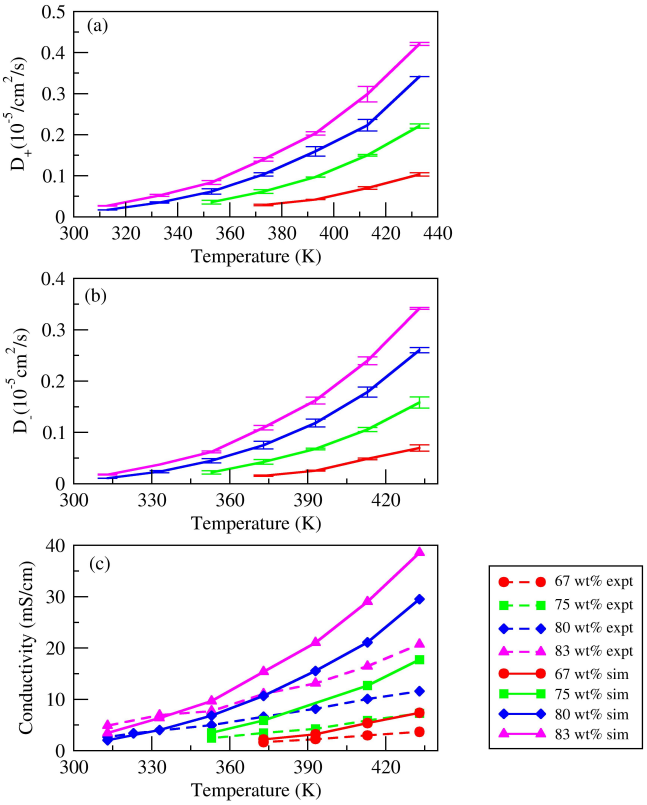

Figure 3.7: Temperature-dependent diffusion coefficients of (a) cation and (b) anion (c) Ionic conductivity. Experimental conductivities are from the work of Liu et al.[155]

the diffusion coefficient for cations/anions increase by a factor of ∼3. However, at 67 IL wt%, The diffusion coefficients of cation increases by a factor of ∼3.5 and anions by ∼4.4 respectively.

The ionic conductivity was calculated using the Nernst-Einstein equation[123] which is written as:

$$\frac{N_A e^2}{V_{mol}\ k_B T}(D_+ + D_-) \tag{3.1}$$

where, N_A is Avogadro number, $V_{mol} = \frac{mol.wt}{Density}$, D_+ and D_- are the diffusion coefficients of the cations and anions, N is the number of ion pairs, T is the temperature, e is the charge

of an electron and k_B is the Boltzmann constant. The simulated ionic conductivities are in qualitative agreement (see Figure 3.7 c) with the experimental ionic conductivities. At T$\leq$ 373 K, the simulated ionic conductivities are higher by a factor of 1.4 - 1.7 compared to experimental ionic conductivities. At T = 433 K, the simulated ionic conductivities are higher by a factor of 1.8 - 2.5 compared to experimental conductivities. The higher ionic conductivity with increasing IL wt% supports the presence of well developed interconnected ionic channels (see Figure 3.4) and supports experimental results.[155,166]

Chapter 4

Quantum Mechanical Investigation of Proton Transport in Imidazolium Methanesulfonate Ionic liquid

4.1 Introduction

In this chapter, proton transport pathways in imidazolium methanesulfonate (IMMSA) IL were examined using quantum chemistry calculations. In IMMSA PIL, the constituting acid (MSA) and base (IM) interact to form hydrogen bond(s), where the proton from the acid partially or totally dissociates and transfers to the base forming anion (MS^-) and cation (IMH^+). This phenomenon depends on the strength of the acid and base and can be determined by their aqueous ΔpK_a values [167,168] for an acid, A, and base, B, reacting to form cation BH^+ and anion A^-, ΔpK_a is defined as the difference between the pK_a values of BH^+(aq) and A(aq). Davidowski et al.,[169] using NMR spectroscopy and electronic structure calculations on diethylmethylamine (DEMA) based PILs with different anions, argued that a more accurate prediction of proton transfer (PT) from acid to base in the PIL can be achieved by examination of gas phase proton affinity (PA) of the acid/anion. Hunt et al.[170] reviewed hydrogen bonds present in a range of PILs. These hydrogen bonds are (a) protic hydrogen bonds, formed through mobile hydrogen between electronegative atoms of proton donating and accepting species, and (b) aprotic hydrogen bonds, formed between the hydrogen atoms in alkylic groups of a molecule and electronegative atoms,

such as N and O, of another molecule.

Lee et al.[154] showed that proton conduction in PIL-doped membranes occurs mainly due to proton exchange between cation and free base. The experimental studies on the effect of acidity on proton transport, using ^{1}H and ^{15}N NMR spectroscopy, have shown that proton diffuses mainly with the anion if the acid in PIL is weak, while for strong acid it diffuses with the cation. Nakamoto et al.[9] synthesized a novel ionic liquid, benzimidazole-bis-(trifluoromethane-sulfonyl)imide, and characterized its transport properties at varying concentration of base using ^{1}H NMR chemical shifts and Raman spectroscopy. The authors observed that increasing base concentration leads to faster proton transport due to higher Grotthuss diffusion, where proton hops between the cation and base. Thus, proton transport in a PIL can occur either via vehicular diffusion or via a combination of Grotthuss and vehicular diffusions.

Of various bases, IM, due to its amphoteric nature, has been widely studied in pure form or as a constituent of PIL for its use as an electrolyte and as a dopant in the membrane (or IM derivatives attached to membrane backbone) for high-temperature fuel cells.[5] IM has a high boiling point (256 °C) with pK_a values: 6.99 for imidazolium (IMH^+) and 14.44 for IM.[171] Proton conduction in liquid IM occurs through vehicular motion of IMH^+ and IM ions, generated through its self-dissociation,[5,172,173] and Grotthuss diffusion of a proton from IMH^+ ion to IM molecule.[174,175] After each step of proton diffusion, rotation of IM molecules is necessary for the subsequent PT. The rotation causes breaking and regeneration of hydrogen bonds with the surrounding IM molecules by overcoming the energy barrier equivalent to a number of bonds breaking in the process, and, thus it controls the rate of proton transport.[5] Kumar and Venkatnathan[176] reported energy barrier of IM rotation for two, three, and four IM molecules as 8.0,17.1, and 20.0 kcal/mol, and showed them to be equivalent to the number of hydrogen bonds broken during the rotation of the IM ring.

Experimental results show evidence of similar phenomenon of ring rotation in proton conduction in crystals and PILs containing IM as one of the constituents. Goward and coworkers,[177] using solid state NMR, did an extensive study of proton transport in IM-based proton conductors. Their results show IMH^+ ion ring rotation along the C_2-axis in solid IMMSA with a barrier of 38 $\pm$ 5 kJ/mol. This barrier increases to 128 kJ/mol, depending on the chemical properties of the acidic constituent. The authors attributed this large barrier to strong electrostatic interactions between IMH^+ ions and the coordinating anions. Conrad and co-workers[178] measured ionic conductivity of IMMSA and reported energy barriers of 36.3 $\pm$ 3.2 kJ/mol in solid phase and 20.3 $\pm$ 0.13 kJ/mol in the melt, respectively. A lower activation energy barrier of 21.4 $\pm$ 4 kJ/mol in solid imidazolium oxalate was also reported, attributed to breaking of relatively weaker bonds, i.e., hydrogen bonds, during ring rotation.[179] Traer and Goward[180] examined dynamics of proton transport in solid imidazolium methylphosphonate (IMMPA) and observed the slower rotation of IM ring, compared to IMMSA. The authors concluded that rotation of both methylphosphonate and IMH^+ ions contribute to ionic conductivity.

While phosphates are good proton conductors, at higher temperatures they condense into pyrophosphates resulting in a decrease of proton conductivity irreversibly.[181] However, sulfonate functional group is chemically stable and is part of side chains of PFSA membranes, such as Nafion, which facilitates proton conduction. MSA, a prototype of these membranes, is a strong nonhalogenated acid and bears low toxicity and high biodegradability, which makes it an ecofriendly electrolyte.[182] Almeida and Goward[183] investigated proton dynamics in sulfonic acid based pristine salts, such as benzimidazolium methanesulfonate (BMSA), IMMSA, and imidazolium trifluoromethanesulfate (IFMS), and in salt-polymer composites. The authors proposed that proton conduction in BMSA salt occurs via rotation of the anions only; in IFMS salt via rotation of cations only; and in IMMSA salt via rotation of both cations and anions. Proton conduction phenomena

was attributed to the available space for rotation of constituents of an IL: in BMSA, larger size of benzimidazolium ion restricts its rotation, whereas anion has ample space to freely rotate; in IFMS, rotation of anion is inhibited due to steric hindrance between CF_3 groups; and in IMMSA, both anion and cation have enough space for their unrestrained rotation.

IMMSA offers several advantages such as high electrochemical window of 2.0 V, good thermal stability, favorable plastic crystal behavior, and easy synthesis making it a potential candidate for high-temperature PEMFCs.[178] In pure IM, hydrogen bonding interactions occur among IM molecules and IMH^+ and IM ions. Thus, in IMMSA, an MSA molecule will interact with these chemical species of IM and another MSA molecule. In this chapter, static electronic structure calculations were employed to investigate various possible routes for PT in IMMSA, in the presence of increasing IM molecules. Although these static calculations do not consider dynamic structural changes, they still offer excellent insights to understand interactions among molecular constituents and the energetics associated with proton transport pathways.[44,184–186] The computational details are presented in section 4.2. The structure and energy barriers involved in PT in IMMSA and with varying IM molecules are presented in section 4.3.

4.2 Computational details

All quantum calculations were performed using Gaussian 09 suite of programs.[187] Hybrid DFT with Becke's three-parameter functional B3LYP[109,114–116] with 6-311++G** basis set was used. All systems explored in the study were optimized, followed by frequency calculations to ensure minimum energy geometry. The barriers at each PT step, structural and rotational, was examined through transition state (TS) structure, which was obtained by employing Berny algorithm using GEDIIS,[188] and were confirmed by the presence of one imaginary frequency. A restricted, if otherwise not mentioned, potential energy

surface (PES) scan, followed by optimization, was performed on a structure by moving the hydrogen atom to examine PT between participating atoms or by rotating a molecule to investigate reorganization. The intrinsic reaction coordinate calculations were performed on the TS structure to confirm its connectivity with initial and final structures.

The stability of various possible geometries of a complex was examined by calculating electronic energy along with zero point energy (ZPE) corrections. A PES scan is usually followed by a TS search, and the calculation of barriers through TS calculations are reported with and without ZPE corrections. All ZPE corrected energy barriers are reported in parentheses. The gas phase PA of a substrate (B) was calculated as negative of heat of reaction (ΔH) for proton addition. For example, if proton addition reaction is

$$B + H^+ \rightarrow BH \tag{4.1}$$

then PA of B = -(ΔH). The value of ΔH = -$\Delta E_{elec} - \Delta$ZPE + $\frac{5}{2}$RT, where $\Delta(E_{elec} +$ ZPE) is $(E_{elec}$ + ZPE$)_{BH}$ - $(E_{elec}$ + ZPE$)_B$, and $\frac{5}{2}$RT includes translational energy $\frac{3}{2}$RT and PV term (= RT) of the proton. The interaction energy of a complex is calculated as the energy difference between complex and the sum of isolated species, i.e., E_{int} = $E_{complex}$ - ΣE_i, where $E_{complex}$ is the energy of the complex, and E_i = electronic energy + ZPE of species i. The PA of a complex depends on which atom in the complex the proton interacts, and accordingly, PA is referred with respect to that particular atom. The reverse of the above reaction is the deprotonation, and the corresponding deprotonation energy has the same magnitude as PA.

4.3 Results and discussion

The chemical structures of MSA, MS^- ion, IM, IMH^+ ion, IM^- ion, and IMMSA are shown in Figure 4.1 (along with interatomic distances of interest). The possible inter-

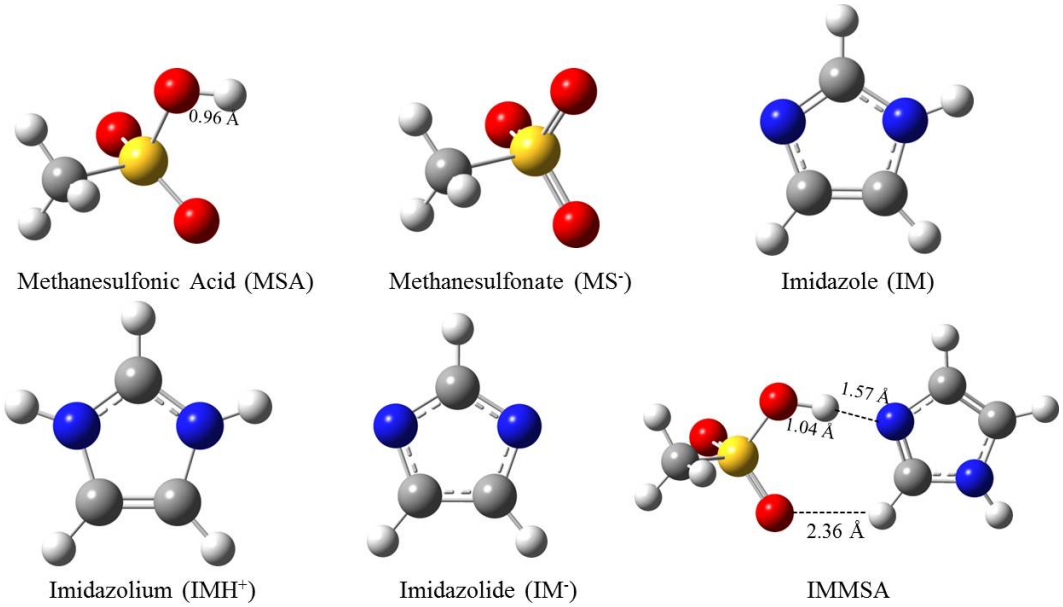

Figure 4.1: Chemical structures of MSA, MS^- ion, IM, IMH^+ ion, IM^- ion, and IMMSA. Color code: dark blue, dark gray, light gray, red, and yellow spheres represent N, C, H, O, and S atoms, respectively.

actions among these species in IM rich IMMSA leading to proton conduction can be categorized as (i) between MSA and IM, (ii) between IMH^+ and IM, (iii) between IM^- ion and IM, (iv) between MSA and IM^-, and (v) between MSA and MS^- ion. Apart from these, other interactions are also possible and are discussed in the latter part of the chapter. These interactions arise from hydrogen bonds, such as O-H···N, O···H-N, and O···H-C, forming among neutral molecules and charged species, and electrostatic interactions between charged species. The strength of hydrogen bonds depends on interatomic distances and angle between interacting atoms, whereas the strength of electrostatic interactions depends on the size of the charged species and distance between them.

4.3.1 PA vs ΔpK_a

Proton conduction depends on the concentration of charged species and their mobility in the surrounding medium. In IL or in base rich IL, charged species are generated either

due to PT from an acidic constituent to the basic molecule or complex or due to autoprotonation. The transfer of a proton from one component and its acceptance by another are widely determined by experimentally measuring ΔpK_a value in the aqueous phase.[168] An approximate value of ΔpK_a of any IL can be estimated using quantum chemistry calculations. An alternate, and well-accepted method,[169] is via calculation of ΔPA (ΔPA = PA of anion − PA of base). A comparison of calculated vs experimental PA is shown in Table A1 of Appendix A. To understand relationship between ΔpK_a, ΔPA, and location of the exchangeable proton, calculations were performed to estimate ΔPA value of a series of ILs consisting of IM as a common base and are presented in Table A1.

The results in Table A1 show that proton does not move from acid to base in IM···CH_3SO_3H (pK_a of CH_3SO_3H = 1.92),[178] IM···CF_3COOH (pK_a of CF_3COOH = 0.23),[189] and IM···CH_3COOH (pK_a of CH_3COOH = 4.76).[190] ILs due to low acidity of the acidic components. In these ILs, the concentration of charged species due to self-dissociation will be lower. CF_3SO_3H (pK_a = 14.7)[191] and HTFSI (pK_a = 10)[192] (bis(trifluoromethanesulfonyl)imide) are relatively stronger acids. Hence in these ILs, IM-CF_3SO_3H and IMH-TFSI, the proton moves to the base and generates charged species. In terms of ΔPA values, ΔPA < 90 kcal/mol will lead to PT from acid to base. This has been further confirmed by calculation of ΔPA for another set of ILs containing DEMA (pK_a = 10.5)[192] as a common base. The results are shown in Table A2 of the Appendix A. To examine the effect of dispersion, PA calculations with B3LYP-D3 functional, using the Gaussian 09 revision D.01[193] software, were performed. These calculations show that the effect of dispersion on PA and ΔPA is insignificant (see Table 4.1 below and TableA1 and TableA2 of the Appendix A).

In an IM rich IL, an extra IM molecule interacts, via hydrogen bonding, with surrounding base or acid molecules, or with ions. This interaction leads to change in acidity and basicity of the system. Table 4.2 shows the effect of extra IM molecules on PA of IM

Table 4.1: Chemical formula of each ion pair, ΔpK_a = (pK_a(base) - pK_a(acid)) values of the IL, calculated using experimental aqueous pK_a values of base and acid, calculated gas phase ΔPA = (PA of anion - PA of base), and final position of the proton in each ion pair (ΔPA values in parentheses are calculated using B3LYP-D3 functional).

System	ΔpK_a	ΔPA (kcal/mol)	Final position of proton
IM-HTFSI	24.44	68.32 (68.86)	Proton transfers to IM
IM-CF_3SO_3H	29.14	73.23 (73.33)	Proton transfers to IM
IM-CH_3SO_3H	16.36	93.44 (93.43)	Proton remains with CH_3SO_3H
IM-CF_3COOH	14.21	93.81 (93.68)	Proton remains with CF_3COOH
IM-CH_3COOH	9.68	119.29 (119.48)	Proton remains with CH_3COOH

and IM ion. The left half of the table illustrates the effect on PA of imidazole chain with increasing IM molecule, and the right half is for the corresponding anion of the chain. An increase in IM molecules in an imidazole chain increases the PA of the complex. This increase is significant up to three IM molecules in the chain. Due to the negative charge on IM ion, its basicity is higher than for a neutral IM molecule. The table shows opposite trend for PA of IM ion: PA decreases up to three molecules in the chain, and addition of more molecules does not have a significant effect. This indicates that increasing length of a neutral imidazole chain increases its proton acceptance ability, and the ability trend reverses for the anionic chain. There is not much effect of IM addition on PA value of the chain, with more than three molecules. This also supports previous work[176] that in liquid

IM an extra proton is stabilized by a chain of three IM molecules and proton exists on the middle IM molecule, extra charge shared by two surrounding molecules. Table 4.2 also illustrates that autoprotonation of a longer chain will generate smaller charged complexes provided satisfying the ΔPA criterion.

The movement of a charge or charged species in the surrounding medium can be due to their motion in the bulk phase, due to structural changes in the medium or due to a combination of both. In the next part of this chapter, structural changes and energy barriers for PT in IMMSA, and in IMMSA with one and two IM molecules, were examined. The initial configurations of IMMSA and IMMSA with one/two IM molecules were chosen by fully considering the cation-anion interactions such as hydrogen bonds, electrostatic interaction, and steric factors. Proton conduction in IM based system requires rotation of all molecules in the hydrogen bonded network. Hence, rotation of molecules was considered, and the lowest activation energy pathway through calculation of TS structure is presented in this chapter.

4.3.2 Interaction and proton transport in IMMSA

[MSA]/[IM] = 1:1 composition (also referred as IMMSA) is chosen to investigate PT possibilities. As seen in Figure 4.1, proton does not transfer from MSA to IM, and this is corroborated to ΔPA > 90 kcal/mol (PA values of MS^- ion (see Figure B4 a of Appendix B) and IM are 319.55 and 226.09 kcal/mol, respectively). The O-H bond in the acid increases from 0.96 to 1.04 Å. The figure also shows that IM and MSA interact via two hydrogen bonds, shown as dotted lines in Figure 4.1, to form an adduct with an interaction energy of 15.5 kcal/mol. One hydrogen bond is O-H···N, and the other is O···H-C. As defined by Hunt et al.,[170] the former hydrogen bond is protic and the latter is aprotic.

The above results of elongation of O-H bond, non-transfer of proton from MSA, and formation of two hydrogen bonds on its interaction with an IM molecule were ob-

Table 4.2: Gas phase PA of IM and IM^- with increasing IM content.

System	PA (kcal/mol)	System	PA (kcal/mol)
IM	226.09	IM^-	349.79
$(IM)_2$	245.88	$(IM...IM^-)$	332.45
$(IM)_3$	257.49	$(IM_2...IM^-)$	321.53
$(IM)_4$	262.53	$(IM_3...IM^-)$	316.83
$(IM)_5$	265.07	$(IM_4...IM^-)$	314.49
$(IM)_6$	266.50	$(IM_5...IM^-)$	313.22

tained without inclusion of solvation effects. The calculation of gas phase ΔPA confirms/validates the final position of proton. The solvation effect can be studied by choosing an appropriate solvation model[194] that requires an a priori knowledge of dielectric constant, which is not available in the literature for IMMSA IL. Alternatively, smaller ensembles of monomers to form dimer, trimer, tetramer, etc., of IMMSA can also be generated and optimized using gas phase quantum chemistry calculations, and the results can be extrapolated to understand the behavior in bulk IMMSA IL. The quantum chemistry calculations on larger n-mers of IMMSA are computationally intensive and also complex due to many possible initial configurations. As a prototypical example, geometry optimization of an IMMSA dimer was performed, where the resultant structure is shown in

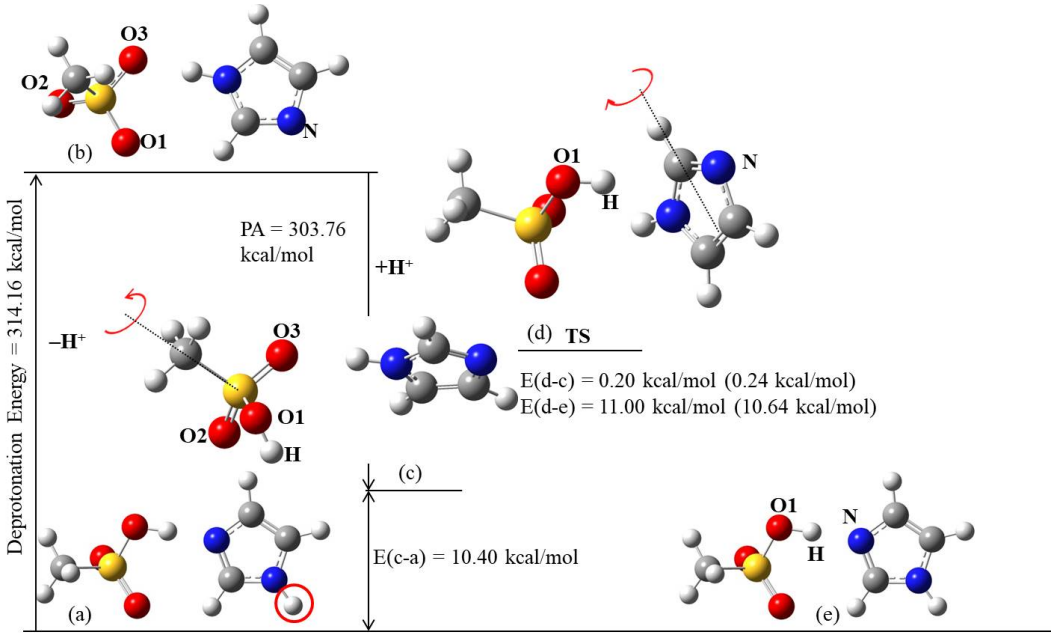

Figure 4.2: Structural changes on loss and gain of proton followed by reorganization of molecules in IMMSA. Structure (a) represents [MSA]/[IM] = 1:1, i.e., IMMSA. The optimized structure shows proton does not transfer from MSA to IM. Complex (b) was obtained when complex (a) loses the proton, marked by a circle. Structure (c) was obtained by subsequent gain of a proton by oxygen O1 in structure (b). Structure (d) is the TS structure for IM rotation where hydrogen bonding interactions between molecules break. Final structure (e) shows regeneration of hydrogen bonds. Structures (e) and (a) are the same. Energy barriers without and with ZPE corrections (in parentheses) are reported.

Figure B5 of Appendix B. Unlike the case of IMMSA monomer this structure shows PT from MSA to IM where the resultant MS^- ion and IMH^+ ion are interlinked via a hydrogen bonding network. Further an increased number of hydrogen bonds are observed in IMMSA dimer in comparison to IMMSA monomer. Similar quantum chemistry calculations (excluding solvation effects) have also been widely reported.[45,66,176,195–197]

4.3.3 Interaction of IMMSA with one IM molecule

The changes in structure and intermolecular interactions on addition of one IM molecule to IMMSA to form a [MSA]/[IM] = 1:2 composition is chosen for examination of PT. The

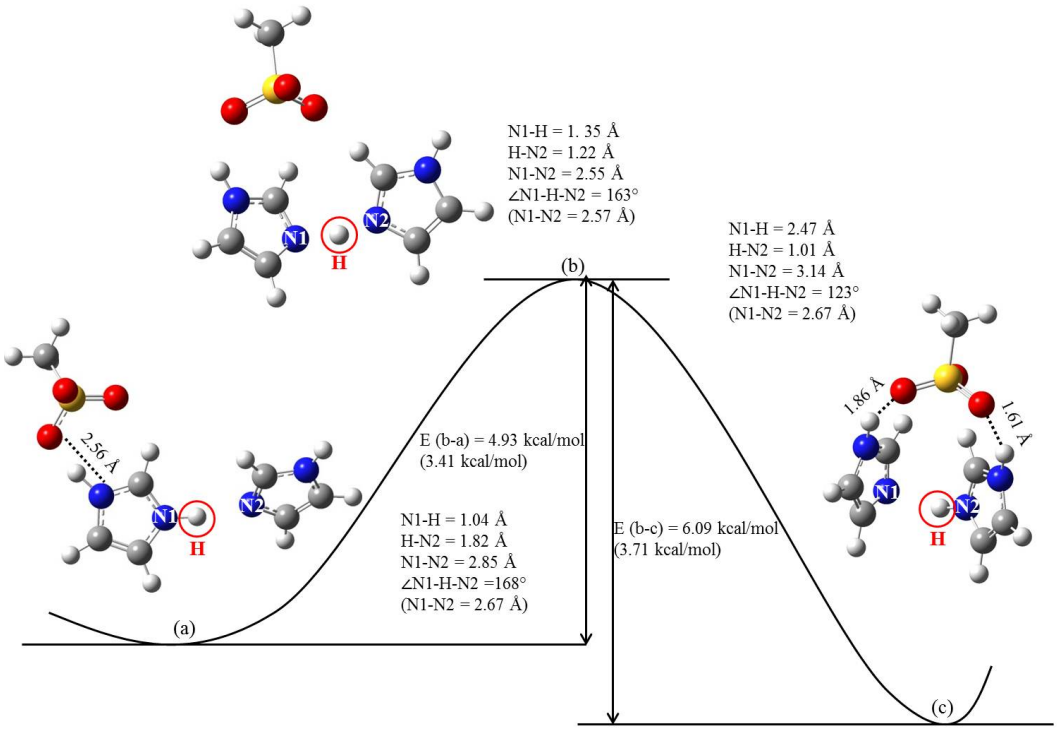

Figure 4.3: PES of proton transfer in mixture of [MSA]/[IM] = 1:2, i.e., IMMSA with one IM molecule. Structure (a) is the resultant optimized geometry of mixture forming MS···IMH···IM complex. In structure (a), N1 and N2 represent nitrogen atoms of IMH^+ ion and IM molecule, respectively, and H represents labile proton. Proton transfers from IMH^+ ion to IM molecule through TS structure (b). Structure (c) is the corresponding product where IM molecule and IMH^+ ion interact with the MS^- ion via hydrogen bonding network. Energy barriers without and with ZPE corrections (in parentheses) are reported. The atomic distances, N1-N2, in parentheses are for the corresponding IMH^+···IM system.

comparison of PA of MS^- ion and $(IM)_2$ gives ΔPA = 73.72 kcal/mol (< 90 kcal/mol), which shows that proton will transfer from MSA to IM molecule leading to formation of charged species. The optimized structure is shown in Figure 4.3a. The calculated interaction energy of the structure is 18.71 kcal/mol. This generation of charged species in this system is similar to previous studies[3,198] on $CF_3HO_2POP(CF_3)O_2H$, where it has been shown that charge separation forming ion pair occurs on addition of the water molecule that induces long-range proton hopping mechanism. Structure (b) is the TS for PT from

IMH^+ ion to IM (proton involved is circled), and structure (c) is the corresponding product. N1 and N2 represent two nitrogen atoms bonded via hydrogen atom, H. The atomic distances, N1-N2, in parentheses are for corresponding $IMH^+\cdots IM$ system. The increasing N1-N2 distance, in comparison to $IMH^+\cdots IM$, in structure (a), indicates an electrostatic interaction of MS ion with the IMH^+ ion; where these ions arise from PT from MSA to IM molecule. The PT from N1 to N2 in the complex occurs if the distance is 2.55 Å, which is almost same for $IMH^+\cdots IM$, with an energy barrier of 4.93 kcal/mol (3.41 kcal/mol with ZPE corrections). The electrostatic interaction results in higher energy barrier than for PT from IMH^+ ion to IM (ca. 0.72 kcal/mol, without ZPE corrections).[176] In TS structure (b), MS^- ion is also hydrogen bonded to a second IM molecule. On complete transfer of the proton to the second IM molecule leading to structure (c), the N1-N2 distance increases to 3.14 Å and ∠N1-H-N2 angle decreases from 163° to 123°, weakening the hydrogen bonding interaction between two IMs. However, there is an increased hydrogen bonding interaction (indicated by O-H distance = 1.61 Å) between second IM molecule and MS^- ion in structure (c), which leads to higher reverse energy barrier (6.09 kcal/mol). This shows that, all species, MS^- ion, IM, and IMH^+ ion, in structure (c) are interlinked by hydrogen bonds and are more stable than structure (a). In conclusion, an addition of one IM molecule to IMMSA promotes proton dissociation from MSA, which results in an ion pair formation; where the role of the second IM molecule is to stabilize the ion pair. As the proton is trapped, it would be an energy intensive proton conduction via structure (c). There are other possibilities of PT, where complex (a) can lose proton to surrounding medium and subsequently gain it, following rotation. This mechanism is explored in the following subsections.

4.3.4 Loss and gain of proton

The complex (a) can lose a proton from the N-H bond in second IM molecule to the surrounding ion or molecule, such as IM^- ion, IM, or MS^- ion. Figure 4.4 shows such PT process. The complex (a) in the figure is same as structure (4.3a). The proton is denoted by a red circle. The deprotonation energy of the complex with respect to above proton is ca. 309.20 kcal/mol and is lower compared to CH_3SO_3H, i.e., the complex has the more acidic proton. The figure shows that the loss of proton results in PT from IMH^+ in (a) to form complex (b). As described in the previous case, a proton can interact with free oxygen atoms, O1, O2, and O3, of this complex, and the resultant structures are shown in Figure B11 of the Appendix B. The final structures show the loss of O···H-C hydrogen bond interaction and increase in intermolecular distances. The calculated PA values with respect to these oxygen atoms are nearly the same, ca. 296.86 kcal/mol. The optimized structure of proton interaction with the oxygen atom, denoted by O, of complex (b) leading to complex (c) is also shown in Figure 4.4.

4.3.5 Relay of proton through structural changes

To relay the accepted proton by complex (c) further, rotation of molecules, leading to structure similar to complex (a), is necessary to reestablish the required hydrogen bonded network. There are two such ways to examine rotation barrier in the complex: (1) by initiating rotation on -SO_3H group by the freezing apical carbon atoms of IM molecules, followed by rotation of each IM molecule; or (2) by initiating the rotation of first IM molecule in the complex. A PES scan using the first possibility also includes crossing of a barrier from the staggered form of CH_3SO_3H to its eclipsed form. No TS structure was found for the rotation of IM molecule. A PES obtained using the second possibility is shown in Figure 4.4 with structures (c) to (g). The first IM molecule in the complex was

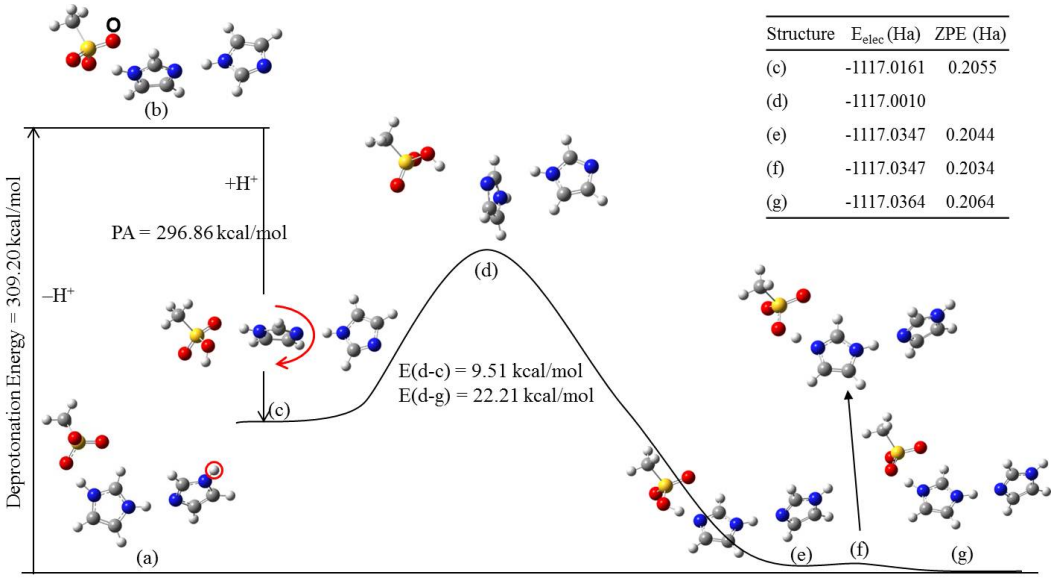

Structure	E_{elec} (Ha)	ZPE (Ha)
(c)	-1117.0161	0.2055
(d)	-1117.0010	
(e)	-1117.0347	0.2044
(f)	-1117.0347	0.2034
(g)	-1117.0364	0.2064

Figure 4.4: Structural changes in MSA···IM···IM complex through proton loss and gain. Structure (a) represents [MSA]/[IM] = 1:2. Complex (b) is obtained when complex (a) loses a proton marked by a circle. Structure (c) was obtained by subsequent gain of a proton by oxygen, denoted by O, in structure (b). IM molecule of structure (c) was then rotated in the marked direction by freezing the apical carbon of both IM molecules and S atom of MSA to obtain a PES. Structure (d) is the energy maxima, and structure (e) is the corresponding product. In structure (d), IM molecule is in 90° rotated position, which shows the hydrogen bonds between the oxygen atom of MSA and hydrogen atom of IM and between IM molecules break. In structure (e), all IM molecules are flipped and hydrogen bonds between molecules regenerated. The acidic proton is with -SO_3H group. A PES of proton transfer from MSA to IM in structure (e), structure (f) is TS, and structure (g), the corresponding product. An inset table shows negligible energy barrier for PT from structure (e) to (g).

rotated in the marked direction in steps of 10° to 180°. As the IM molecule rotates, hydrogen bonding interactions (O···H-N between MSA and IM, and N···H-N between IM and IM) weaken, and thus, the energy of the system increases. An energy maximum structure (d) was obtained at 90° rotation of the IM molecule and shows minimum hydrogen bonding interaction with the neighboring molecules. Further rotation results in regeneration of hydrogen bonding network among these molecules and decrease in the energy of the system leading to structure (e). Both IM molecules in the structure are flipped. The MSA in the structure does not lose proton to the neighboring IM molecule. A TS structure (f)

shows proton transfers from structure (e) to (g), with a negligible barrier. The final structure (g) is same as structure (a). The electronic energies, along with ZPE corrections, of structures (c) to (g) given in the inset table show a little difference in energy of structures (e), (f), and (g). This indicates that these configurations can be interchangeable at a faster rate, and at equilibrium, are indistinguishable.

Figure 4.4 also shows forward and reverse energy barriers, calculated using a PES scan, on rotation of IM molecule. The respective barriers are 9.51 and 22.21 kcal/mol. Similar results of PES scan and energy barriers were obtained for proton interaction with other oxygen atoms of complex (b) and are shown in Figures B12 and Figure B13 of Appendix B. A TS structure, corresponding to structural changes from (c) to (e) in Figure B13 of Appendix B, was also obtained and is shown in Figure B14 of Appendix B. The results show that the forward and reverse energy barriers of IM rotation (see Figure B14 of Appendix B) are 1.93 kcal/mol (1.87 kcal/mol with ZPE corrections) and 13.68 kcal/mol (13.86 kcal/mol with ZPE corrections), and are found to be slightly higher compared to IMMSA (see Figure 4.2).

The intermolecular distance (O-N distance) in IMMSA is 2.61 Å, which increases on an addition of one IM molecule. This increased distance results in reduced interaction between MS^- ion and the last IM molecule in the chain, which carries a free proton with comparatively lower deprotonation energy (from 314.16 to 309.19 kcal/mol). The lower deprotonation energy of IMMSA···IM complex in comparison with IMMSA indicates its higher proton donating ability. An excess IM interaction with IMMSA also induces PT from MSA to IM and consequently increases the concentration of charged species in the medium. All these phenomena cumulatively can lead to enhanced proton conductivity of [MSA]/[IM] = 1:2 composition system.

4.3.6 Interaction of IMMSA with two IM molecules

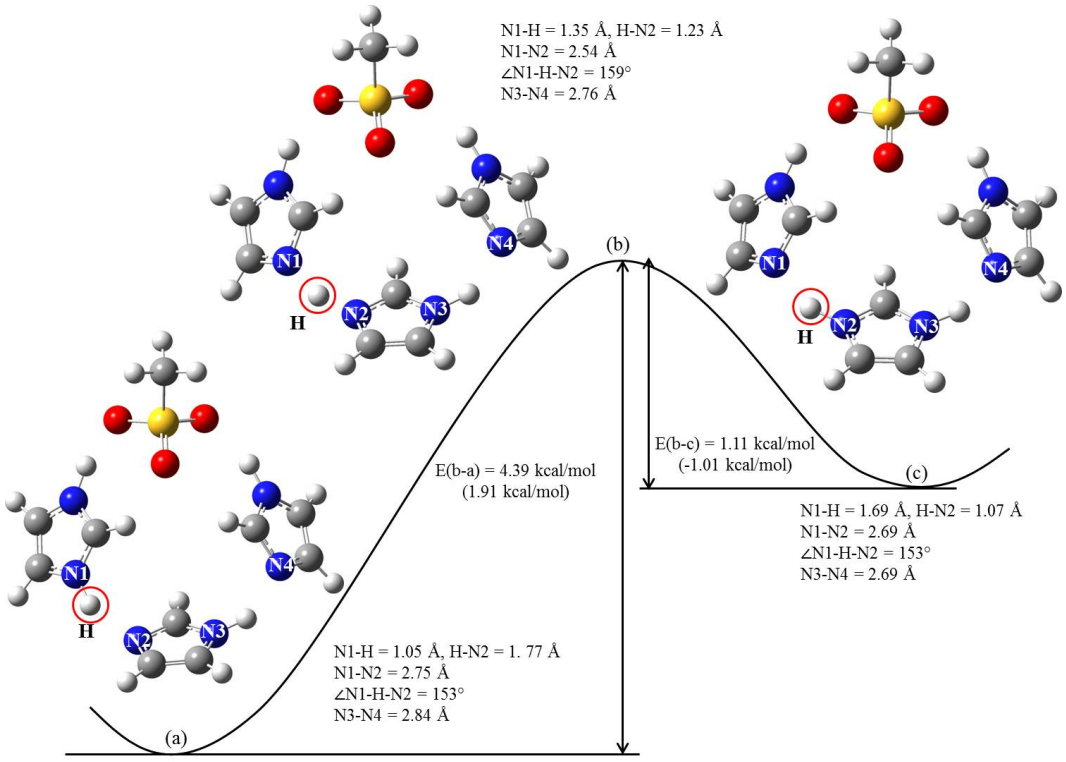

Figure 4.5: PES of proton transfer in a [MSA]/[IM] = 1:3, i.e., IMMSA with two IM molecules. Structure (a) is the resultant optimized geometry of mixture where the anion interacts with bow-shaped IM chain. N1, N2, N3, and N4, in the structure, represent nitrogen atoms, and H represents labile proton. Proton transfers from IMH^+ ion to IM molecule via the TS (b). Structure (c) is the corresponding product. The changes in atomic distance and angle along with PT barriers are also shown. Energy barriers without and with ZPE corrections (in parentheses) are reported.

To examine the effect of further increasing base content in IMMSA, one IM molecule was introduced to the complex Figure 4.4a. The resultant mixture represents [MSA]/[IM] = 1:3 composition, and the most stable geometry is shown in Figure 4.5a. The interaction energy of the complex is 30.16 kcal/mol. A comparison of PA of MS^- ion and $(IM)_3$ gives ΔPA = 62.06 kcal/mol (< 90 kcal/mol), which reflects PT from MSA to IM molecule. A bow-shaped medium strength hydrogen-bonded network is formed. The MS^- ion in the complex is hydrogen bonded with two neighboring IM species: IMH^+ ion and a neu-

tral IM molecule. This IMH^+ ion is further hydrogen-bonded with another IM molecule through N1-H···N2 bond, resembling an Eigen ion,[199] where N1 and N2 are their corresponding nitrogen atoms and H is the hydrogen atom between them. In the figure, N3 and N4 represent other two nitrogen atoms, and N3-N4 distance denotes the intermolecular distance between IM molecules. The figure also shows a PES of structure (a) leading to (c) via the TS structure (b). The ZPE values are 0.280606, 0.27662, and 0.280057 Ha for (a), (b), and (c), respectively. The atomic distances indicate that proton transfers from N1 to N2 with a forward energy barrier of 4.39 kcal/mol (1.91 kcal/mol with ZPE corrections) and a reverse barrier of 1.11 kcal/mol (1.01 kcal/mol with ZPE corrections). These barriers are slightly lower than those in IMMSA···IM system (see Figure 4.3). This is due to decreased N1-N2 distances. The lower barriers indicate the ease of PT in this system. A comparison of forward and reverse energy barriers implies faster PT from structures (c) to (a) and a higher concentration of structure (a) at equilibrium. All molecules in the system are hydrogen bonded; hence, proton removal will be energy intensive. An alternate possible way through the formation of the cation is discussed here.

When an excess proton present in the medium interacts with the above structure (a), the resultant geometries will depend on which of three oxygen atoms in the anion it combines with. The resultant minimum energy configurations obtained from interaction of the excess proton with different oxygen atoms O1, O2, and O3 of the complex 4.5a along with atomic distances are shown in Figure B15 of the Appendix B. The addition of an excess proton results in a decrease in MSA interactions with the surrounding species. The resultant structure obtained from removal of hydrogen atom, indicated by an arrow in structure (b) of Figure B15, and a subsequent PES scan obtained from rotation of IM molecule are shown in Figure B16 of Appendix B. This shows a higher rotational barrier (15.64 kcal/mol) and is directly related to number of hydrogen bonds breaking in the process.[176] Similar rotational barriers are expected from structures (c) and (d) in Figure B15 of the

Appendix B.

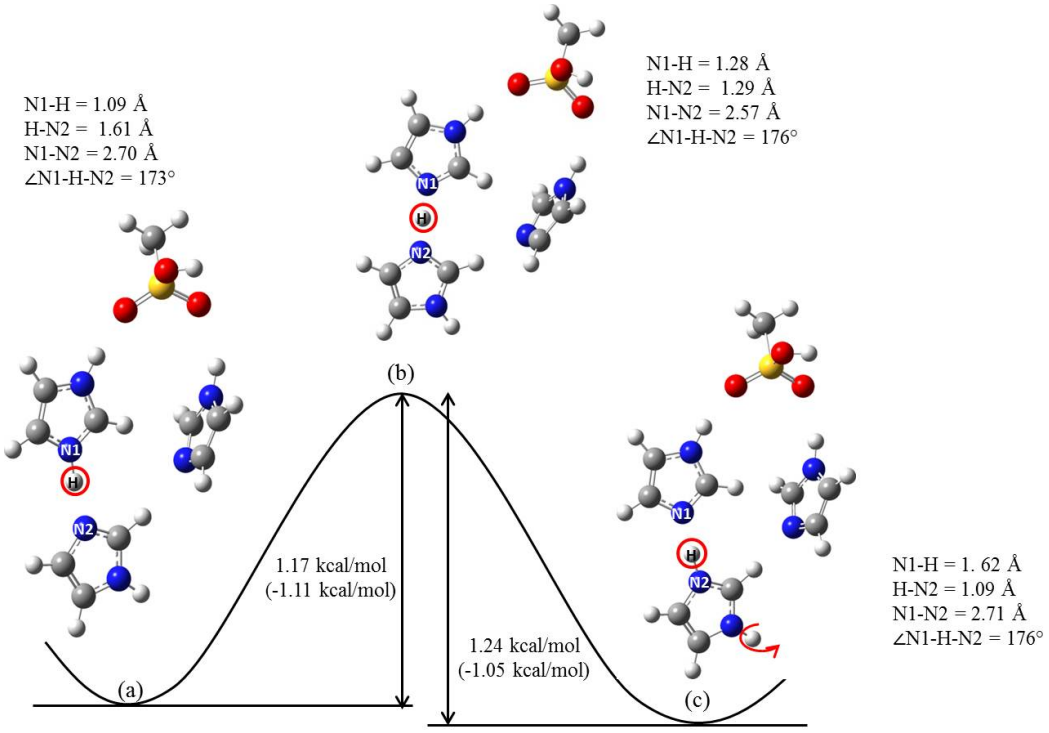

Figure 4.6: PES of proton transfer in [MSA]/[IM] = 1:3 with an excess proton. Structure (a) is the resultant optimized geometry of the complex. N1 and N2, in the structure, represent nitrogen atoms of IMH^+ ion and IM molecule, respectively, and H represents labile proton. Proton transfers from IMH^+ ion to IM molecule via the TS (b). Structure (c) is the corresponding product. The changes in atomic distance and angle along with PT barriers are shown. Energy barriers without and with ZPE corrections (in parentheses) are reported.

There also exists a relatively higher energy conformer, structure (e) in Figure B15 of Appendix B, which can facilitate proton conduction better than all other possibilities. The proton transport via this structure is detailed in Figure 4.6. Structures (a), (b), and (c), in the figure, represent initial, TS, and final geometry of the IMMSA···IM···IM system with an excess proton along with atomic distances, indicating PT. In structure (a), two imidazole species, IMH^+ ion and IM are hydrogen bonded with MSA. The third IM is hydrogen bonded with these species with N-H···N2, where N1 and N2 correspond to nitrogen atoms of IMH^+ ion and IM, respectively, and a hydrogen atom, H, is bonded with

N1, and C-H···N. N1-N2 distance, as shown in the figure, is 2.70 Å, which is lower than that in structure 4.5a. This is due to relatively weaker hydrogen bond interactions of third IM with its neighbors. The bond angle, ∠N1-H-N2 = 173°, indicates a linear hydrogen bond between IMH^+ and IM. The lower N1-N2 distance and linear hydrogen bond result in smaller PT barrier from IMH^+ ion to IM, i.e., 1.17 kcal/mol (1.11 kcal/mol including ZPE corrections). The results are in agreement with the previous work[200–203] of PT barrier dependency on hydrogen bond length, between donor and acceptor, and its directionality. The reverse PT barrier 1.24 kcal/mol (1.05 kcal/mol including ZPE corrections) is nearly equal to forward barrier, which indicates that these configurations are interchangeable at the cost of low energy, and at equilibrium, concentration of these complexes will be nearly same.

For further proton transport, IMH^+ ion formed in structure (c) must lose the proton, marked by a curved arrow. The deprotonation energy of the complex (c) with respect to the proton is ca. 230 kcal/mol. To understand the next step in proton conduction mechanism, geometry optimization of the complex (c) was performed after removal of the proton, and results are presented in Figure 4.7. The figure shows changes in geometry and corresponding energy during optimization. In the figure, the initial structure (a), on which geometry optimization was performed, was obtained from removing the marked proton from the structure (4.6c). Structures (b) and (c) are intermediate structures, and structure (d) is the final optimized structure. The figure shows that there is a continuous decrease in energy of the system. In structure (b), right IM molecule starts rotating and loses C-H···N hydrogen bond interaction, relatively weaker in strength, with left imidazole-chain and O···H-N with -SO_3H group. Structure (c) shows regeneration of hydrogen bond with -SO_3H, i.e., O-H···N. There is no change in the structure of left imidazole-chain. Further optimization of structure (c) shows a steep decrease in energy, which occurs due to PT from -SO_3H to right IM molecule and formation of N···H-N hy-

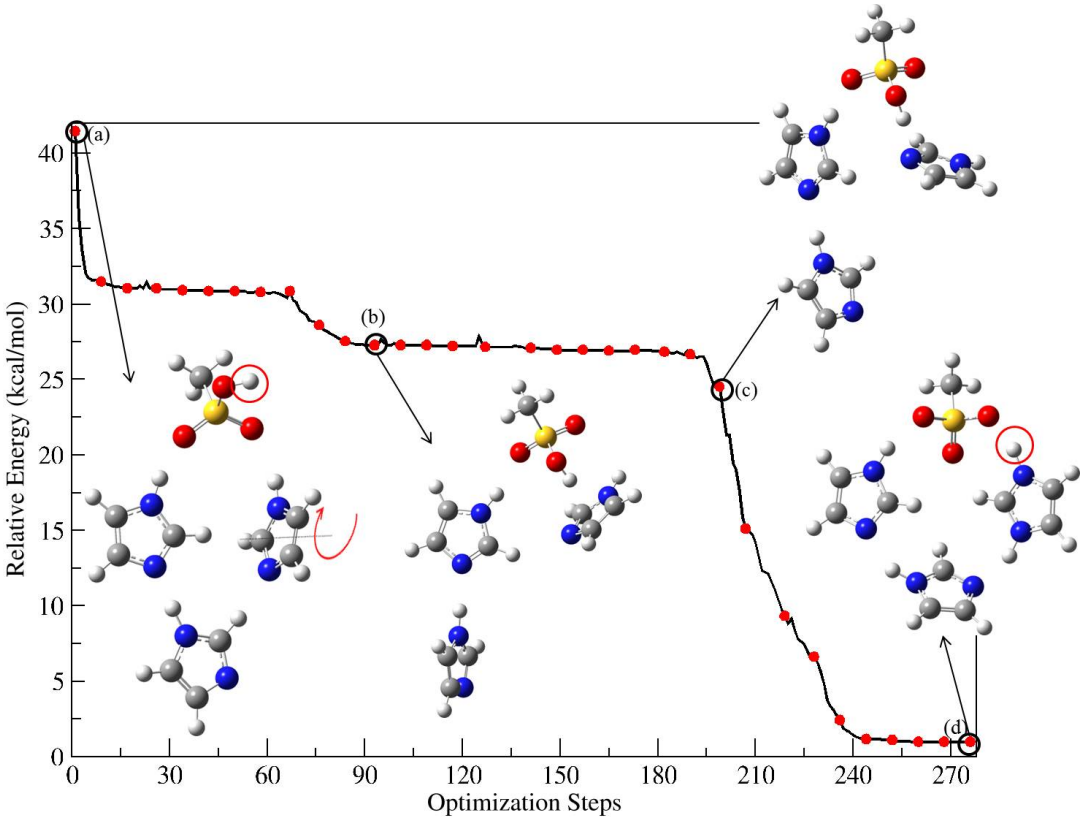

Figure 4.7: Geometry optimization of complex (a), obtained from structure 4.6c after losing its proton from IMH^+. Figure shows a barrierless rotation of IM molecule in the complex during optimization. Structures (b) and (c) represent intermediate geometry of the complex (a), and structure (d) is the final structure.

drogen bond with left imidazole-chain. The final optimized structure is the same as structure (4.5a). In this cyclic path (shown in Figure 4.8), structure (4.5a) → structure (4.6a) arises from proton gain, structure (4.6a) → structure (4.6c) from proton transfer within the structure, and structure (4.6c) → structure (4.7a) is obtained from removal of proton from structure (4.6c). Species in structure (4.7a) reorganizes to give structure (4.7d). In this mechanism, there shows no rotation barrier, unlike previous cases. Structure (4.7d) is similar to structure (4.5a) and thus this cyclic process occurs and can lead to enhanced proton conduction in IMMSA with two IM molecules. Thus, it can be concluded that a collective examination of proton affinity, energy barrier, and hydrogen bonding is neces-

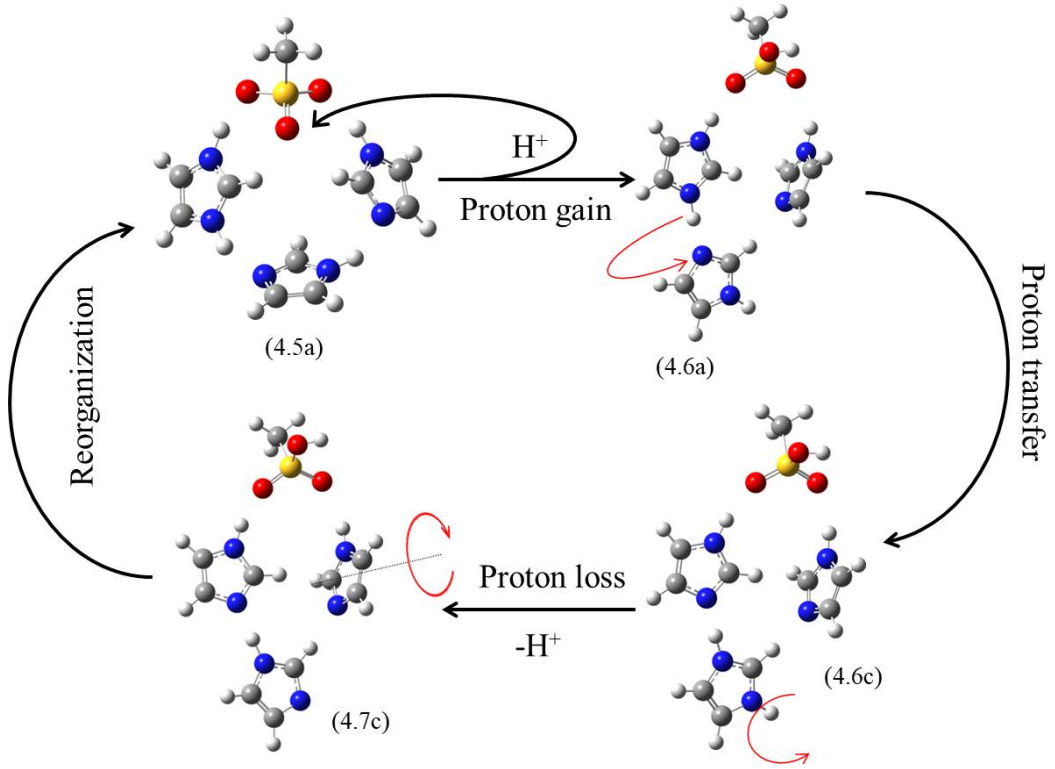

Figure 4.8: Schematic of proton transport pathway in [MSA]/[IM] = 1:3, i.e., IMMSA with two IM molecules.

sary to predict proton conduction in base rich IM based ILs.

Chapter 5

Summary and outlook

5.1 Conclusions

The salient features of the thesis are as follows:

- **Chapter 1** of thesis presents a literature on humidified and non-humidified PEMs.
- **Chapter 2** of thesis describes, using MD simulations, the effect of the sulfonate group charge delocalization of hydrated Nafion polymer membrane on its structural and dynamical properties. The sulfur-sulfur RDFs suggest that the repulsion between the sulfonate groups decreases with an increase in charge delocalization. The RDFs suggest that sulfonate-water and sulfonate-hydronium interactions decrease slightly with charge delocalization. The average water cluster size decreases significantly with an increase in charge delocalization. With small amounts of delocalization, the water diffusion increases because the charge is not concentrated on the sulfonate group alone which allows the water molecules not to be trapped in the vicinity of the sulfonate group. However, with increasing charge delocalization the water diffusion decreases due to a large decrease in the water cluster sizes. Hence, it can be concluded that the diffusion coefficients of water molecules can be increased slightly by suitably adjusting the amount of charge delocalization. This effect can be useful for reverse osmosis where PEMs are used and water diffusion is critical. The results from this work can be applied to examine other functionalized polymer membranes with sulfonic, phosphoric or carboxylic acid groups which can offer

high proton conductivity in hydrated environments.

- **Chapter 3** of thesis describes dynamical properties of [dema][TfO] doped PBI using MD simulations. The cation-cation and anion-anion RDFs at 50 IL wt% illustrates a structured arrangement of ions due to ionic clusters. The RDFs shows that anions interact strongly with the hydrogen atoms (attached to the imidazole nitrogen atoms) of the PBI. Compared to anions, the cation interactions are less likely with PBI. This suggests that proton transfer in [dema][TfO] IL doped PBI is likely to occur via cationic clusters and supports the hypothesis on proton transport proposed by Noto et al.[149] The magnitude of diffusion coefficients of cations is slightly higher than anions. Similar trends in diffusion coefficients are seen from the MD simulations on neat and hydrated [dema][TfO] IL by Chang et al.[204] The calculated ionic conductivities show qualitative agreement (see Figure 3.7) with experimental ionic conductivities. The difference in the magnitude of ionic conductivity between simulations and experiments is from the limitation of the classical (non-polarizable) force fields. The development of polarizable or reactive force-fields to calculate ionic conductivity in such systems can be the focus of future activities.

- **Chapter 4** of thesis describes mechanism of proton transfer in imidazolium methanesulfonate (IMMSA) with varying IM content using quantum chemistry calculations. The results show that in IMMSA ([MSA]:[IM] = 1:1) the acidic proton of MSA does not transfer to IM molecule, and this can be attributed to high gas phase ΔPA value. However, the IM + MSA gas phase pair does not predict the correct protonation state of these species in the liquid due to the absence of solvent stabilization of the ion species. The proton conduction in the complex occurs with an IM molecule with a small rotational barrier of ca. 0.20 kcal/mol. When IMMSA interacts with one IM molecule ([MSA]/[IM] = 1:2 composition), MSA donates a proton to IM leading to

MS···IMH···IM complex, where the role of the second IM molecule is to stabilize the ion pair. This proton transfer from MSA to IM results in higher concentration of charged ions in the system compared to IMMSA. The calculated proton transport barrier from IMH^+ to IM is 4.93 kcal/mol. However,the IM rotational barrier of 9.51 kcal/mol is higher compared to IMMSA. When IMMSA interacts with two IM molecules ([MSA]/[IM] = 1:3 composition), in the presence of excess proton, the barrier for proton transport along the IMH^+ to IM chain was the minimum, i.e., $\backsim$1.17 kcal/mol. The removal of a proton from this structure leads to configurational changes involving spontaneous rotation of molecules, without any barrier. The results presented in the investigation qualitatively explain higher proton conductivity of base rich, IM based ILs.

5.2 Future directions

Base rich ILs are known to show enhanced conductivity.[9,73,91] Noda et al.[73] calculated diffusion coefficients by PFGSE-NMR in imidazolium bis(trifluoromethanesulfonyl) ([Im][TFSI]). The authors reported that fast proton exchange occurs between the IMH^+ cation

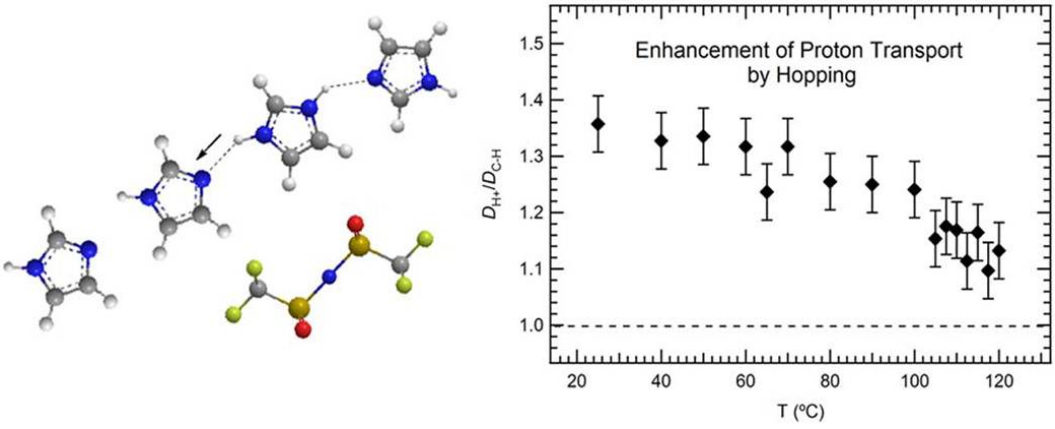

Figure 5.1: Schematic of proton hopping in [Im][TFSI]. Reprinted with permission from work of Hoarfrost et al.[91] Copyright American Chemical Society.

and IM, with excess IM. The authors proposed that proton conduction occurs via vehicular and hopping mechanisms and supported this by Direct current polarization measurements. Nakamoto et al.[9] synthesised PIL with bis(trifluoromethanesulfonyl)imide (HTFSI) acid and BIM base with varying amount of BIM. Similar to the previous study, the authors observed fast proton exchange reactions between the protonated and free BIM, especially with excess BIM. The authors proposed this PIL as a suitable electrolyte in anhydrous conditions. Hoarfrost et al.[91] examined proton transport in [Im][TFSI] IL using NMR and QENS techniques, to explore proton (see Figure 5.1) hopping mechanism in IM rich conditions.

However, there has been no computational study to investigate proton hopping in base rich imidazolium ILs. A future direction in this research area is to deploy AIMD simulations to calcualate proton/ion diffusion coefficients and ionic conductivity. The outcome of this investigation is expected to support/validate existing experimental investigations on IMH^+ ILs. These simulations can also be extended to examine proton hopping mechanism in IL doped polymer membranes which will be in better agreement with experimental measurement of proton conductivity.

Appendix A

Table A1: Comparison of calculated (this work) and experimental PA. (PA values in parentheses are calculated using B3LYP-D3 functional).

System	PA (kcal/mol)	PA (kcal/mol)
IM	226.09 (226.54)	225.3[205]
DEMA	231.61 (234.86)	233.3[206]
$TFSI^-$	294.4 (295.40)	294[207]
$CF_3SO_3^-$	299.32 (299.87)	305[208]
MS^-	319.9 (319.97)	321[209]
CF_3COO-	319.9 (320.22)	324[210]
CH_3COO^-	345.38 (346.02)	349[210]

Table A2: Chemical formula of each ion pair, ΔpK_a = (pK_a(base) - pK_a(acid)) values of the IL, calculated using experimental aqueous pK_a values of base and acid, calculated gas phase ΔPA = (PA of anion - PA of base), and final position of the proton in each ion pair. (ΔPA values in parentheses are calculated using B3LYP-D3 functional).

Ion Pair	ΔpK_a	ΔPA (kcal/mol)	Final position of proton
DEMA-HTFSI	20.5	62.80 (62.59)	Proton transfers to DEMA
DEMA-CF_3SO3H	29.14	67.71 (67.71)	Proton transfers to DEMA
DEMA-CH_3SO_3H	12.42	87.92 (87.16)	Proton transfers to DEMA
DEMA-CF_3COOH	10.27	88.29 (87.41)	Proton transfers to DEMA
DEMA-CH_3COOH	5.74	113.77 (113.21)	Proton remains with CH_3COOH

Table A3: System sizes of all [dema][TfO]-PBI (dodecamer, 32 chains) compositions.

Number of IL pairs	wt% of [dema][TfO]	Total no. of atoms (IL+PBI)
832	50	46,400
1,696	67	70,592
2,496	75	92,992
3,328	80	116,288
4,064	83	136,896

Appendix B

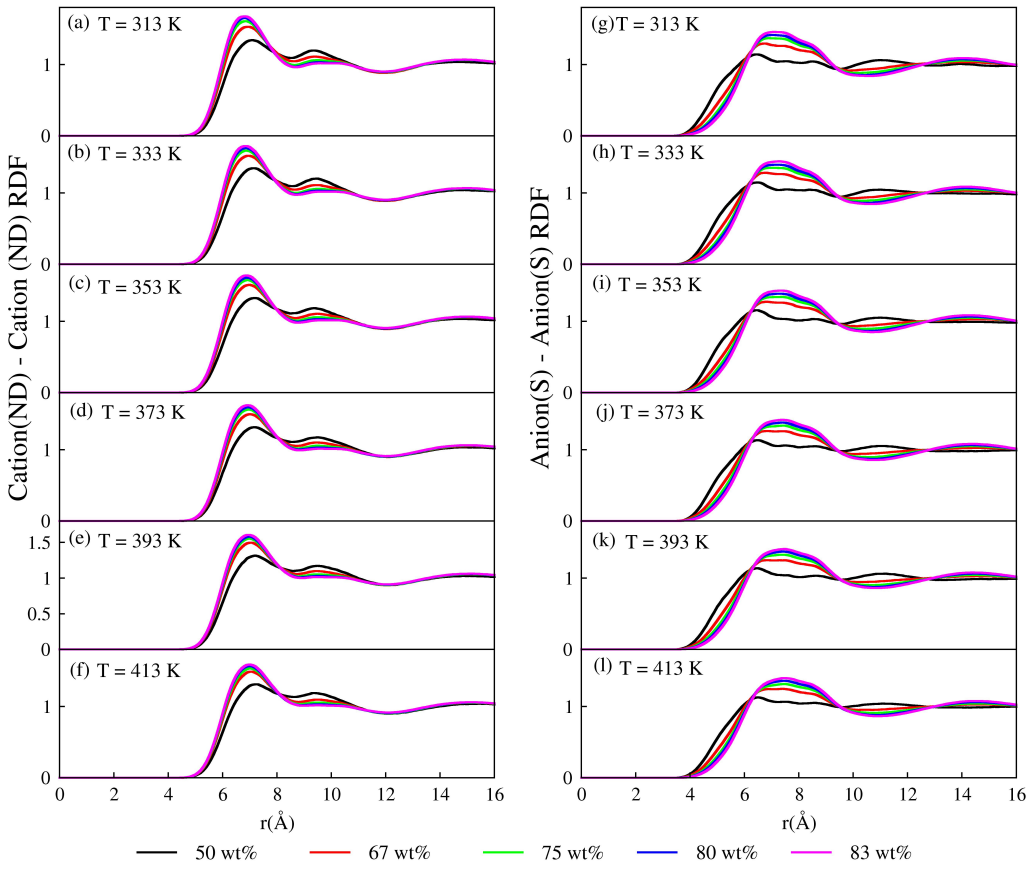

Figure B1: Cation-Cation and Anion-Anion RDFs (T = 313 K, 333 K, 353 K, 373 K, 393 K, and 413 K).

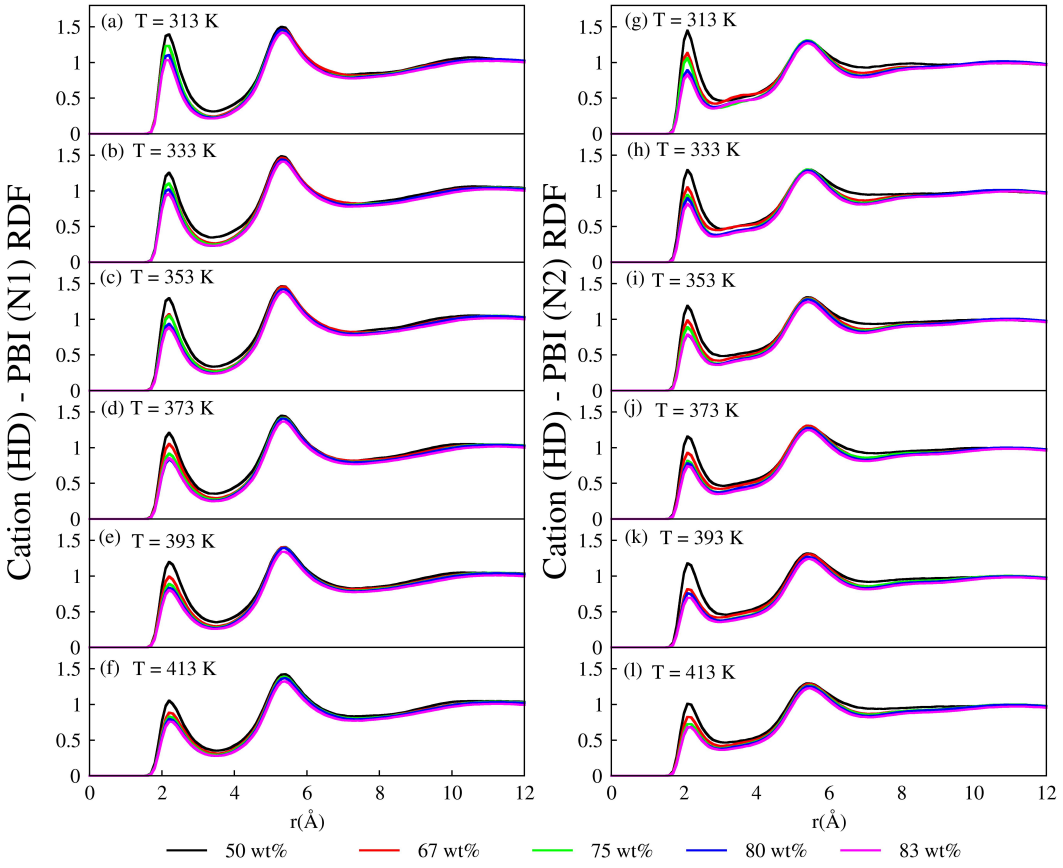

Figure B2: Cation-PBI RDFs (T = 313 K, 333 K, 353 K, 373 K, 393 K, and 413 K).

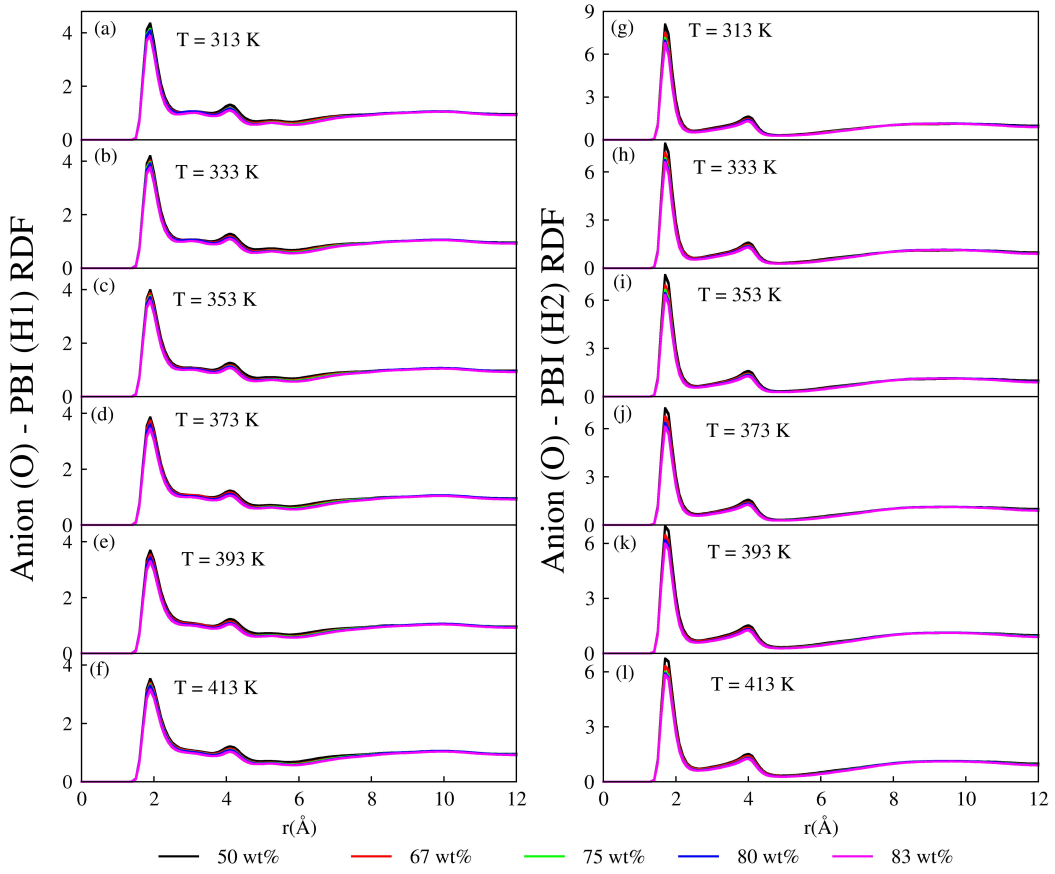

Figure B3: Anion-PBI RDFs (T = 313 K, 333 K, 353 K, 373 K, 393 K, and 413 K).

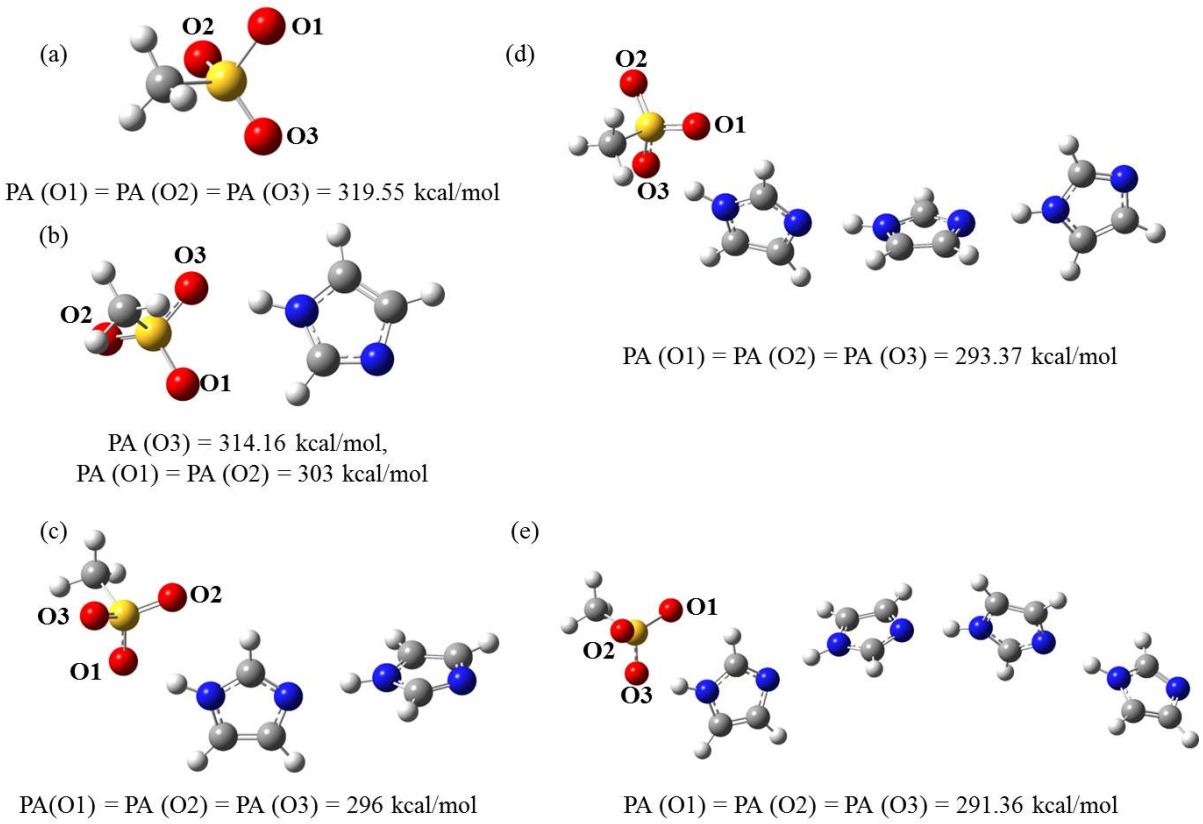

Figure B4: Structure and gas phase proton affinity (PA) of (a) MS^- ion (b) MS^- ion with one IM (c) MS^- ion with two IM, (d) MS^- ion with three IM, and (e) MS^- ion with four IM molecules.

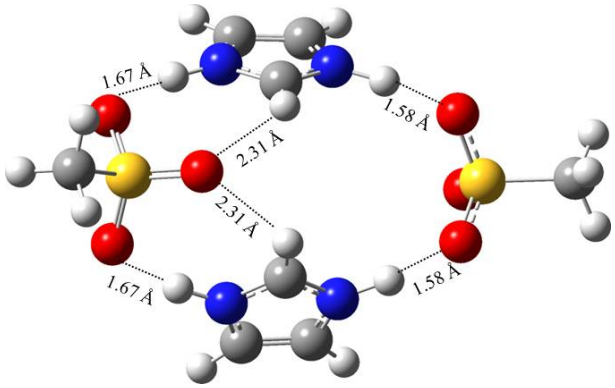

Figure B5: Dimer of IMMSA (Hydrogen bond distances are shown with dotted lines).

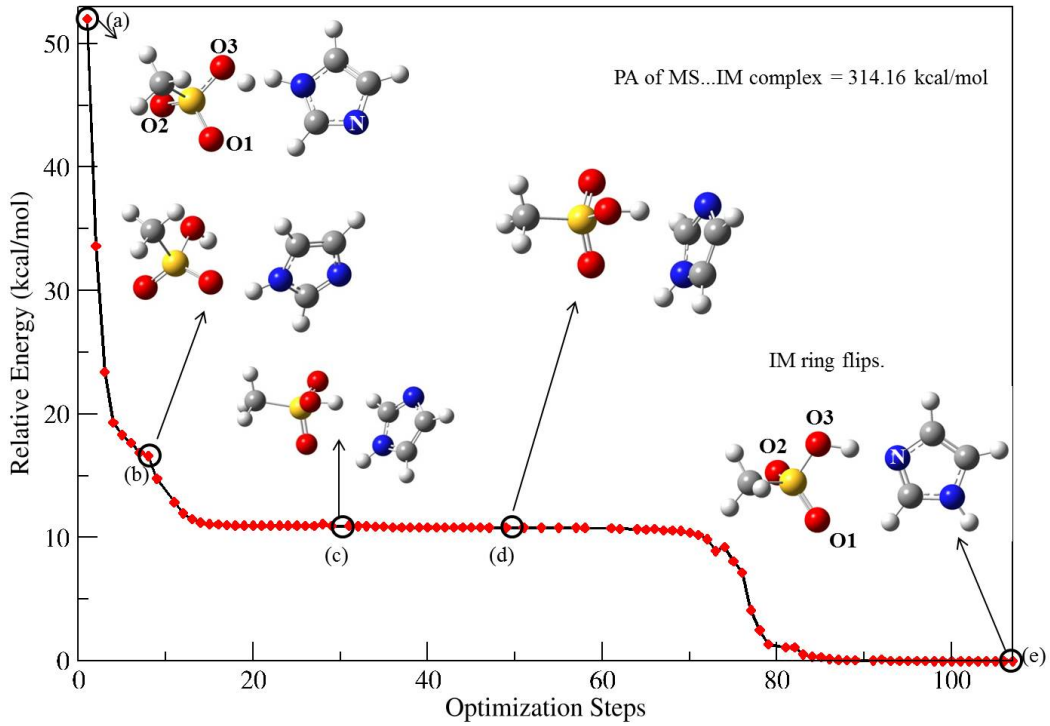

Figure B6: Optimization of MS...IM complex with a proton near oxygen atom, O3. The changes in geometry of complex are shown in structures (a) to (e). This proton causes repulsion between the newly formed O3–H bond and H–N bond. There is a continuous decrease in energy and finally the IM ring flips (see structure (e)).

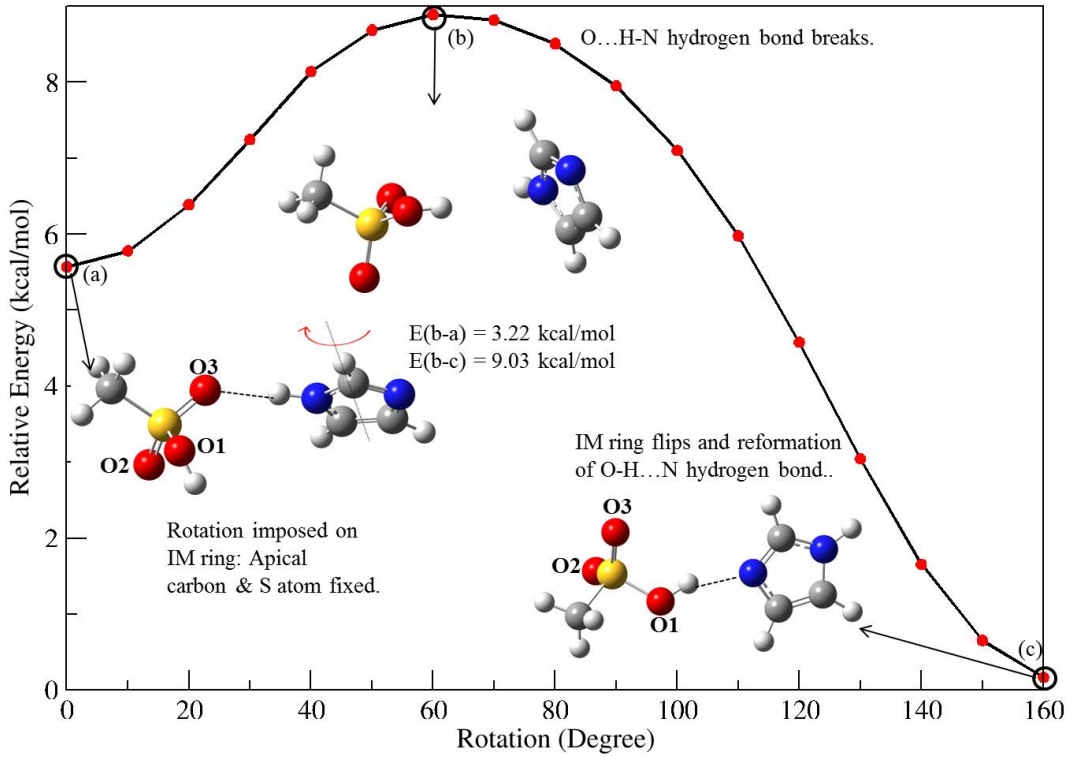

Figure B7: PES scan of IM in IMMSA complex (a), obtained from interaction of a proton to oxygen atom, O1 of MS...IM complex, by imposing rotation of IM molecule in the marked direction by freezing the apical carbon of IM and S atom of MSA. Hydrogen bond O...H–N is shown by a dotted line. The hydrogen bond completely breaks at structure (b), showing a peak. Structure (c) shows the completely flipped IM molecule with hydrogen bond regenerated between MSA and IM molecule. The calculated forward energy barrier, using TS structure, is 0.20 kcal/mol (0.24 kcal/mol with ZPE corrections) and reverse energy barrier is 11.00 kcal/mol (10.64 kcal/mol with ZPE corrections).

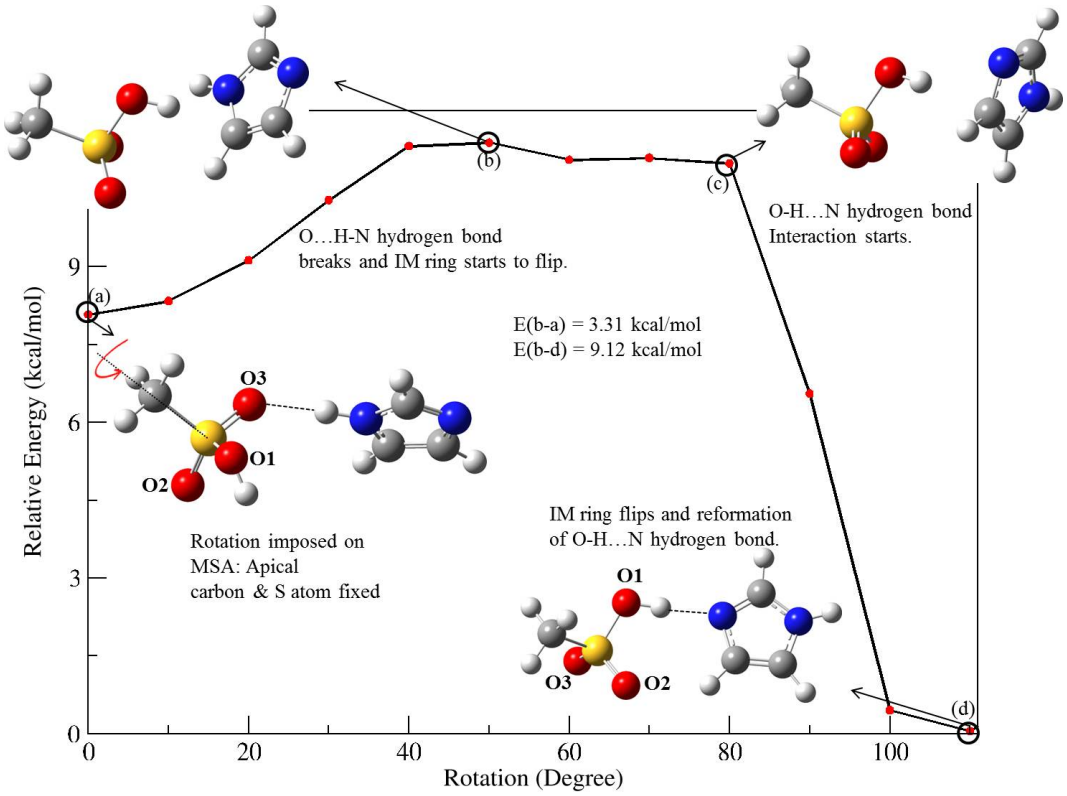

Figure B8: PES scan of MSA in IMMSA complex (a), obtained from interaction of a proton to oxygen atom, O1 of MS...IM, by imposing rotation of $–SO_3H$ groups of MSA molecule in the marked direction by freezing the apical carbon of IM and S atom of MSA. Hydrogen bond O...H–N is shown by a dotted line. Structure (b) was obtained after 50° rotation where hydrogen bond breaks. On further rotation, at structure (c), O-H and N-H bonds repulsion occurs leading to rotation of IM molecule. Structure (d) shows a completely flipped IM molecule with regenerated hydrogen bonding between MSA and IM molecule.

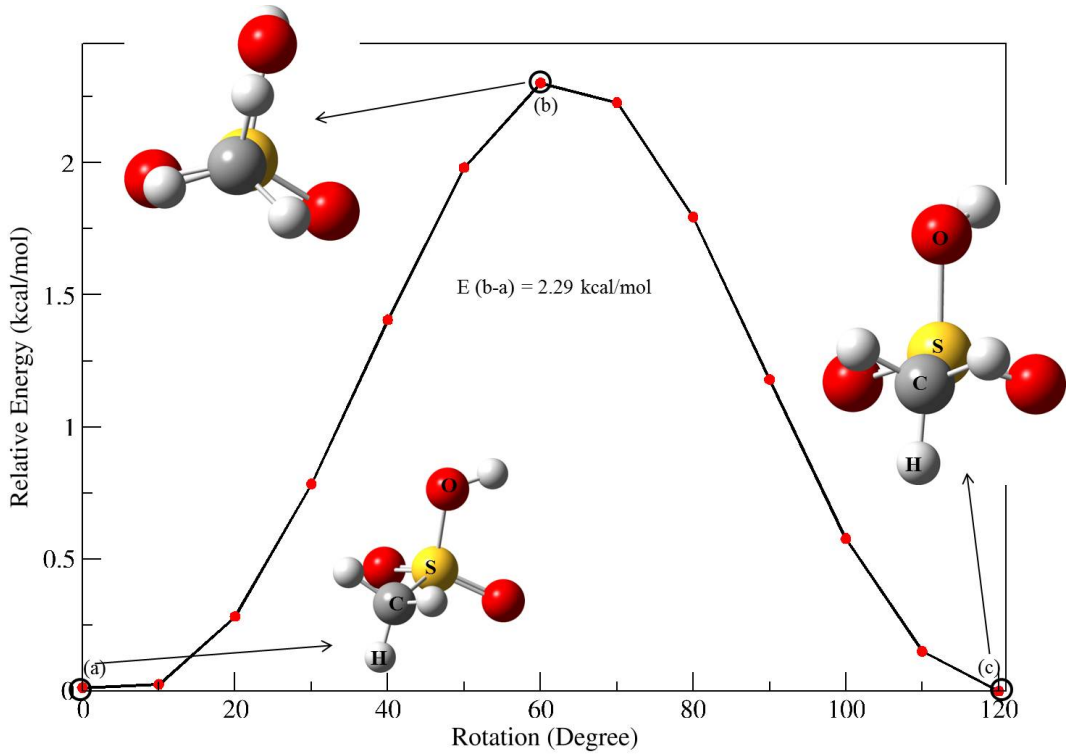

Figure B9: PES scan of CH_3SO_3H by changing dihedral angle between H-C-S-O atoms as denoted in structure (a). Structure (a) shows staggered form of the molecule. Further, increase in the dihedral angle in structure (a) results in an increase in the energy of the system. Structure (b), at the maxima, is an eclipsed form of the molecule. Further with increasing dihedral angle, the staggered form is obtained as seen in structure (c). The energy barrier of $–SO_3H$ rotation is 2.29 kcal/mol. The calculated forward barrier, using TS structure, is 2.31 kcal/mol (2.04 kcal/mol with ZPE).

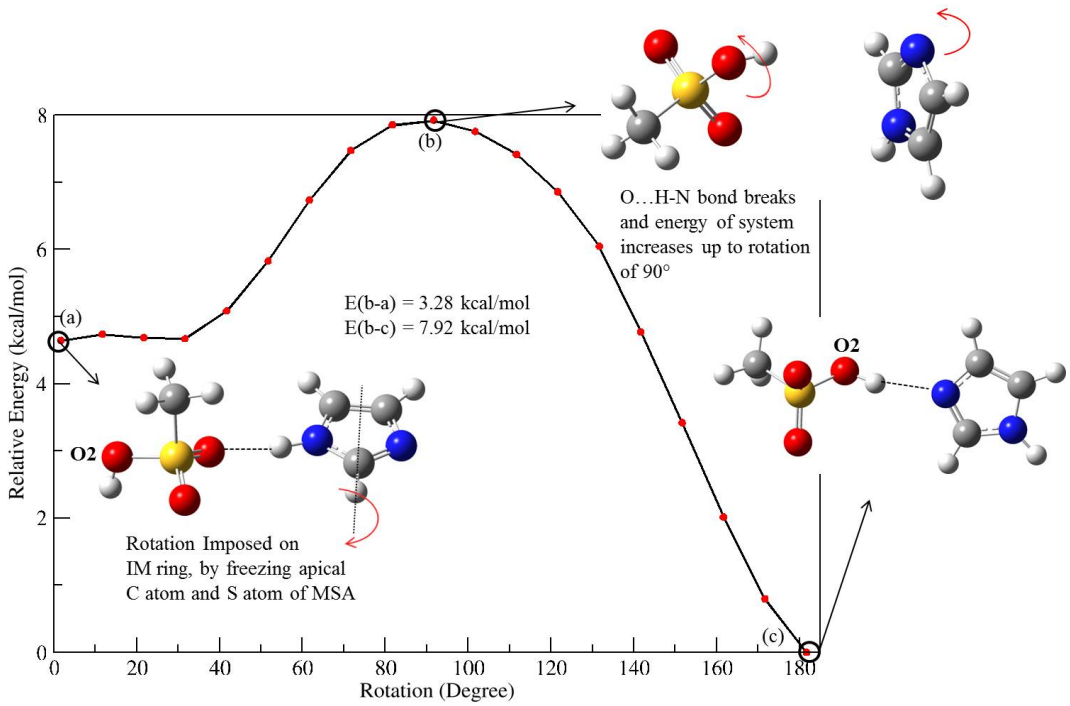

Figure B10: PES scan of IM in IMMSA complex (a), obtained from the interaction of a proton with oxygen atom, O2 of MS...IM. IM molecule was rotated in the marked direction by freezing the apical carbon of IM and S atom of MSA. Structure (b) shows that on rotation of IM molecule up to 90°, the hydrogen bond (shown by dotted line), between the acidic hydrogen of IM and O atom of MSA breaks. Structure (c) is final structure in which the hydrogen bond is regenerated. The calculated forward barrier, using TS structure, is -0.11 kcal/mol (-0.06 kcal/mol with ZPE corrections) and the reverse barrier is 10.86 kcal/mol (10.52 kcal/mol with ZPE corrections).

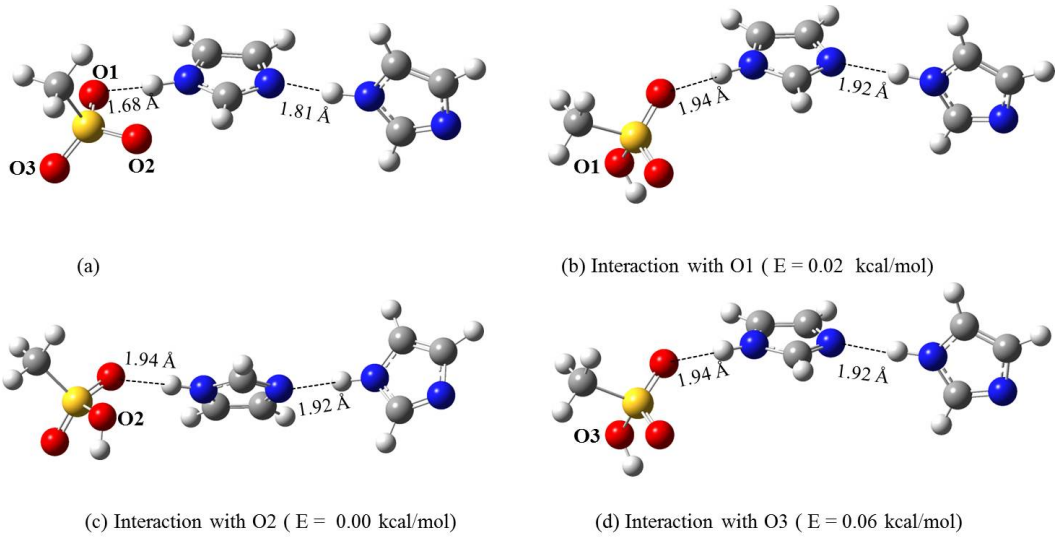

Figure B11: Interaction of a proton with different oxygen atoms, O1, O2, and O3, in MS...IM...IM complex (a). PA of all the three O atoms is $\backsim$296 kcal/mol. Structures (b), (c) and (d) were obtained when O1, O2, and O3, respectively, of MS^- ion in the complex (a) interacts with a proton. Configuration of structures (b) and (d) is same. The relative energies (including ZPE corrections) of complexes (b) and (d) with respect to structure (c) are shown in parentheses which show all structures are equally stable.

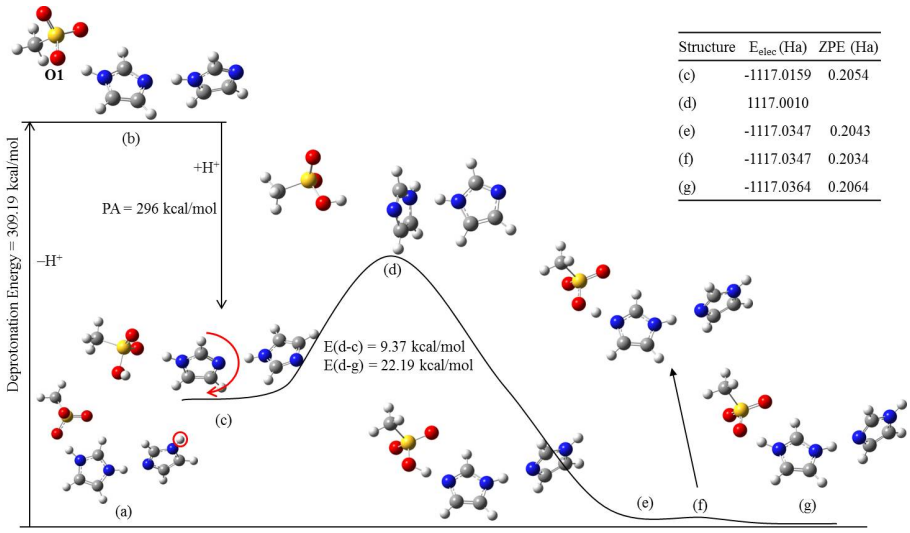

Figure B12: Structural changes in MSA...IM...IM complex through proton loss and gain. Complex (b) is obtained when complex (a) loses a proton marked by a circle. Structure (c) was obtained by subsequent gain of a proton by oxygen O1, in structure (b). PES scan of IM molecule of structure (c) was then performed by rotation in the marked direction by freezing the apical carbon of both IM molecules and S atom of MSA to obtain a PES. Structure (d) is the energy maxima and structure (e) is the corresponding product. In structure (d), IM molecule is in 90° rotated position, which show the hydrogen bonds between the oxygen atom of MSA and hydrogen atom of IM and between IM molecules break. In structure (e), all IM molecules are flipped and hydrogen bonds between molecules are regenerated. The acidic proton is with $–SO_3H$ group. A PES of proton transfer from MSA to IM in structure (e) gives structure (f), a transition state, and structure (g), the corresponding product. Inset table shows that there is negligible energy barrier for PT from structure (e) to (g).

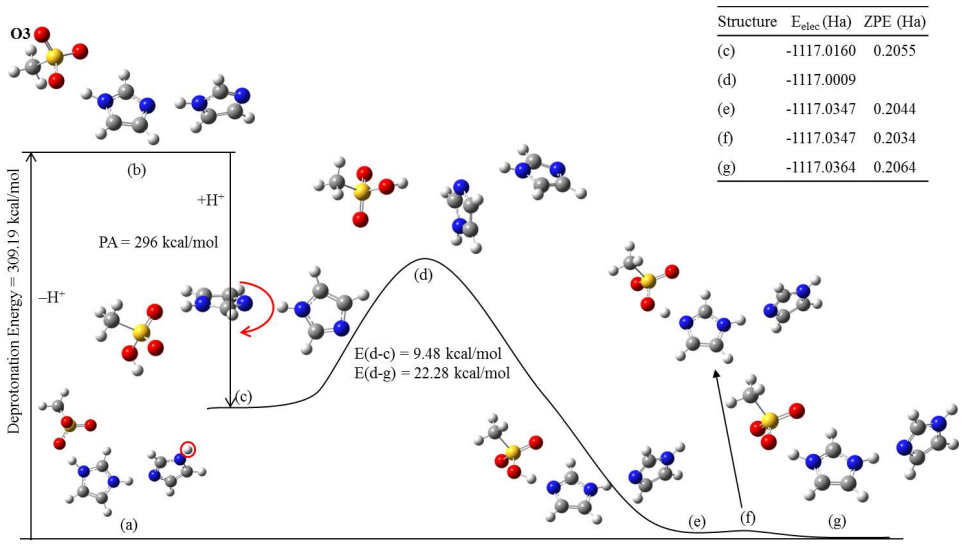

Structure	E_{elec} (Ha)	ZPE (Ha)
(c)	-1117.0160	0.2055
(d)	-1117.0009	
(e)	-1117.0347	0.2044
(f)	-1117.0347	0.2034
(g)	-1117.0364	0.2064

Figure B13: Structural changes in MSA...IM...IM complex through proton loss and gain. Complex (b) is obtained when complex (a) loses a proton marked by a circle. Structure (c) was obtained by subsequent gain of a proton by oxygen, O3 in structure (b). PES scan of IM molecule of structure (c) was then performed by rotation in the marked direction by freezing the apical carbon of both IM molecules and S atom of MSA to obtain a PES. Structure (d) is the energy maxima and structure (e) is the corresponding product. In structure (d), IM molecule is in 90° rotated position, which show the hydrogen bonds between the oxygen atom of MSA and hydrogen atom of IM and between IM molecules break. In structure (e), all IM molecules are flipped and hydrogen bonds between molecules are regenerated. The acidic proton is with $–SO_3H$ group. A PES of proton transfer from MSA to IM in structure (e) gives structure (f), a transition state, and structure (g), the corresponding product. Inset table shows that there is negligible energy barrier for PT from structure (e) to (g).

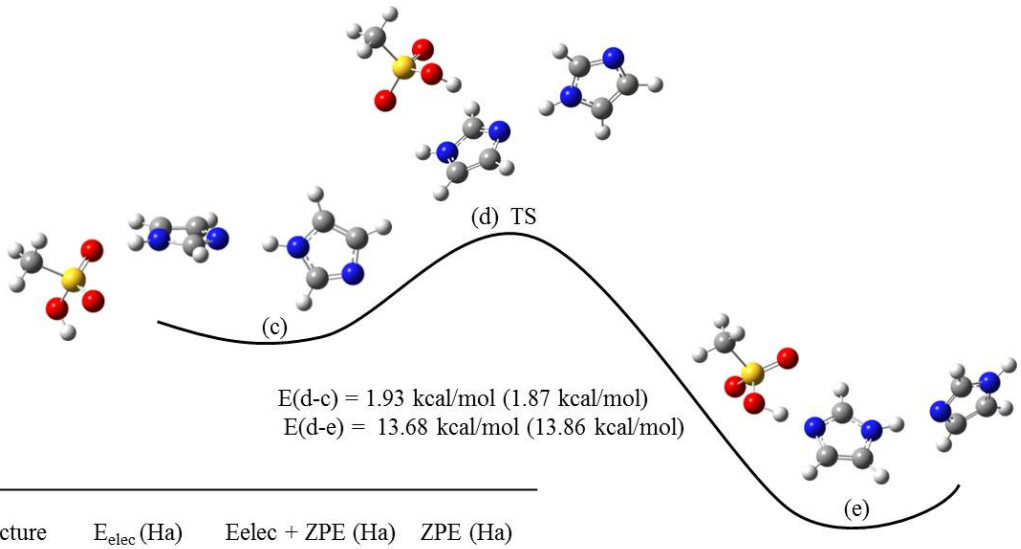

Structure	E_{elec} (Ha)	Eelec + ZPE (Ha)	ZPE (Ha)
(c)	-1117.01602266	-1116.810466	0.205557
(d)	-1117.01294333	-1116.807472	0.205471
(e)	-1117.03475888	-1116.830274	0.204485

Figure B14: The structure (c) is the same structure as in Figure B13 (c). TS structure (d) for IM rotation in MSA...IM...IM complex. The ZPE corrected energy barriers are given in parenthesis.

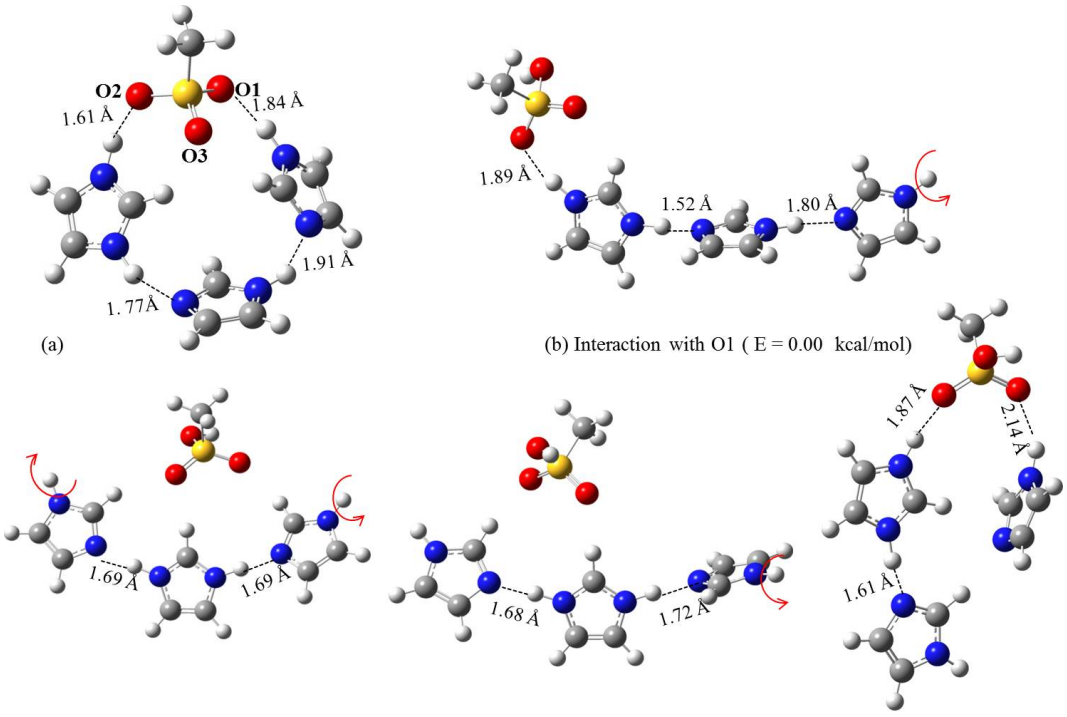

Figure B15: Interaction of an excess proton with different oxygen atoms of MS^- ion in MS...IMH...IM...IM complex (a). The PA with three O atoms is $\backsim$236 kcal/mol. The curved arrow shows the proton which can be donated to surrounding medium. Structures (b), (c) and (d) were obtained when O1, O2, and O3, respectively, of MS^- ion in the complex (a) interacts with a proton. The relative energies (including ZPE corrections) of complexes (b) and (d) with respect to structure (c) are shown in parenthesis which show that structure (a) is the most stable and structures (c) and (d) are equally stable. A relatively higher energy conformer (e) also exists which was obtained through reorganization of IM molecules.

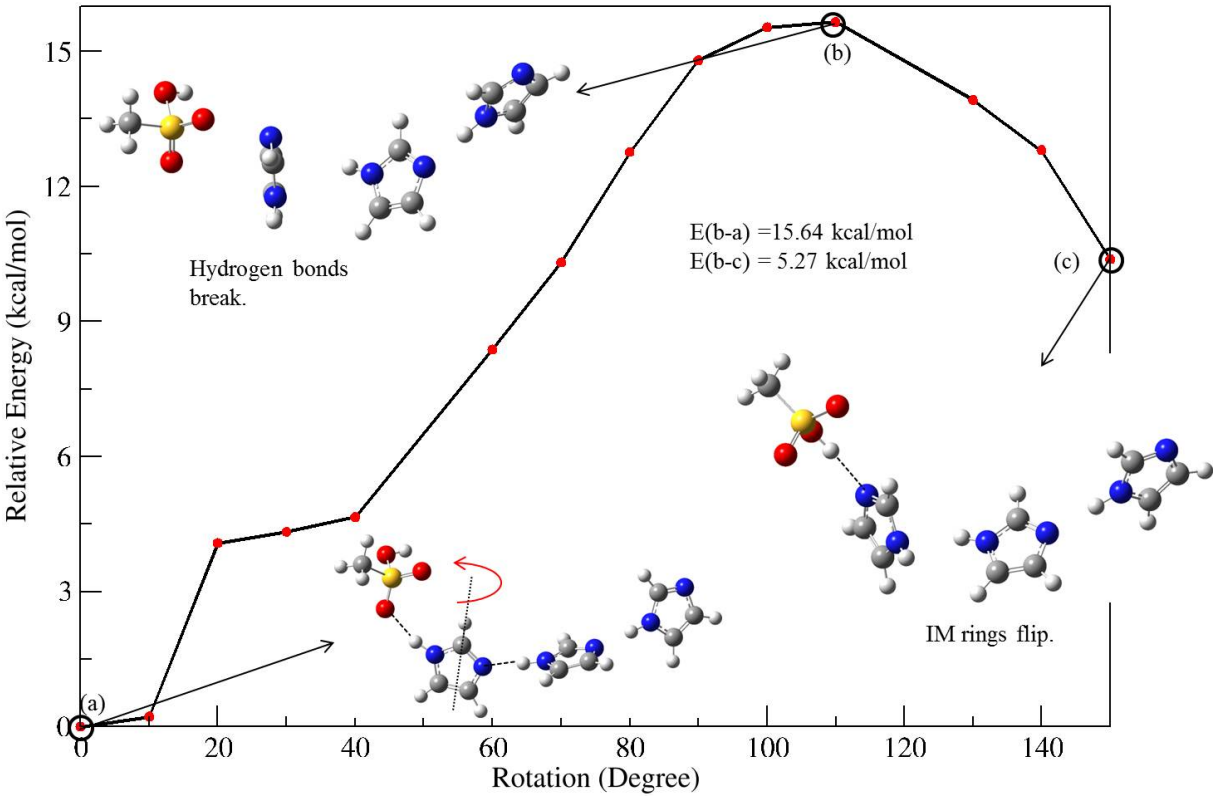

Figure B16: PES scan of rotation of IM molecule in MSA...IM...IM...IM complex in the marked direction. Structure (a) is obtained when a proton is abstracted from Figure B15 (b). Structure (b) is the energy maxima, where hydrogen bonding network of rotating IM with its neighbors break. Structure (c) is obtained on further rotation, where the hydrogen bond between MSA and IM is regenerated as shown by dotted lines.

Bibliography

[1] Dresselhaus, M. S.; Thomas, I. L. *Nature* **2001**, *414*, 332.

[2] Steele, B. C. H.; Heinzel, A. *Nature* **2001**, *414*, 345.

[3] Kreuer, K.; Paddison, S. J.; Spohr, E.; Schuster, M. *Chem. Rev.* **2004**, *104*, 4637.

[4] Mauritz, K. A.; Moore, R. B. *Chem. Rev.* **2004**, *104*, 4535.

[5] Kreuer, K. D.; Fuchs, A.; Ise, M.; Spaeth, M.; Maier, J. *Electrochim. Acta* **1998**, *43*, 1281.

[6] Kreuer, K. D.; Rabenau, A.; Weppner, W. *Angew. Chem. Int. Ed. Engl.* **1982**, *21*, 208.

[7] Agmon, N. *Chem. Phys. Lett.* **1995**, *244*, 456.

[8] Asensio, J. A.; Borrós, S.; Gómez-Romero, P. *J. Polym. Sci. A* **2002**, *40*, 3703.

[9] Nakamoto, H.; Noda, A.; Hayamizu, K.; Hayashi, S.; Hamaguchi, H. O.; Watanabe, M. *J. Phys. Chem. C* **2007**, *111*, 1541.

[10] Devanathan, R. *Energy Environ. Sci.* **2008**, *1*, 101.

[11] Zhang, H.; Shen, P. K. *Chem. Rev.* **2012**, *112*, 2780.

[12] Kusoglu, A.; Weber, A. Z. *Chem. Rev.* **2017**, *117*, 987.

[13] Tang, J.; Yuan, W.; Zhang, J.; Li, H.; Zhang, Y. *RSC Adv.* **2013**, *3*, 8947.

[14] James, P. J.; Elliott, J. A.; McMaster, T. J.; Newton, J. M.; Elliott, A. M. S.; Hanna, S.; Miles, M. J. *J. Membr. Sci.* **2000**, *35*, 5111.

[15] McLean, R. S.; Doyle, M.; Sauer, B. B. *Macromolecules* **2000**, *33*, 6541.

[16] Nguyen, T. V.; Nguyen, M. V.; Lin, G.; Rao, N.; Xie, X.; Zhu, D.-M. *Electrochem. Solid-State Lett.* **2006**, *9*, A88.

[17] Kwon, O.; Kang, Y.; Wu, S.; Zhu, D.-M. *J. Phys. Chem. B* **2010**, *114*, 5365.

[18] Novitski, D.; Holdcroft, S. *ACS Appl. Mater. Interfaces* **2015**, *7*, 27314.

[19] Zawodzinski, T. A.; Derouin, C.; Radzinski, S.; Sherman, R. J.; Smith, V. T.; Springer, T. E.; Gottesfeld, S. *J. Electrochem. Soc.* **1993**, *140*, 1041.

[20] Goswami, S.; Klaus, S.; Benziger, J. *Langmuir* **2008**, *24*, 8627.

[21] Bass, M.; Berman, A.; Singh, A.; Konovalov, O.; Freger, V. *J. Phys. Chem. B* **2010**, *114*, 3784.

[22] He, Q.; Kusoglu, A.; Lucas, I. T.; Clark, K.; Weber, A. Z.; Kostecki, R. *J. Phys. Chem. B* **2011**, *115*, 11650.

[23] Zawodzinski, T. A.; Gottesfeld, S.; Shoichet, S.; Mccarthy, T. J. *J. Appl. Electrochem.* **1993**, *23*, 86.

[24] Perrin, J.-C.; Lyonnard, S.; Volino, F. *J. Phys. Chem. C* **2007**, *111*, 3393.

[25] Zawodzinski, T. A.; Neeman, M.; Cottesfeld, S. *J. Phys. Chem.* **1991**, *95*, 6040.

[26] Gong, X.; Bandis, A.; Tao, A.; Meresi, G.; Wang, Y.; Inglefield, P. T.; Jones, A. A.; Wen, W. Y. *Polymer* **2001**, *42*, 6485.

[27] Edmondson, C. A.; Fontanella, J. J. *Solid State Ionics* **2002**, *152*, 355.

[28] Tsushima, S.; Teranishi, K.; Hirai, S. *Energy* **2005**, *30*, 235.

[29] Kidena, K.; Ohkubo, T.; Takimoto, N.; Ohira, A. *Eur. Polym. J.* **2010**, *46*, 450.

[30] Ma, Z. R.; Jiang, R. C.; Myers, M. E.; Thompson, E. L.; Gittleman, C. S. *J. Mater. Chem.* **2011**, *21*, 9302.

[31] Liu, Y.; Sambasivarao, S. V.; Horan, J. L.; Yang, Y.; Maupin, C. M.; Herring, A. M. *J. Phys. Chem. C* **2014**, *118*, 854.

[32] Li, J.; Park, J. K.; Moore, R. B.; Madsen, L. A. *Nat. Mater.* **2011**, *10*, 507.

[33] Li, J.; Wilmsmeyer, K. G.; Madsen, L. A. *Macromolecules* **2009**, *42*, 255.

[34] Vishnyakov, A.; Neimark, A. V. *J. Phys. Chem. B* **2001**, *105*, 9586.

[35] Jang, S. S.; Molinero, V.; Tahir, C.; Goddard III, W. A. *J. Phys. Chem. B* **2004**, *108*, 3149.

[36] Cui, S.; Liu, J.; Selvan, M. E.; Keffer, D. J.; Edwards, B. J.; Steele, W. V. *J. Phys. Chem. B* **2007**, *111*, 2208.

[37] Venkatnathan, A.; Devanathan, R.; Dupuis, M. *J. Phys. Chem. B* **2007**, *111*, 7234.

[38] Devanathan, R.; Venkatnathan, A.; Dupuis, M. *J. Phys. Chem. B* **2007**, *111*, 8069.

[39] Devanathan, R.; Venkatnathan, A.; Dupuis, M. *J. Phys. Chem. B* **2007**, *111*, 13006.

[40] Sunda, A. P.; Venkatnathan, A. *Soft Matter* **2012**, *8*, 10827.

[41] Sunda, A. P.; Venkatnathan, A. *J. Mater. Chem. A* **2013**, *1*, 557.

[42] Paddison, S. J. *Solid State Ionics* **1998**, *113*, 333.

[43] Paddison, S. J. *J. New. Mat. Electrochem. Syst.* **2001**, *4*, 197.

[44] Paddison, S. J.; Elliott, J. A. *J. Phys. Chem. A* **2005**, *109*, 7583.

[45] Paddison, S.; Elliott, J. *Solid State Ionics* **2006**, *177*, 2385.

[46] Petersen, M. K.; Voth, G. A. *J. Phys. Chem. B* **2006**, *110*, 18594.

[47] Goddard, W.; Merinov, B.; van Duin, A.; Jacob, T.; Blanco, M.; Molinero, V.; Jang, S.; Jang, Y. *Molecular Simulation* **2006**, *32*, 251.

[48] Petersen, M. K.; Wang, F.; Blake, N. P.; Metiu, H.; Voth, G. A. *J. Phys. Chem. B* **2005**, *109*, 3727.

[49] Feng, S.; Voth, G. A. *J. Phys. Chem. B* **2011**, *115*, 5903.

[50] Feng, S.; Savage, J.; Voth, G. A. *J. Phys. Chem. C* **2012**, *116*, 19104.

[51] Choe, Y.-K.; Tsuchida, E.; Ikeshoji, T.; Yamakawa, S.; Hyodo, S.-A. *Phys. Chem. Chem. Phys.* **2009**, *11*, 3892.

[52] Ilhan, M. A.; Spohr, E. *J. Phys.: Condens. Matter* **2011**, *23*, 234104.

[53] Devanathan, R.; Idupulapati, N.; Baer, M. D.; Mundy, C. J.; Dupuis, M. *J. Phys. Chem. B* **2013**, *117*, 16522.

[54] Meyers, J. P.; Mcgrath, J. E.; Borup, R.; Meyers, J.; Pivovar, B.; Kim, Y. S.; Mukundan, R.; Garland, N.; Myers, D.; Wilson, M. *Chem. Rev.* **2007**, *107*, 3904.

[55] Kumar, M.; Paddison, S. *J. Mater. Res.* **2012**, *27*, 1982.

[56] Rodriguez, D.; Jegat, C.; Trinquet, O.; Grondin, J.; Lassègues, J. *Solid State Ionics* **1993**, *61*, 195.

[57] Wannek, C.; Kohnen, B.; Oetjen, H.-F.; Lippert, H.; Mergel, J. *Fuel Cells* **2008**, *8*, 87.

[58] Li, Q.; Jensen, J. O.; Savinell, R. F.; Bjerrum, N. J. *Prog Polym Sci* **2009**, *34*, 449.

[59] Araya, S. S.; Zhou, F.; Liso, V.; Sahlin, S. L.; Vang, J. R.; Thomas, S.; Gao, X.; Jeppesen, C.; Kaer, S. K. *Int. J. Hydrogen Energ.* **2016**, *41*, 21310.

[60] He, R.; Li, Q.; Xiao, G.; Bjerrum, N. J. *J. Membr. Sci.* **2003**, 169.

[61] Li, Q.; He, R.; Jensen, J. O.; Bjerrum, N. J. *Fuel Cells* **2004**, *4*, 147.

[62] Pahari, S.; Choudhury, C. K.; Pandey, P. R.; More, M.; Venkatnathan, A.; Roy, S. *J. Phys. Chem. B* **2012**, *116*, 7357.

[63] More, M.; Pahari, S.; Roy, S.; Venkatnathan, A. *J. Mol. Liq.* **2013**, *19*, 109.

[64] More, M.; Sunda, A. P.; Venkatnathan, A. *RSC Adv.* **2014**, *4*, 19746.

[65] Pahari, S.; Roy, S. *RSC Adv.* **2016**, *6*, 8211.

[66] Kumar, M.; Venkatnathan, A. *J. Phys. Chem. B* **2013**, *117*, 14449.

[67] Noto, V. D.; Piga, M.; Gi, G. A.; Lavina, S.; Smotkin, E. S.; Sanchez, J.-Y.; Iojoiu, C. *J. Phys. Chem. C* **2012**, *116*, 1370.

[68] Shirata, K.; Kawauchi, S. *J. Phys. Chem. B* **2015**, *119*, 592.

[69] Vilčiauskas, L.; Tuckerman, M. E.; Melchior, J. P.; Bester, G.; Kreuer, K.-D. *Nat. Chem.* **2012**, *4*, 461.

[70] Vilčiauskas, L.; Tuckerman, M. E.; Melchior, J. P.; Bester, G.; Kreuer, K.-D. *Solid State Ionics* **2013**, *252*, 34.

[71] Kumbharkar, S. C.; Kharul, U. K. *J. Membr. Sci.* **2010**, *360*, 418.

[72] Habib, M. A.; Bockris, J. O. *J. Electrochem. Soc.* **1985**, *132*, 108.

[73] Noda, A.; Susan, M. A. B. H.; Kudo, K.; Mitsushima, S.; Hayamizu, K.; Watanabe, M. *J. Phys. Chem. B* **2003**, *107*, 4024.

[74] Matsuoka, H.; Nakamoto, H.; Susan, M. A. B. H.; Watanabe, M. *Electrochim. Acta* **2005**, *50*, 4015.

[75] Galiński, M.; Lewandowski, A.; Stępniak, I. *Electrochim. Acta* **2006**, *51*, 5567.

[76] Fernicola, A.; Panero, S.; Scrosati, B.; Tamada, M.; Ohno, H. *ChemPhysChem* **2007**, *8*, 1103.

[77] Macfarlane, D. R.; Forsyth, M.; Howlett, P. C.; Pringle, J. M.; Sun, J.; Annat, G.; Neil, W.; Izgorodina, E. I. *Acc. Chem. Res.* **2007**, *40*, 1165.

[78] Bai, Y.; Cao, Y.; Zhang, J.; Wang, M.; Li, R.; Wang, P.; Zakeeruddin, S. M.; Gratzel, M. *Nat. Mater.* **2008**, *7*, 626.

[79] Ye, H.; Huang, J.; Xu, J. J.; Kodiweera, N. K. A. C.; Jayakody, J. R. P.; Greenbaum, S. G. *J. Power Sources* **2008**, *178*, 651.

[80] Greaves, T. L.; Drummond, C. J. *Chem. Rev.* **2008**, *108*, 206.

[81] Cho, E.; Park, J. S.; Sekhon, S. S.; Park, G. G.; Yang, T. H.; Lee, W. Y.; Kim, C. S.; Park, S. B. *J. Electrochem. Soc.* **2009**, *156*, B197.

[82] Fujita, M. Y.; Kousa, Y.; Kidena, K.; Ohira, A.; Takeoka, Y.; Rikukawa, M. *Phys. Chem. Chem. Phys.* **2011**, *13*, 13427.

[83] Xiang, J.; Chen, R.; Wu, F.; Li, L.; Chen, S.; Zou, Q. *Electrochim. Acta* **2011**, *56*, 7503.

[84] Eshetu, G. G.; Armand, M.; Scrosati, B.; Passerini, S. *Angew. Chem. Int. Ed.* **2014**, *53*, 13342.

[85] Díaz, M.; Ortiz, A.; Ortiz, I. *J. Membr. Sci.* **2014**, *469*, 379.

[86] MacFarlane, D. R.; Tachikawa, N.; Forsyth, M.; Pringle, J. M.; Howlett, P. C.; Elliott, G. D.; Davis, J. H.; Watanabe, M.; Simon, P.; Angell, C. A. *Energy Environ. Sci.* **2014**, *7*, 232.

[87] Luo, J. et al. *Energy Environ. Sci.* **2015**, *8*, 1276.

[88] Schechter, A.; Savinell, F. *Solid State Ionics* **2002**, *147*, 181.

[89] Susan, M. A. B. H.; Yoo, M.; Nakamoto, H.; Watanabe, M. *Chem. Lett.* **2003**, *32*, 836.

[90] Sood, R.; Iojoiu, C.; Espuche, E.; Gouanvé, F.; Gebel, G.; Mendil-Jakani, H.; Lyonnard, S.; Jestin, J. *J. Phys. Chem. C* **2012**, *116*, 24413.

[91] Hoarfrost, M. L.; Tyagi, M.; Segalman, R. A.; Reimer, J. A. *J. Phys. Chem. B* **2012**, *116*, 8201.

[92] Schaftenaar, G.; Noordik, J. *J. Chem. Eng. Data* **2000**, *14*, 123.

[93] Dennington, R.; Keith, T.; Millam, J. Semichem Inc. Shawnee Mission KS **2009**.

[94] Humphrey, W.; Dalke, A.; Schulten, K. *J. Mol. Graphics* **1996**, *14*, 33.

[95] Pettersen, E. F.; Goddard, T. D.; Huang, C. C.; Couch, G. S.; Greenblatt, D. M.; Meng, E. C.; Ferrin, T. E. *J. Comput. Chem.* **2004**, *25*, 1605.

[96] Brooks, B. R.; Bruccoleri, R. E.; Olafson, B. D.; States, D. J.; Swaminathan, S.; Karplus, M. *J. Comp. Chem.* **1983**, *4*, 187.

[97] Sprenger, K. G.; Jaeger, V. W.; Pfaendtner, J. *J. Phys. Chem. B* **2015**, *119*, 5882.

[98] Jorgensen, W. L.; Maxwell, D. S.; Tirado-Rives, J. *J. Am. Chem. Soc.* **1996**, *118*, 11225.

[99] Sun, H. *J. Phys. Chem. B* **1998**, *102*, 7338.

[100] Scott, W. R. P.; Hünenberger, P. H.; Tironi, I. G.; Mark, A. E.; Billeter, S. R.; Fennen, J.; Torda, A. E.; Huber, T.; Krüger, P.; van Gunsteren, W. F. *J. Phys. Chem. A* **1999**, *103*, 3596.

[101] Sunda, A. P.; Venkatnathan, A. *J. Comput. Chem.* **2011**, *32*, 3319.

[102] Sunda, A. P. *J. Mater. Chem. A* **2015**, *3*, 1.

[103] Nasrabadi, A. T.; Gelb, L. D. *J. Phys. Chem. B* **2017**, *121*, 1908.

[104] Szabo, A.; Ostlund, S. N. *Modern Quantum Chemistry: Introduction to Advanced Electronic Structure Theory; Dover Publications: New York*; **1996**.

[105] Parr, R. G.; Yang, W. *Density Functional Theory for Atoms and Molecules; Oxford University press: New York*; **1989**.

[106] Kohn, W.; Becke, A. D.; Parr, R. G. *J. Phys. Chem.* **1996**, *100*, 12974.

[107] Perdew, A., J. P.; Zunger *Phys. Rev. B* **1981**, *23*, 5048.

[108] Perdew, Y., J. P.; Wang *Phys. Rev. B* **1992**, *45*, 13244.

[109] Vosko, S. H.; Wilk, L.; Nusair, M. *Can. J. Phys.* **1980**, *58*, 1200.

[110] Perdew, J. P.; Burke, K.; Ernzerhof, M. *Phys. Rev. Lett.* **1996**, *77*, 3865.

[111] Becke, A. D. *J. Chem. Phys.* **1993**, *98*, 5648.

[112] Becke, A. D. *J. Chem. Phys.* **1993**, *98*, 1372.

[113] Tao, J.; Perdew, J. P.; Staroverov, V. N.; Scuseria, G. E. *Phys. Rev Lett.* **2003**, *91*, 146401.

[114] Lee, C.; Yang, W.; Parr, R. G. *Phys. Rev. B* **1988**, *37*, 785.

[115] Becke, A. D. *Phys. Rev. A.* **1998**, *38*, 3098.

[116] Stephens, P. J.; Devlin, F. J.; Chabalowski, C. F.; Frisch, M. J. *J. Phys. Chem.* **1994**, *98*, 11623.

[117] Zhao, Y.; Schultz, N. E.; Truhlar, D. G. *J. Chem. Theory. Comput* **2006**, *2*, 364.

[118] Zhao, Y.; Truhlar, D. G. *Acc. Chem. Res* **2008**, *41*, 157.

[119] Grimme, S. *J. Comput. Chem.* **2006**, *27*, 1787.

[120] Frenkel, D.; Smit, B. *Understanding Molecular Simulation: From Algorithms to Applications; Academic Press, Inc. Orlando, FL, USA*; **1996**.

[121] Leach, A. R. *Molecular Modelling: Principles and Applications; Prentice Hall: Harlow, England*; **2001**.

[122] Rapaport, D. C. *The Art of Molecular Dynamics Simulation; Cambridge University Press: New York, NY, USA*; **2004**.

[123] Allen, M. P.; Tildesley, D. J. *Computer Simulations of Liquids; Oxford Science Publications: New York*; **1987**.

[124] Eikerling, M.; Paddison, S. J.; Zawodzinski, T. A. *J. New. Mat. Electrochem. Syst.* **2002**, *5*, 15.

[125] Mikami, M.; Urata, S.; Tsuzuki, S.; Shinoda, W.; Takada, A.; Irisawa, J. *Phys. Chem. Chem. Phys.* **2004**, *6*, 3325.

[126] Vila, A.; Mosquera, R. A. *J. Phys. Chem. A* **2000**, *104*, 12006.

[127] Vishnyakov, A.; Neimark, A. V. *J. Phys. Chem. B* **2001**, *105*, 7830.

[128] Urata, S.; Tsuzuki, S.; Mikami, M.; Takada, A.; Uchimaru, T.; Sekiya, A. *J. Comput. Chem.* **2002**, *23*, 1472.

[129] Urata, S.; Tsuzuki, S.; Takada, A.; Mikami, M.; Uchimaru, T.; Sekiya, A. *J. Comput. Chem.* **2004**, *25*, 447.

[130] Urata, S.; Irisawa, J.; Takada, A.; Shinoda, W.; Tsuzuki, S.; Mikami, M. *J. Phys. Chem. B* **2005**, *109*, 4269.

[131] Wu, Y.; Tepper, H. L.; Voth, G. A. *J. Chem. Phys.* **2006**, *124*, 024503.

[132] Choe, Y.-K.; Tsuchida, E.; Ikeshoji, T.; Yamakawa, S.; Hyodo, S.-A. *J. Phys. Chem. B* **2008**, *112*, 11586.

[133] Arntsen, C.; Savage, J.; Tse, Y. L. S.; Voth, G. A. *Fuel Cells* **2016**, *16*, 695.

[134] Spohr, E.; Commer, P.; Kornyshev, A. A. *J. Phys. Chem. B* **2002**, *106*, 10560.

[135] Hess, B.; Kutzner, C.; van der Spoel, D.; Lindahl, E. *J. Chem. Theory Comput.* **2008**, *4*, 435.

[136] Berendsen, H. J. C.; Postma, J. P. M.; van Gunsteren, W. F.; DiNola, A.; Haak, J. R. *J. Chem. Phys.* **1984**, *81*, 3684.

[137] Darden, T.; York, D.; Pedersen, L. *J. Chem. Phys.* **1993**, *98*, 10089.

[138] Nosé, S. *Mol. Phys.* **1984**, *52*, 255.

[139] Wise, A. J.; Grey, J. K.; Devanathan, R.; Dupuis, M. *Phys. Chem. Chem. Phys.* **2012**, *14*, 11281.

[140] Knox, C. K.; Voth, G. A. *J. Phys. Chem. B* **2010**, *114*, 3205.

[141] Clark, J. K.; Paddison, S. J.; Hamrock, S. J. *Phys. Chem. Chem. Phys.* **2012**, *14*, 16349.

[142] Kreuer, K. D. *J. Membr. Sci.* **2001**, *185*, 29.

[143] Malek, K.; Eikerling, M.; Wang, Q.; Liu, Z.; Otsuka, S.; Akizuki, K.; Abe, M. *J. Chem. Phys.* **2008**, *129*, 204702.

[144] Cui, S.; Liu, J.; Selvan, M. E.; Paddison, S. J.; Keffer, D. J.; Edwards, B. J. *J. Phys. Chem. B* **2008**, *112*, 13273.

[145] Sengupta, S.; Lyulin, A. V. *J. Phys. Chem. B* **2018**, *122*, 6107.

[146] Devanathan, R.; Venkatnathan, A.; Rousseau, R.; Dupuis, M.; Frigato, T.; Gu, W.; Helms, V. *J. Phys. Chem. B* **2010**, *114*, 13681.

[147] Tripathy, M.; Kumar, P. B.; Deshpande, A. P. *J. Phys. Chem. B* **2017**, *121*, 4873.

[148] Sengupta, S.; Pant, R.; Komarov, P.; Venkatnathan, A.; Lyulin, A. V. *Int. J. Hydrogen Energy* **2017**, *42*, 27254.

[149] Di Noto, V.; Negro, E.; Sanchez, J. Y.; Lojoiu, C. *J. Am. Chem. Soc.* **2010**, *132*, 2183.

[150] Liu, S.; Zhou, L.; Wang, P.; Shao, Z.; Yi, B. *J. Mater. Chem. A* **2013**, *1*, 4423.

[151] Mogurampelly, S.; Ganesan, V. *J. Chem. Phys.* **2017**, *146*, 074902.

[152] Blanchard, J. W.; Belieres, J.-P.; Alam, T. M.; Yarger, J. L.; Holland, G. P. *J. Phys. Chem. Lett.* **2011**, *2*, 1077.

[153] Nakamoto, H.; Watanabe, M. *Chem. Comm.* **2007**, 2539.

[154] Lee, S.-Y.; Ogawa, A.; Kanno, M.; Nakamoto, H.; Yasuda, T.; Watanabe, M. **2010**, *4*, 9764.

[155] Liu, S.; Zhou, L.; Wang, P.; Zhang, F.; Yu, S.; Shao, Z.; Yi, B. *ACS Appl. Mater. Interfaces* **2014**, *6*, 3195.

[156] Jorgensen, W. L.; Maxwell, D. S.; Tirado-Rives, J. *J. Am. Chem. Soc.* **1996**, *118*, 11225.

[157] Bhargava, B. L.; Balasubramanian, S. *J. Chem. Phys.* **2007**, *127*, 114510.

[158] Rey-Castro, C.; Tormo, A. L.; Vega, L. F. *Fluid Phase Equilibria* **2007**, *256*, 62.

[159] Kowsari, M. H.; Alavi, S.; Ashrafizaadeh, M.; Najafi, B. *J. Chem. Phys.* **2009**, *130*, 014703.

[160] Tenney, C. M.; Massel, M.; Mayes, J. M.; Sen, M.; Brennecke, J. F.; Maginn, E. J. *J. Chem. Eng. Data* **2014**, *59*, 391.

[161] Lopes, J. N. C.; Deschamps, J.; Pádua, A. A. H. *J. Phys. Chem. B* **2004**, *108*, 2038.

[162] Bussi, G.; Donadio, D.; Parrinello, M. *J. Chem. Phys.* **2007**, *126*, 014101.

[163] Li, S.; Fried, J.; Colebrook, J.; Burkhardt, J. *Polymer* **2010**, *51*, 5640.

[164] Bhavsar, R. S.; Nahire, S. B.; Kale, M. S.; Patil, S. G.; Aher, P. P.; Bhavsar, R. A.; Kharul, U. K. *J. Appl. Polym. Sci.* **2011**, *120*, 1090.

[165] Yasuda, T.; Kinoshita, H.; Miran, M. S.; Tsuzuki, S.; Watanabe, M. *J. Chem. Eng. Data* **2013**, *58*, 2724.

[166] Yu, S.; Yan, F.; Zhang, X.; You, J.; Wu, P.; Lu, J.; Xu, Q.; Xia, X.; Ma, G. *Macromolecules* **2008**, *41*, 3389.

[167] Belieres, J. P.; Angell, C. A. *J. Phys. Chem. B* **2007**, *111*, 4926.

[168] Yoshizawa, M.; Xu, W.; Angell, C. A. *J. Am. Chem. Soc.* **2003**, *125*, 15411.

[169] Davidowski, S. K.; Thompson, F.; Huang, W.; Hasani, M.; Amin, S. A.; Angell, C. A.; Yarger, J. L. *J. Phys. Chem. B* **2016**, *120*, 4279.

[170] Hunt, P. A.; Ashworth, C. R.; Matthews, R. P. *Chem. Rev.* **2015**, *44*, 1257.

[171] Armarego, W. L.; Chai, C. L. L. *Purification of Laboratory Chemicals (Sixth Edition) Butterworth-Heinemann: Oxford*; **2009**.

[172] Kawada, A.; McGhie, A. R.; Labes, M. M. *J. Chem. Phys.* **1970**, *52*, 3121.

[173] Kreuer, K. D. *Solid State Ionics* **1997**, *94*, 55.

[174] Münch, W.; Kreuer, K. D.; Silvestri, W.; Maier, J.; Seifert, G. *Solid State Ionics* **2001**, *145*, 437.

[175] Daycock, J. T.; Jones, G. P.; Evans, J. R.; Thomas, J. M. *Nature* **1968**, *218*, 672.

[176] Kumar, M.; Venkatnathan, A. *J. Phys. Chem. B* **2015**, *119*, 3213.

[177] Goward, G. R.; Saalwächter, K.; Fischbach, I.; Spiess, H. W. *Solid State Nucl. Magn. Reson.* **2003**, *24*, 150.

[178] Luo, J.; Conrad, O.; Vankelecom, I. F. J. *J. Mater. Chem. A* **2013**, *1*, 2238.

[179] Rachocki, A.; Pogorzelec-Glaser, K.; Pietraszko, A.; Tritt-Goc, J. *J. Phys.: Condens. Matter* **2008**, *20*, 505101.

[180] Traer, J. W.; Goward, G. R. *Phys. Chem. Chem. Phys.* **2012**, *12*, 263.

[181] Atkins, P.; Overton, T.; Rourke, J.; Weller, M.; Armstrong, F.; Salvador, P.; Hagerman, M.; Spiro, T.; Stiefel, E. *Inorganic Chemistry, 4th ed. W. H. Freeman and Company: New York*; **2006**.

[182] Gernon, M. D.; Wu, M.; Buszta, T.; Janney, P. *Green Chem.* **1999**, *1*, 127.

[183] De Almeida, N. E.; Goward, G. R. *J. Power Sources* **2014**, *268*, 853.

[184] Paddison, S. J.; Pratt, L. R.; Zawodzinski, T. A. *J. New. Mat. Electrochem. Syst.* **1999**, *2*, 183.

[185] Paddison, S. J. *Annu. Rev. Mater. Res.* **2003**, *33*, 289.

[186] Clark, J. K.; Paddison, S. J. *Electrochim. Acta* **2013**, *101*, 279.

[187] Frisch, M. J. et al. *Gaussian 09, Revision B.01, Gaussian, Inc., Wallingford CT*; **2009**.

[188] Li, X.; Frisch, M. J. *J. Chem. Theory Comput.* **2006**, *2*, 835.

[189] Eidman, K. F.; Nichols, P. J. *Trifluoroacetic Acid In Encyclopedia of Reagents for Organic Synthesis, (Ed.)*; **2006**.

[190] Goldberg, R. N.; Kishore, N.; Lennen, R. M. *J. Phys. Chem. Ref. Data* **2002**, *31*, 231.

[191] Trummal, A.; Lipping, L.; Kaljurand, I.; Koppel, I. A.; Leito, I. *J. Phys. Chem. A* **2016**, *120*, 3663.

[192] Miran, M. S.; Yasuda, T.; Susan, M. A. B. H.; Dokko, K.; Watanabe, M. *J. Phys. Chem. C* **2014**, *118*, 27631.

[193] Frisch, M. J. et al. *Gaussian 09, Revision D.01, Gaussian, Inc., Wallingford CT*; **2009**.

[194] Tomasi, J.; Mennucci, B.; Cammi, R. *Chem. Rev.* **2005**, *105*, 2999.

[195] Wang, C.; Clark, J. K.; Kumar, M.; Paddison, S. J. *Solid State Ionics* **2011**, *199*, 6.

[196] Clark, J. K.; Paddison, S. J. *Solid State Ionics* **2012**, *213*, 83.

[197] Sun, X.; Cao, B.; Zhou, X.; Liu, S.; Zhu, X.; Fu, H. *J. Mol. Liq.* **2016**, *221*, 254.

[198] Wang, C.; Paddison, S. J. *Phys. Chem. Chem. Phys.* **2010**, *12*, 970.

[199] Chen, H.; Yan, T.; Voth, G. A. *J. Phys. Chem. A* **2009**, *113*, 4507.

[200] Cybulski, S. M.; Scheiner, S. *J. Phys. Chem.* **1989**, *93*, 6565.

[201] Chu, C. H.; Ho, J. J. *Chem. Phys. Lett.* **1994**, *221*, 523.

[202] Scheiner, S. *Acc. Chem. Res.* **1994**, *27*, 402.

[203] Chu, C. H.; Ho, J. J. *J. Phys. Chem.* **1995**, *99*, 16590.

[204] Chang, T. M.; Dang, L. X.; Devanathan, R.; Dupuis, M. *J. Phys. Chem. A* **2010**, *114*, 12764.

[205] Hunter, E. P. L.; Lias, S. G. *J. Phys. Chem. Ref. Data* **1998**, *27*, 413.

[206] Aue, D. H.; Webb, H. M.; Bowers, M. T. *J. Am. Chem. Soc.* **1976**, *98*, 311.

[207] Leito, I.; Raamat, E.; Kütt, A.; Saame, J.; Kipper, K.; Koppel, I. A.; Koppel, I.; Zhang, M.; Mishima, M.; Yagupolskii, L. M.; Garlyauskayte, R. Y.; Filatov, A. A. *J. Phys. Chem. A* **2009**, *113*, 8421.

[208] Viggiano, A. A.; Henchman, M. J.; Dale, F.; Deakyne, C. A.; Paulson, J. F. *J. Am. Chem. Soc.* **1992**, *114*, 4299.

[209] Koppel, I. A.; Taft, R. W.; Anvia, F.; Zhu, S.-Z.; Hu, L.-Q.; Sung, K.-S.; DesMarteau, D. D.; Yagupolskii, L. M.; Yagupolskii, Y. L. *J. Am. Chem. Soc.* **1994**, *116*, 3047.

[210] Caldwell, G.; Renneboog, R.; Kebarle, P. *Can. J. Chem.* **1989**, *67*, 611.